DEVELOPMENT OF PREDICTIVE AND NONLINEAR CONTROL DESIGNS FOR AN ELECTRIC ALL WHEEL DRIVE POWERTRAIN SYSTEM

by

ANTHONY ROSS

A dissertation submitted in partial fulfillment of the
requirements for the degree of

DOCTOR OF PHILOSOPHY IN SYSTEMS ENGINEERING

2024

Oakland University
Rochester, Michigan

Doctoral Advisory Committee:

Manohar Das, Ph.D., Chair
Ka C. Cheok, Ph.D.
Christopher Kobus, Ph.D.
Kasaundra Tomlin, Ph.D.

ACKNOWLEDGMENTS

I would like to extend my deepest thanks to my wife, Shelby, who has stood by my side every step of this process. I would also like to extend thanks to my family and friends who encouraged and lifted me up along the way. Thank you to Dr. Das who showed incredible patience and kindness in helping me achieve this goal. Also, thank you to my committee members who were supportive and encouraging through this entire process.

Also, I'd like to extend a special thanks to Dr. Jose Alcantar Velasquez who mentored me and provided invaluable assistance to help me get started on this journey.

Anthony Ross

ABSTRACT

DEVELOPMENT OF PREDICTIVE AND NONLINEAR CONTROL DESIGNS FOR AN ELECTRIC ALL WHEEL DRIVE POWERTRAIN SYSTEM

by

ANTHYONY ROSS

Adviser: Manohar Das, Ph.D.

Vehicle electrification is a strong trend in the automotive industry. The use of electric motors for propulsion offers many opportunities and some technical difficulties. This thesis addresses the challenge of controlling and coordinating two electric motors as part of an electric all wheel drive (eAWD) powertrain to maintain vehicle stability during longitudinal and lateral motion of the vehicle. The control problem is broken into two pieces, vehicle level control and control of the electric motors.

At the vehicle level, several control strategies are developed and compared. First a weighted one step ahead (WOSA) controller is developed. Next a nonlinear model predictive controller (NLMPC) is developed. Next a feedback linearization controller (FLC) is developed. Finally, a sliding mode controller (SMC) is developed. In each case, the vehicle level controller is integrated with fuzzy rules to translate the vehicle level control signal into reference targets for the motor controllers. The integration of a physical model and fuzzy rules into a single controller is a unique concept that is explored in this thesis.

Each of the electric motors consists of a traction motor and torque vectoring motor. WOSA controllers are developed for each type of motor and integrated with the vehicle level controller for overall vehicle control. The WOSA is a simple but powerful control approach for the motor controllers.

Key system states are estimated using the controller output observer (COO) concept. The COO provides a good estimate of the system states with sensor data that is already available on typical vehicles. The COO also uses the WOSA control strategy.

For both longitudinal and lateral motion, the effectiveness of the control strategies are demonstrated for launch and a high speed double lane change maneuver on high friction and low friction road surfaces using Simulink and CarSim.

TABLE OF CONTENTS

TABLE OF CONTENTS - continued

LIST OF TABLES

LIST OF FIGURES

LIST OF ABBREVIATIONS

EV	Electric Vehicle
eAWD	Electric All Wheel Drive
ABS	Anti Lock Braking System
WOSA	Weighted One Step Ahead
NLMPC	Non Linear Model Predictive Controller
FLC	Feedback Linearization Controller
SMC	Sliding Mode Controller
COO	Controller Output Observer
ACC	Adaptive Cruise Control
PID	Proportion Integration Derivative
KF	Kalman Filter
EKF	Extended Kalman Filter
NN	Neural Network
CG	Center of gravity

CHAPTER ONE

INTRODUCTION

1.1 Vehicle Electrification

Vehicle electrification is an important trend in the automotive industry. Many automotive manufacturers have committed themselves to converting over their fleets to all EV within the next few years [1],[2]. Electric powertrains offer unique advantages, and some challenges.

The most obvious advantage is lower emissions which is good for the environment. Other advantages include quiet and smooth operation, very quick torque response, and possibly lower operating costs because of fewer mechanical powertrain components that can wear out. A thorough survey comparing EVs with traditional ICE vehicles is presented in [3].

There are some disadvantages that are sometimes associated with electric vehicles. One is the limited range of the battery pack. Another is perceived lack of dynamic performance. A third disadvantage is that more complicated vehicle controls are needed for the battery pack, power electronics, electric motors, etc. Integrating the electrical controls with the traditional vehicle controls for ABS, traction control and stability control takes a considerable amount of effort. A very good overview of the architecture for controlling an EV vehicle is presented in [4].

One way to address the issue of lack of dynamic performance is to use multiple electric motors in the powertrain. Including multiple motors requires advanced techniques for controlling and coordinating the motors to provide a pleasant and safe driving experience.

This thesis presents an electric all wheel drive (eAWD) powertrain that consists of an electric motor assembly on the front and rear axles. The motor assembly consists of a traction motor which is responsible for providing torque in the longitudinal direction, and a small torque vectoring motor which is responsible for providing torque from side to side for lateral vehicle motion. A detailed discussion of various types of traction motor configurations and architectures is provided in [5]. A general discussion of torque vectoring is presented in [6]. A detailed explanation of the traction and torque vectoring motors for the eAWD that is used in this thesis is presented in Chapter 3.

1.2 Vehicle Motion Controller

1.2.1 Controller Architecture

For this thesis, the vehicle motion controller is composed of two components: the vehicle level controller and the powertrain level controller. At the vehicle level, the driver's requests are determined based on the accelerator pedal position and steering wheel angle. The vehicle controller has to interpret these inputs to determine the appropriate tire force targets (traction and torque vectoring) to meet the driver's requests. These target tire forces are then cascaded to the powertrain controller.

At the powertrain level, the target tire forces are converted into torque requests for each of the electric motors which comprises the eAWD. The motor torque request are then converted into half shaft torque requests that are sent to the wheels to propel the vehicle. A diagram of this concept is presented in Figure 1.1.

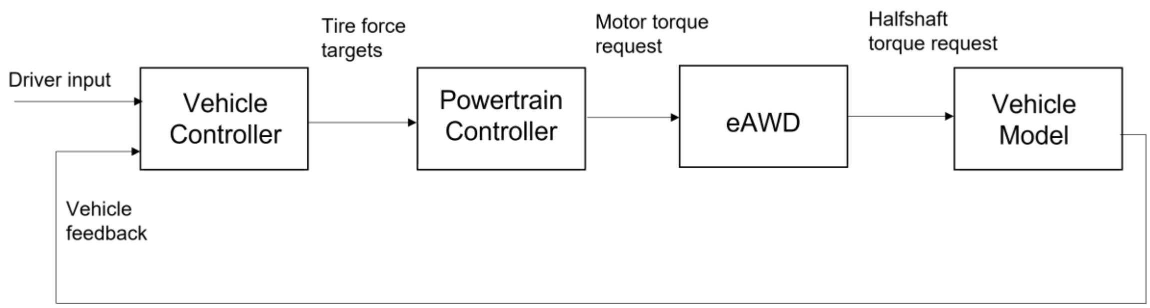

Figure 1.1 Overall control architecture for vehicle motion

This thesis considers longitudinal and lateral vehicle motion in the design of the vehicle motion controller.

For longitudinal motion, the vehicle is moving straight ahead. The operating scenario is driving on a straight road, launching from a stop at an intersection or stopping in a straight line. The typical vehicle controls associated with longitudinal motion are ABS braking, traction control, cruise control, collision avoidance control, etc. For this thesis, launching and slowing down on a high friction road surface and launching on a low friction road surface are considered. The controller consists of a weighted one step ahead (WOSA) predictive controller coupled with fuzzy rules to provide an integrated control strategy to improve the overall controller performance for tracking the target tire forces during each of the mentioned driving scenarios. A WOSA tracking controller is designed for the traction motor at the powertrain level. A detailed explanation of the WOSA controller concept is presented in Chapter 3. A detailed description of the longitudinal motion controller design is discussed in Chapter 4.

For lateral motion, the operating scenario is driving around a corner, changing lanes on the highway, going around a curve on an exit or entrance ramp, etc. Typical lateral motion controls include stability control, anti-rollover control, side slip control, lane departure avoidance, etc. At the vehicle level, the driver turns the steering wheel, and the vehicle controller interprets this as a yaw rate target. The controller calculates a control yaw moment that allows the vehicle to meet the yaw rate target. The control yaw moment is cascaded to the powertrain controller as target tire forces on either side of the vehicle. The powertrain controller then calculates motor torque requests to match the target tire forces. In this thesis, a nonlinear vehicle plant model is used to design the vehicle level controller. A WOSA controller is used to calculate the control yaw moment, and fuzzy rules are used to convert the control yaw moment into target tire forces for the powertrain controller. The fuzzy logic rules allow the controller to enforce constraints for the powertrain and add a level of robustness. A WOSA tracking controller is designed for the torque vectoring motors at the powertrain level. For this thesis, a high friction and low friction double lane change maneuver are considered. A detailed explanation of the lateral motion controller design is presented in Chapter 5.

Next, three additional vehicle level lateral motion controllers are considered. These controllers use the same powertrain controller as described above. It is interesting to note how well these controllers work with the fuzzy logic rule set to calculate the control yaw moment input that is used for the double lane change maneuver. The additional controllers considered are a nonlinear model predictive controller (NLMPC), a feedback linearization controller (FLC) and a sliding mode controller (SMC). These are discussed in Chapter 6.

1.2.2 Parameter Estimation

As part of the overall control strategy, it is necessary to estimate key parameters that cannot be directly measured. For the longitudinal control case, the vehicle speed and actual traction force are estimated. For the lateral motion case, the lateral velocity and lateral tire forces are estimated. These parameters are estimated using a controller output observer (COO). The advantage of the COO is that it provides good estimation, it is fairly simple to implement and it relies on measured signals that are already available on most vehicles. The COO is discussed in more detail in Chapters 4 and 5.

1.3 Literature Review

Research into using fuzzy logic to control various aspects of vehicle motion and dynamics is an ongoing area of interest. In [8],[9],[10],[11] fuzzy rules are used to control ABS braking and traction control. For ABS braking and traction control, the goal of the controller is to limit wheel slip by adjusting the brake pressure in the brake cylinders. Fuzzy rules are employed to adjust the braking pressures based on the slip rate error. The amount of pressure applied is proportional to the amount of slip rate error detected. The level of pressure is calculated from fuzzy logic membership functions.

In [12],[13],[14],[15],[16] fuzzy rules are used to track the desired yaw rate and/or slip angle to maintain vehicle stability during a maneuver such as a double lane change. In each of these works, the test vehicle uses an electric motor at each of the four wheel hubs. The controller calculates command torques for each motor to maintain the desired yaw rate and/or slip angle. Because there are four motors, they can be controlled independently to generate a desired torque distribution from left to right and front to rear.

Each of the works mentioned in [12 – 16] generally use the error between the desired yaw rate/slip angle and the actual output from the system as the input into the fuzzy logic rule base. These systems do not use a physical model of the vehicle to design the fuzzy logic controller. The rules for designing the fuzzy system are based on a heuristic understanding of the system and how it should perform. The approach of using fuzzy logic to design a yaw stability controller is effective. However, there is a considerable amount of effort to design the fuzzy rules, and the number of rules can become quite large.

In [17], an eAWD system consisting of a traditional full hybrid vehicle with a transaxle electric motor on the front axle and an electric motor system consisting of a combined traction and torque vectoring motor on the rear axle is presented. This research explored several control frameworks using the Youla parametrization approach for the yaw controller. Though the Youla parametrization approach is a very effective way to design a yaw stability controller, the implementation is not straightforward. The eAWD system used in this work is based on the eAWD that is discussed in [17].

Other researchers have used optimal and predictive control schemes as a way to implement yaw stability control [18], [19], [20], [21], [22]. In [18] a general predictive controller is used. The controller predicts the future value of the yaw rate, and takes control action at the present time based on predicted future error. In [19] a particle swarm optimization scheme is used to distribute the torque to the motor actuators to track a desired yaw target. In [20 - 22] model predictive control (MPC) is used for the yaw controller. MPC works by calculating a series of optimal control inputs for a series of time periods into the future according to a receding time horizon. MPC is an effective control strategy for yaw control.

1.4 Contributions of This Thesis

This thesis takes a unique approach to vehicle level controller design by combining the controller for the physical plant model with fuzzy rules into an integrated controller strategy. The physical plant model considers the actual dynamics of the system. However, a model does not perfectly capture the system behavior. Using fuzzy logic rules as part of the controller strategy allows for the combination of physical laws and "intelligent" intervention to improve the overall performance of the controller.

- For longitudinal motion, the vehicle controller calculates an overall traction force target based on the vehicle model. A fuzzy rule set is used to dynamically adjust the traction force distribution between the front and rear axles to account for weight shifting during launching and deceleration of the vehicle. Also, fuzzy rules are implemented to adjust the motor torques in a secondary control loop to improve the tracking of the target traction force.
- A fuzzy controller strategy is implemented to automatically adjust the traction motor torques to improve overall traction and reduce wheel slip during vehicle launch on a low friction surface.
- For lateral motion, several vehicle level controllers based on a nonlinear plant model are developed. Each controller is integrated with a fuzzy logic rule set. The vehicle level controller calculates the control yaw moment. The fuzzy logic rule set translates the control yaw moment into target tire forces for the torque vectoring motor

controllers. The fuzzy logic rules are based on an intuitive understanding of the relationship between the yaw moment and how the torque vectoring motors should respond. The effectiveness of these controllers is demonstrated by simulating a high speed double lane change on a high friction and a low friction road surface. The controller performances are compared and analyzed against each other. The controllers that are implemented are WOSA, NLMPC, FLC and SMC.

- At the powertrain level, WOSA controllers for the traction motor (longitudinal motion) and the torque vectoring motor (lateral motion) are developed. The effectiveness of these motor controllers is demonstrated in the overall control strategy for longitudinal and lateral motion control.
- Key vehicle parameters are estimated using COO observers implemented with the WOSA control strategy.
- The control strategies are implemented and simulated using Simulink and CarSim.

1.5 Dissertation Outline

- In Chapter 2, the eAWD system is described in detail, and the system equations are derived. Also, simulation with CarSim and Simulink is discussed.
- In Chapter 3, the derivation of the one step ahead controller for linear and nonlinear plants is presented.
- In Chapter 4, a discussion of longitudinal vehicle motion, and the longitudinal tire model are presented. The vehicle and powertrain controllers are developed. Finally, simulation results are presented for several control cases.

- In Chapter 5, a discussion of lateral vehicle motion and the lateral tire model are presented. The vehicle and powertrain controllers are developed using WOSA. Simulation results are presented for several control cases.
- In Chapter 6, NLMPC, FLC and SMC vehicle level controllers for lateral motion are designed and simulated.
- In Chapter 7, the four lateral motion vehicle level controllers (WOSA, NLMPC, FLC, SMC) are compared and contrasted.
- In Chapter 8, conclusions and future work are discussed.

CHAPTER TWO

EAWD MODEL DEVELOPMENT AND ASSUMPTIONS

2.1 Description of the eAWD powertrain

The heart of the eAWD powertrain is the electric motor assembly. The motor assembly consists of a traction motor which is responsible for transmitting torque to the right and left half shafts through a planetary gearset. Also, there is a small torque vectoring motor which is responsible for shifting torque between the half shafts as necessary through a secondary gearset. The torque vectoring motor adds a degree of freedom to the powertrain system. By shifting torque from one wheel to the other, vehicle stability can be improved during extreme driving conditions. The planetary gearset on each side provides torque transfer and multiplication from the motors to the half shafts. There is an electric motor assembly on the front and rear axle of the vehicle, which makes up the eAWD powertrain system. A pictorial representation of the motor assembly is presented in Figure 2.1. A schematic of the motor assembly is presented in Figure 2.2. The motor assembly described here is the same one that is described in [17]. In [17], the derivation of the dynamic equations for the motor system are done with a bond graph. Here, the equations are derived using free body diagrams and Newton's equations.

Specifications of the electric motor system

- 65 KW traction motor
- 6 KW torque vectoring motor

- 1000 Nm traction torque capacity at each wheel
- 600 Nm vectoring torque capacity at each wheel
- Dynamic front/rear and right/left torque split
- Traction and torque vectoring motors are independent

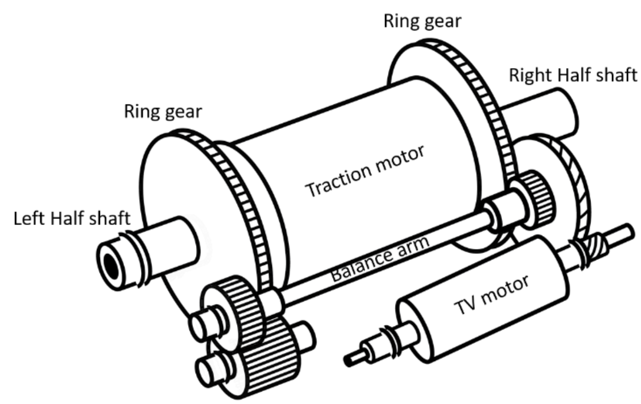

Figure 2.1 eAWD assembly

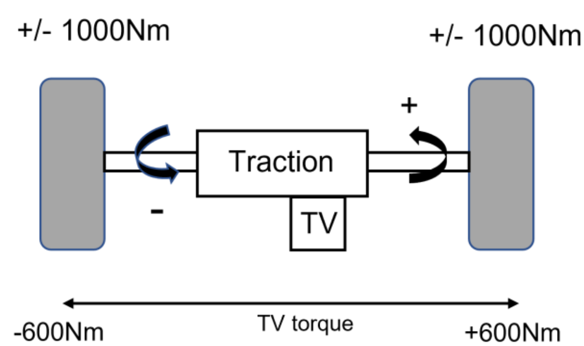

Figure 2.2   eAWD schematic
There is a motor on the front and rear axle of the vehicle

2.1.1 Planetary Gearset

Because the operation of the motor assembly in the eAWD powertrain relies on a planetary gearset to transmit torque to the wheels, a brief description of the gearset is provided here. A planetary gearset is a mechanism that allows for different gear ratios and speeds between the input and output shafts by changing which gears are allowed to rotate, and which gears are held steady. The system is contained in a compact package. A diagram of the planetary gearset is presented in Figure 2.3. The planetary gearset in relation to the eAWD motor assembly is presented in Figure 2.4. The configuration of the planetary gearset for the eAWD is presented in Figure 2.5.

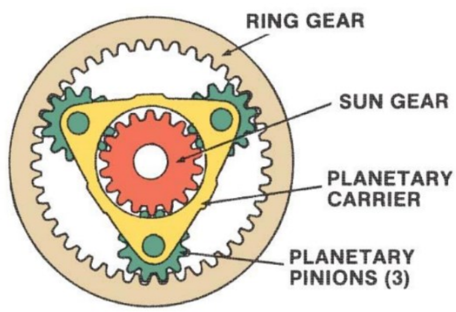

Figure 2.3 Planetary Gearset [23]

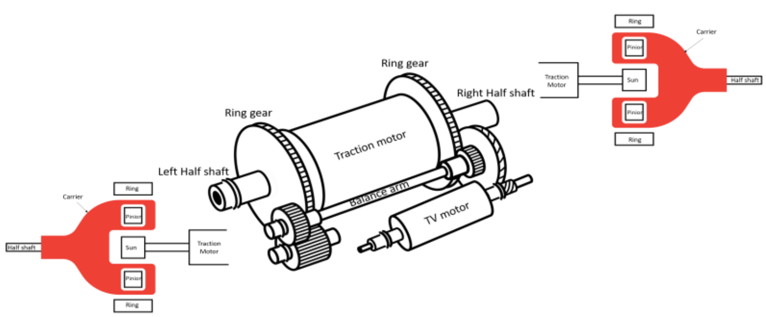

Figure 2.4 eAWD and Planetary Gearset

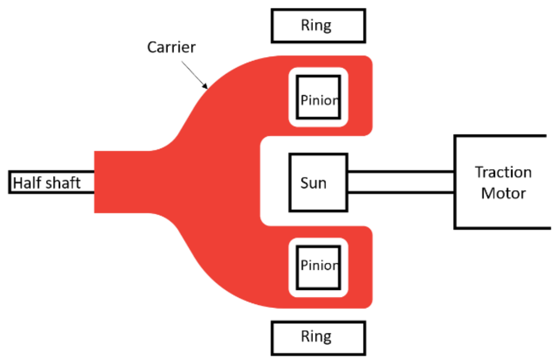

Figure 2.5 Planetary Gearset Configuration

2.2 Driving Cases

This section discusses how the motor assembly used in the eAWD operates in three important driving cases. The basic equation that represents the relative speeds between the components of the planetary gear set is presented in (2.1). This equation is applicable for the left and right side of the axle.

$$\omega_c = \frac{\rho}{(1+\rho)}\omega_s + \frac{1}{(1+\rho)}\omega_r \tag{2.1}$$

Where:

ω_c : Angular speed of carrier in rads/s

ω_s : Angular speed of sun gear in rads/s

ω_r : Angular speed of ring gear in rads/s

ρ : Gear ratio between sun gear and ring gear

Case 1 – Straight ahead driving

The traction motor outputs torque to the planetary gear set on the right and left sides. Because the vehicle is driving in a straight line and there is no speed differential between the two wheels, the balance arm keeps the ring gears from rotating. This concept is shown in Figure 2.6.

Case 2 – Cornering

As the vehicle turns a corner, the right and left wheels will want to rotate at different speeds. The balance arm rotates to adjust the speeds of the right and left ring gears and allow the right and left carriers to turn at different angular speeds (ω_{c_R}, ω_{c_R}). The balance arm and the planetary gear set work together to allow the motor system to act as an open differential. This concept is shown in Figure 2.7.

Case 3 – Torque vectoring motor is active

When the torque vectoring motor is active, it's angular speed modifies the angular speeds of the right and left carriers (ω_{c_R}, ω_{c_R}) through the action of the balancing bar. Modifying the angular speeds of the carriers corresponds to modifying the torque output at each half shaft. Note that the half shaft is connected to the carrier. This concept is shown in Figure 2.8.

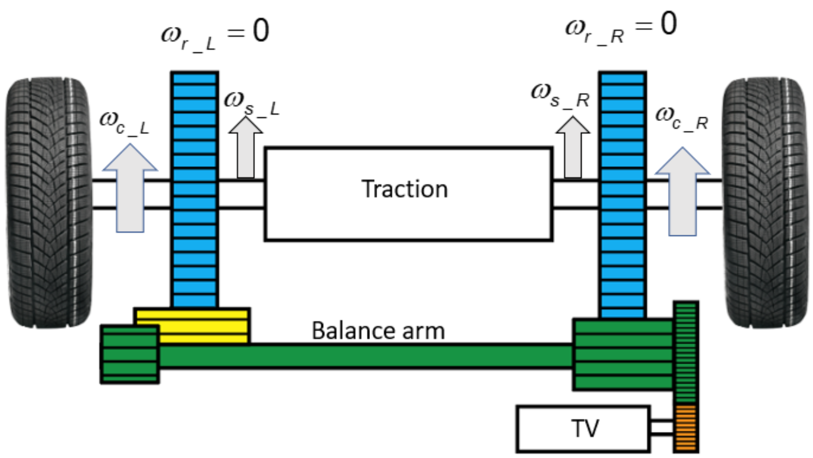

Figure 2.6 Driving Case 1. The angular speed of the ring gears is 0, and the right and left carriers turn at the same angular speed.

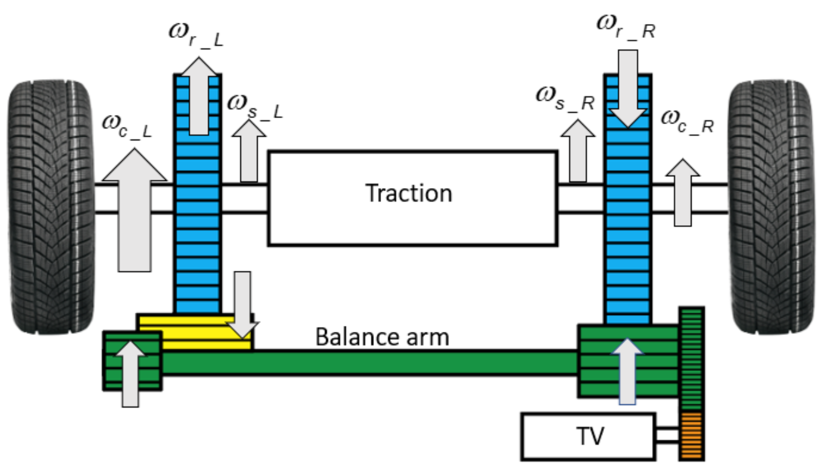

Figure 2.7 Driving Case 2. The vehicle is turning right, and the left wheel is turning at a faster angular speed than the right wheel.

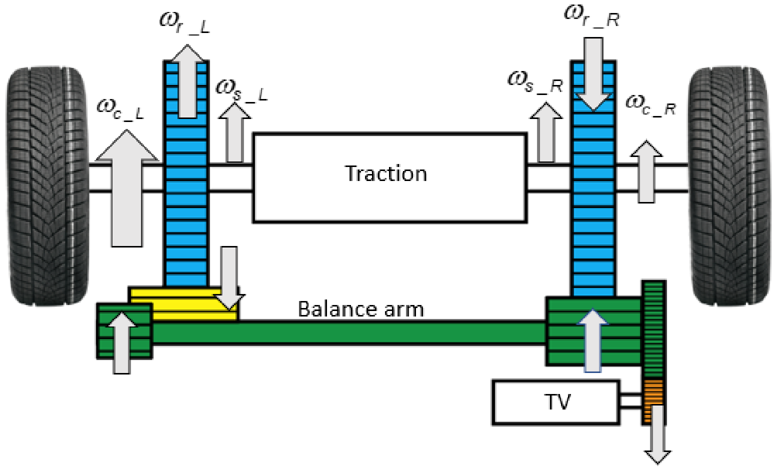

Figure 2.8 Driving Case 3. When the torque vectoring motor is active, it's rotational speed affects the rotational speed of the right and left carriers through the action of the balance arm.

2.3 Development of the eAWD Model

To develop the model of the eAWD system, some simplifying assumptions are made to keep the model within a reasonable scope. These assumptions are as follows:

- The masses of the carrier, ring gear and balance shaft are negligible relative to the masses of the traction and torque vectoring motor.
- Gear lash in the system is negligible.
- The only inertias in the system come from the traction motor, torque vectoring motor and the wheels.
- The only compliance in the system comes from the half shafts.

The free body diagram of the traction motor is presented in Figure 2.9 Applying Newton's law for angular acceleration (2.2), (2.3) can be derived from the free body diagram.

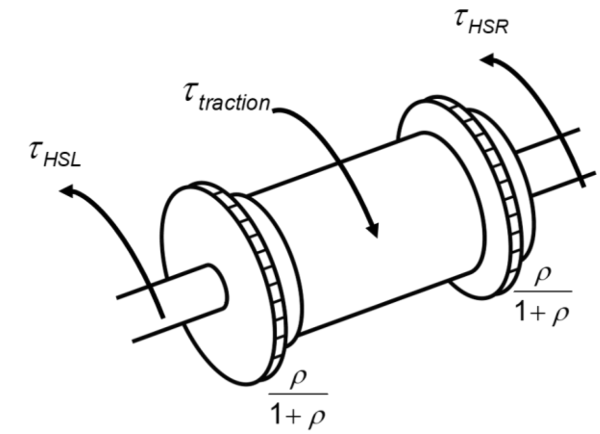

Figure 2.9 Free body diagram for the traction motor

$$\dot{\omega} = \frac{\tau_{\text{resultant}}}{J} \tag{2.2}$$

$$\dot{\omega}_{traction} = \frac{1}{J_{trac}}\left(\tau_{traction} - \frac{\rho}{(1+\rho)}\left(\tau_{HSL} + \tau_{HSR}\right)\right) \tag{2.3}$$

Note: $\tau_s = \frac{\rho}{(1+\rho)}\tau_c$ is the torque ratio between the sun gear (which connects to the traction motor output) and the carrier (which connects to the half shaft).

The free body diagram of the torque vectoring motor is presented in Figure 2.10. Applying Newton's law (2.2) yields (2.4).

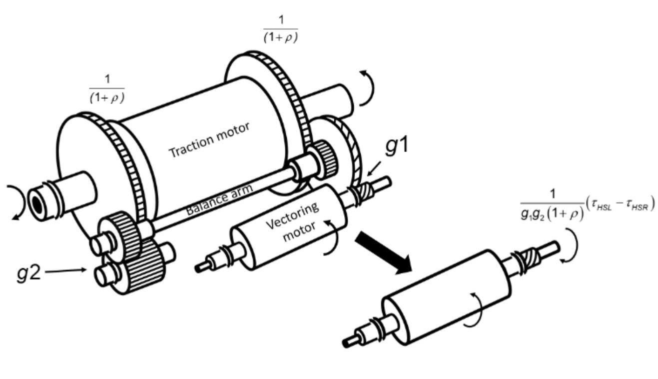

Figure 2.10 Free body diagram for the torque vectoring motor

$$\dot{\omega}_{TV} = \frac{1}{J_{TV}}\left(\tau_{TV} - \frac{1}{g_1 g_2 (1+\rho)}(\tau_{HSL} - \tau_{HSR})\right) \tag{2.4}$$

Note: $\tau_r = \frac{1}{(1+\rho)}\tau_c$ is the torque ratio between the ring gear and the carrier which is connected to the half shafts.

The half shafts will experience a torsional load from the motor inputs and the wheel, which generate (2.5) and (2.6).

$$\dot{\theta}_{HSL} = \frac{\rho}{1+\rho}\omega_{Traction} - \frac{1}{g_1 g_2 (1+\rho)}\omega_{TV} - \omega_{wL} \tag{2.5}$$

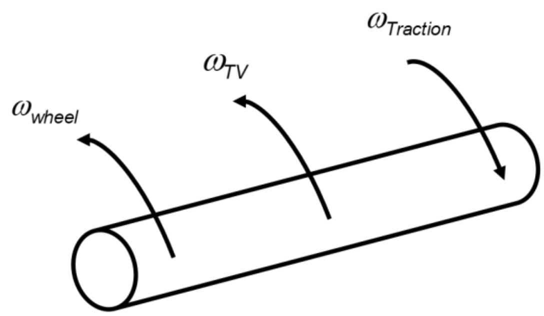

Figure 2.11 Free body diagram of the left half shaft

$$\dot{\theta}_{HSR} = \frac{\rho}{1+\rho}\omega_{Traction} + \frac{1}{g_1 g_2 (1+\rho)}\omega_{TV} - \omega_{wR} \tag{2.6}$$

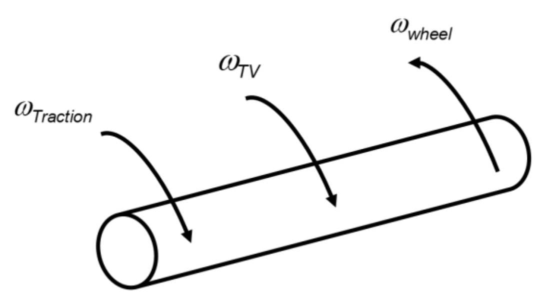

Figure 2.12 Free body diagram of the right half shaft

Note that the half shafts will experience a torsional load because the traction motor and torque vectoring motor will be operating at different angular velocities. As a result, the half shaft torques are calculated based on the principle of a rotational spring, (2.7), (2.8).

$$\tau_{HSL} = K\theta_{HSL} + b\dot{\theta}_{HSL} \tag{2.7}$$

$$\tau_{HSR} = K\theta_{HSR} + b\dot{\theta}_{HSR} \tag{2.8}$$

The angular acceleration of the wheels is given by (2.9) and (2.10) which are based on the free body diagram of a wheel shown in Figure 2.13.

$$\dot{\omega}_{WSL} = \frac{1}{J}\left(\tau_{HSL} - R_w F_{xL}\right) \tag{2.9}$$

$$\dot{\omega}_{WSR} = \frac{1}{J}\left(\tau_{HSR} - R_w F_{xR}\right) \tag{2.10}$$

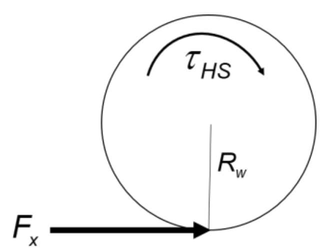

Figure 2.13 Free Body Diagram of Wheel

The collection of the eAWD equations represents the dynamic model of the system, (2.11) to (2.16). These equations apply to the front and rear axle of the vehicle.

$$\dot{\omega}_{traction} = \frac{1}{J_{trac}}\left(\tau_{traction} - \frac{\rho}{(1+\rho)}\left(\tau_{HSL} + \tau_{HSR}\right)\right) \tag{2.11}$$

$$\dot{\omega}_{TV} = \frac{1}{J_{TV}}\left(\tau_{TV} - \frac{1}{g_1 g_2 (1+\rho)}\left(\tau_{HSL} - \tau_{HSR}\right)\right) \tag{2.12}$$

$$\dot{\theta}_{HSL} = \frac{\rho}{1+\rho}\omega_{Traction} - \frac{1}{g_1 g_2 (1+\rho)}\omega_{TV} - \omega_{wL} \tag{2.13}$$

$$\dot{\theta}_{HSR} = \frac{\rho}{1+\rho}\omega_{Traction} + \frac{1}{g_1 g_2 (1+\rho)}\omega_{TV} - \omega_{wR} \tag{2.14}$$

$$\dot{\omega}_{WSL} = \frac{1}{J_W}\left(\tau_{HSL} - R_w F_{xL}\right) \tag{2.15}$$

$$\dot{\omega}_{WSR} = \frac{1}{J_W}\left(\tau_{HSR} - R_w F_{xR}\right) \tag{2.16}$$

Table 2.1 Definitions of the eAWD state variables

State variable	Units	Definition
$\omega_{traction}$	rad/s	Rotational speed of traction motor
ω_{TV}	rad/s	Rotational speed of torque vectoring motor
θ_{HSL}	radians	Angle rotation of left half shaft
θ_{HSR}	radians	Angle rotation of right half shaft
ω_{WSL}	radians	Rotational speed of left wheel
ω_{WSR}	rad/s	Rotational speed of right wheel
τ_{HSL}	Nm	Left half shaft torque
τ_{HSR}	Nm	Right half shaft torque

Table 2.2 Definitions of the eAWD model parameters

Parameter	Definition
J_{Trac}	Traction motor moment of inertia
J_{TV}	Torque vectoring motor moment of inertia
J_w	Wheel moment of inertia
K	Half shaft torsional spring constant
b	Half shaft torsional damping constant

2.4 Simulation Integration with CarSim and Simulink

The control strategies discussed in this thesis are developed and simulated using Simulink and CarSim. The overall controller is implemented in Simulink, and half shaft torques are calculated in Simulink and imported into CarSim. A diagram of this structure is shown in Figure 2.14. A D-class sedan from CarSim is the plant model as shown in Figure 2.15. CarSim calculates all the vehicle parameters and exports those back into Simulink, shown in Figure 2.16.

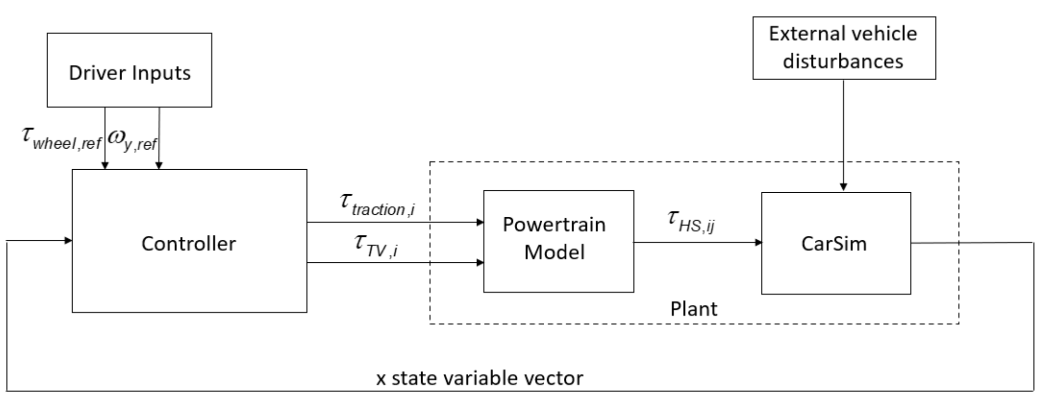

Figure 2.14 Control Diagram for eAWD Powertrain

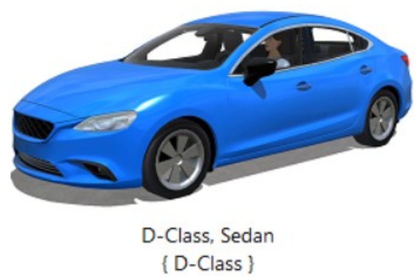

Figure 2.15 CarSim vehicle

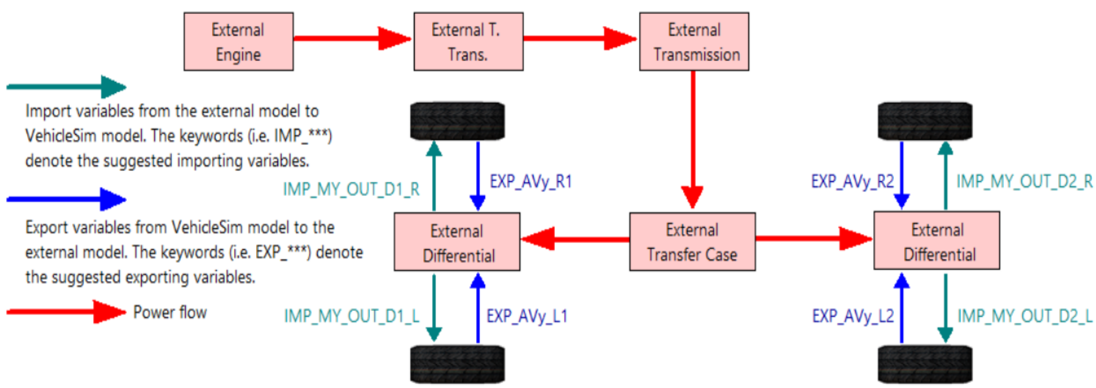

Figure 2.16 CarSim Interface with Simulink

It should be noted that coordination with the vehicle braking system is not considered in this thesis. Driver input comes only from the accelerator pedal and steering wheel. The controller only has authority of the torque commands to the electric motors.

CHAPTER THREE

DEVELOPMENT OF WEIGHTED ONE STEP AHEAD CONTROLLER

The weighted one step ahead (WOSA) controller calculates the control input to minimize the predicted error one time step into the future. This controller has the advantage of being relatively straightforward to implement, yet provides very good tracking of the reference signal. In this thesis, two forms of the weighted one step ahead controller are used. In section 3.1, a general WOSA controller is developed for a linear system. In section 3.2, a general WOSA controller is developed for a non linear system [24].

3.1 Linear Control Case

Here, a WOSA controller is developed for the general control case for a linear state space system. This controller will be used to implement the longitudinal vehicle controller discussed in Chapter 4, and the traction and torque vectoring motor controllers discussed in Chapters 4 and 5. It will also be used to implement the controller output observers (COO) that will be discussed in Chapters 4 and 5.

Consider a general MIMO state space system.

$$\dot{x}(t) = Ax(t) + Bu(t) \tag{3.1}$$

$$y(t) = Cx(t) + Du(t) \tag{3.2}$$

Using Euler's method, the state space equations can be discretized, (3.3) and (3.4).

$$x_{k+1} = x_k + t_s(Ax_k + Bu_k) \tag{3.3}$$

$$y_k = Cx_k + Du_k \tag{3.4}$$

The discrete system is rewritten in (3.5) and (3.6).

$$x_{x+1} = \bar{A}x_k + \bar{B}u_k \tag{3.5}$$

$$y_k = Cx_k + Du_k \tag{3.6}$$

Where

$\bar{A} = (I + t_s A)$

and

$\bar{B} = t_s B$

and t_s is the sampling interval for the discrete system.

The goal of the controller is to calculate u_k such that $\hat{y}_{k+1} = y^*_{k+1}$ where y^*_{k+1} is the reference at the next sample time and $\hat{y}_{k+1}$ is the predicted output. So, (3.6) is rewritten to represent the predicted output using the input at the current sample time, which is presented in (3.7).

$$\hat{y}_{k+1} = Cx_{k+1} + Du_k \tag{3.7}$$

Plugging (3.5) into (3.7) yields (3.8).

$$\hat{y}_{k+1} = C\bar{A}x_k + C\bar{B}u_k + Du_k \tag{3.8}$$

The output error at the next sample time is given by (3.9) and (3.10).

$$e_{k+1} = \hat{y}_{k+1} - y^*_{k+1} \tag{3.9}$$

$$e_{k+1} = C\bar{A}x_k + C\bar{B}u_k + Du_k - y^*_{k+1} \tag{3.10}$$

The objective function is defined in (3.11).

$$J = \frac{1}{2} e_{K+1}^T Q e_{k+1} + \frac{1}{2} u_k^T R u_k \tag{3.11}$$

The first term of this function minimizes the tracking error, and the second term limits the control input. The matrices Q and R are weights placed on the tracking error and input respectively. Also, Q and R are assumed to be symmetric and positive semidefinite.

The partial derivative of (3.11) with respect to u_k is given in (3.12).

$$\frac{\partial J}{\partial u_k} = \frac{\partial (e_{k+1})^T}{\partial u_k} Q(e_{k+1)}) + Ru_k \tag{3.12}$$

Where:

$$\frac{\partial (e_{k+1})}{\partial u_k} = \frac{\partial (C\bar{A}x_k + C\bar{B}u_k + Du_k - y_{k+1}^*)}{\partial u_k} = (C\bar{B} + D) \tag{3.13}$$

Plugging (3.10) and (3.13) into equation (3.12) results in (3.14). Solving equation (3.14) for the input at the current sample time, u_k, yields (3.15), which is the control law.

$$\frac{\partial J}{\partial u_k} = (C\bar{B} + D)^T Q(C\bar{A}x_k + C\bar{B}u_k + Du_k - y_{k+1}^*) + Ru_k = 0 \tag{3.14}$$

$$u_k = (((C\bar{B})^T QC\bar{B} + 2(C\bar{B})^T D + D^T D) + R)^{-1} (C\bar{B} + D)^T Q(y_{k+1}^* - C\bar{A}x_k) \tag{3.15}$$

3.2 Nonlinear Control Case

Here, the WOSA controller is developed for a general nonlinear system. This controller is implemented for the lateral motion vehicle controller discussed in Chapter 5. Assume a nonlinear system.

$$\dot{x}(t) = f(x(t)) + Bu(t) \tag{3.16}$$

$$y(t) = Cx(t) + Du(t) \tag{3.17}$$

The system can be discretized using Euler's method.

$$x_{k+1} = x_x + t_s(f(x_k) + Bu_k) \tag{3.18}$$

$$y_k = Cx_k + Du_k \tag{3.19}$$

Rewriting equation (3.19) to represent the predicted output at the next sample time using the current input yields (3.20)

$$\hat{y}_{k+1} = Cx_{x+1} + Du_k \tag{3.20}$$

Substituting equation (3.18) into (3.20) yields (3.21).

$$\hat{y}_{k+1} = C(x_x + t_s(f(x_k) + Bu_k)) + Du_k \tag{3.21}$$

The predicted error is defined in (3.22).

$$e_{k+1} = y^*_{k+1} - \hat{y}_{k+1} \tag{3.22}$$

Where y^*_{k+1} is the reference at the next sample time.

The objective function is presented in (3.23).

$$J = \frac{1}{2}e^T_{k+1}Qe_{k+1} + \frac{1}{2}u^T_k Ru_k \tag{3.23}$$

Where Q is a weighting matrix for the system output, and R is a weighting matrix for the system input. Also, Q and R are assumed to be symmetric and positive semidefinite.

Taking the partial derivative for (3.23) with respect to u_k yields (3.24).

$$\frac{\partial J}{\partial u_k} = \frac{\partial e^T_{k+1}}{\partial u_k}Qe_{k+1} + Ru_k \tag{3.24}$$

Where:

$$\frac{\partial e_{k+1}^T}{\partial u_k} = \frac{\partial (y_{k+1}^* - C(x_x + t_s(f(x_k) + Bu_k)) + Du_k)^T}{\partial u_k} = -(C(t_s B + D))^T \tag{3.25}$$

Plugging (3.21),(3.22) and (3.25) into (3.24) yields (3.26).

$$\frac{\partial J}{\partial u_k} = -(C(t_s B + D))^T Q(y_{k+1}^* - C(x_k + t_s(f(x_k) + Bu_k)) + Du_k) + Ru_k \tag{3.26}$$

Setting (3.26) equal to 0 and solving for u_k yields (3.27).

$$\begin{aligned} u_k &= (t_s^2(B^T C^T QCB) + 2t_s B^T C^T QCD + D^T C^T QCD + R)^{-1} \ldots \\ &(t_s B^T + D^T)C^T Q(y_{k+1}^* - Cx_k - t_s C(f(x_k)) \end{aligned}$$

(3.27)

CHAPTER FOUR

LONGITUDINAL MOTION CONTROL

4.1 Introduction

This chapter considers two key driving scenarios for controlling the longitudinal motion of the vehicle: Launching the vehicle and tracking the driver traction force request on a high friction road surface, and launching on a low friction road surface. These driving scenarios involve distributing the motor torque commands between the front and rear axles to maintain vehicle stability, and preventing wheel slip to maximize the available traction force.

4.1.1 Literature Review on Torque Allocation

In [25], an adaptive cruise control (ACC) system for an electric vehicle is studied. It's necessary for the ACC to track the requested acceleration from the driver. This requires the controller to determine the appropriate torque commands for each electric motor to track the requested acceleration. A self tuning PID controller is used, where the tuning mechanism is a neural network (NN). The NN is trained online during vehicle operation and is able to adjust the PID parameters based on operating conditions. In [26], an unconstrained optimization strategy is used to allocate motor torque commands to the front and rear axles based on minimizing the tire slip ratios.

Other researchers have used fuzzy rule strategies to accomplish the appropriate distribution of torque between the front and rear axles or between the in-hub motors as discussed in section 1.4.

This thesis takes a different approach than what is typically done for allocating the motor torque commands. First a WOSA controller is used to track the traction force reference, a fuzzy logic rule set is used to assign torque requests to the front and rear traction motors, then a secondary control loop employing fuzzy rules is used to adjust the motor torque commands to improve the tracking of the traction force request. The main advantage of this control strategy is that it's effective, relatively simple to implement, and the fuzzy rules rely on human understanding of how the system should operate rather than a complex mathematical model.

4.1.2 Literature review on Wheel Slip Control

When the vehicle is launching, accelerating or braking, it's important to prevent wheel slip to maintain the highest level of traction possible and prevent the vehicle from becoming unstable. This is especially true on a low friction road surface. Researchers have proposed several solutions to this problem for EV vehicles.

Reference [27] controls wheel slip by first estimating the coefficient of friction of the road surface. Then a sliding mode control strategy is used to adjust the motor torque commands to ensure the vehicle operates in the maximum friction zone. This control strategy relies on a fairly complex process to estimate the friction coefficient and an online Pacejka tire model.

Reference [28] uses a NLMPC strategy to calculate the motor torques necessary to maintain a predefined desired slip ratio. This strategy uses an online Pacejka tire model to calculate the necessary tire forces. Also, there are three weighting matrices that have to be tuned. In [29], a NLMPC is also used. This NLMPC strategy calculates the optimal values for several parameters of a multimachine electric motor structure. What's interesting about this approach is that the weighting factors for the objective function are calculated online using fuzzy rules which take into account the vehicle operating conditions.

This thesis addresses wheel slip control in the driving case of launching on a low friction road surface. In this case, it is necessary to adjust motor torque commands to maintain a desired wheel slip ratio. This is done by using a fuzzy rule control strategy. The fuzzy rule strategy does not rely on estimating the coefficient of friction which is very difficult to do in real time. It also does not rely on an online tire model to calculate tire forces. It's simpler to implement versus NLMPC strategies.

4.1.3 Literature Review on Longitudinal Velocity and Tire Force Estimation

As part of the overall control strategy for longitudinal motion, estimates of the tire longitudinal tire force and vehicle speed are necessary.

The Kalman filter (KF) and extended Kalman filter (EKF) are popular ways of estimating vehicle state parameters, and the literature has many examples. One particular interesting use of the EKF is presented in [30]. Here, two EKF's are used in tandem. One EKF is used to estimate the vehicle state variables, the other is used to estimate the system parameters. Amongst the estimated values are the longitudinal tire forces and the longitudinal vehicle speed. The disadvantage of this approach is that it relies heavily on a detailed vehicle model and tire model. Also, it is necessary to provide four covariance matrices, two process and two noise output.

In [31], an EKF is used to estimate the longitudinal tire forces. Similar to the previous discussion of the tandem EKF, this requires the use of a detailed vehicle model and tire model.

In [32], a KF is used to estimate the vehicle speed from a wheel speed sensor and a vehicle accelerometer, and fuzzy rules are used to adjust the covariances matrix for the KF to rely more on the wheel speed sensor or accelerometer depending on the level of wheel slip.

In [17], a controller output observer (COO) is used to estimate longitudinal vehicle speed and tire forces. This observer uses an estimation model as the plant to be controlled. The control inputs into the estimation model are the longitudinal tire forces, and the output is the vehicle acceleration which gets integrated to estimate the longitudinal vehicle speed. The COO relies only on the measured longitudinal acceleration which is readily available. The control strategy that is used is the Youla parameterization method. This thesis uses a COO strategy similar to that presented in [17] to estimate the longitudinal tire force and speed. However, the controller is a WOSA.

4.1.4 Brief Discussion of Fuzzy Logic

This thesis uses the concept of fuzzy logic rules coupled with a controller designed from a physical plant model of the vehicle to create an integrated vehicle controller strategy. As such, it is important to briefly discuss some key concepts for fuzzy logic.

Fuzzy logic is used in situations where the relationship between the input variable and the output variable cannot be easily represented with a mathematical model. Human understanding of the relationship is used to represent that relationship, and is captured in the fuzzy inference system. Fuzzy logic is often thought of as a form of artificial intelligence because it captures human knowledge to make decisions about or control a process that does not have a mathematical formulation. In Figure 4.1, a fuzzy control scheme is represented. The fuzzy inference system uses human knowledge based rules to represent the relationship between the reference input and what the actuator signal should be to control the plant.

The fuzzy inference system works by taking a "crisp" input value and converting that into an input fuzzy variable by assigning it to one or more input membership functions. This process is called fuzzification. Then the appropriate fuzzy rule is applied to assign the output value to one or more output membership functions. The new variable is called the output fuzzy variable. Finally, the output fuzzy variable is converted into a crisp number. This concept is presented in Figure 4.2.

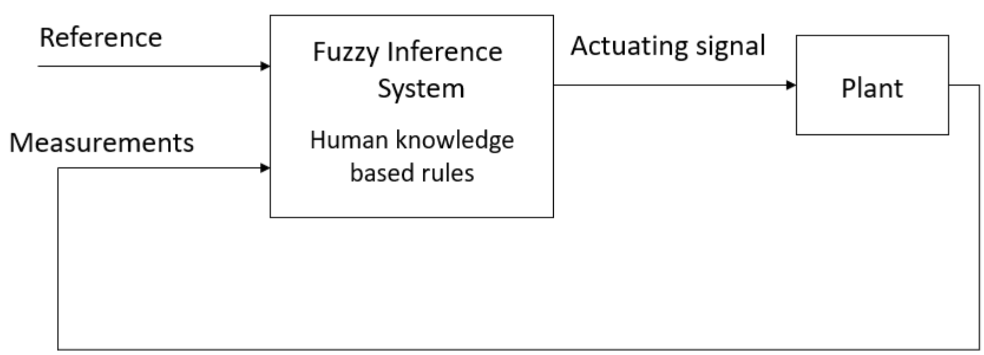

Figure 4.1 Fuzzy inference system for a plant controller

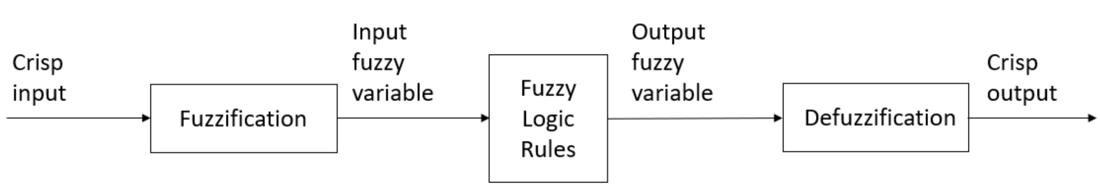

Figure 4.2 Fuzzification and defuzzification process

A simple illustration of how the crisp input is converted into the crisp output is presented in Figure 4.3. Note that the membership functions have descriptive names which help simplify the process of designing the fuzzy inference system. Also the membership functions can be designed based on human knowledge/judgement or based on data from the system or process.

In the interest of briefness, the process of fuzzification and defuzzification is not presented here. There are many sources which explain that process [7].

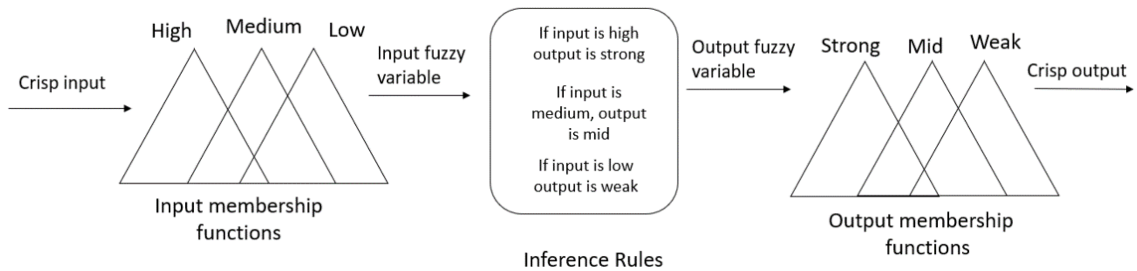

Figure 4.3 The process of fuzzification and defuzzification

4.1.5 Outline Of the Rest Of the Chapter

In the rest of the chapter, important concepts of longitudinal vehicle motion are presented. First, longitudinal tire dynamics are discussed including tire slip and tire forces. Estimation of key vehicle parameters using a COO observer are discussed. Then the WOSA controller and integrated fuzzy logic rules are presented to control the vehicle during launch on a high friction and low friction road surface. Finally, simulation results for all of the discussed driving cases are presented.

4.2 Longitudinal Tire Dynamics

For longitudinal driving, a very simple vehicle motion model is presented in (4.1) which is based on Newton's second law. This model assumes a total traction force, F_x, for the front and rear axles. A diagram of the vehicle model is presented in Figure 4.4.

$$\dot{V}_x = \frac{(F_{x,f} + F_{x,r})}{m} = \frac{F_x}{m} \tag{4.1}$$

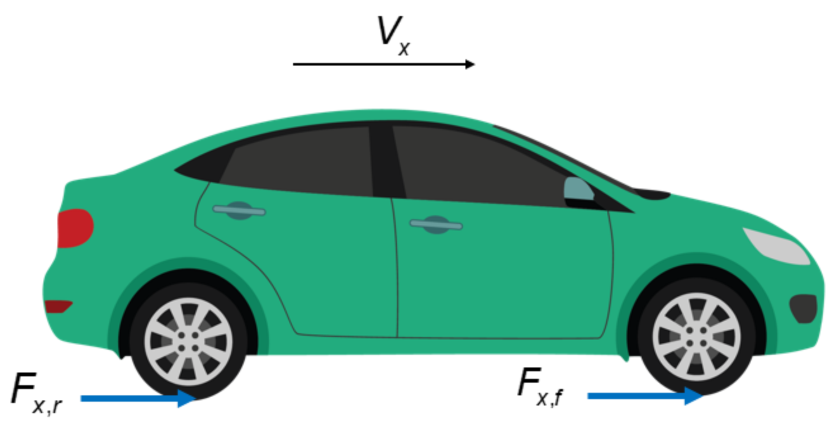

Figure 4.4 Longitudinl tire forces

The traction force, F_x, is the reaction force of the road surface to the tire as the vehicle is propelled forward (or backwards). The traction force arrows point in the direction that the vehicle is moving. The traction force is created because the part of the tire that comes into contact with the road surface wants to grip the road when a torque is applied to the wheel. The grip creates a minute deformation in the tire which in turn generates a reaction force from the road in the direction opposite of the applied torque, Figure 4.5.

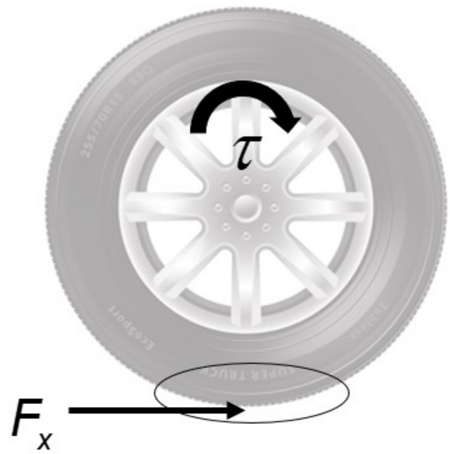

Figure 4.5 Traction force is a reaction of the applied torque

The magnitude of the traction force depends on slip ratio, the normal load of the vehicle on the tire, and the friction coefficient of the road surface. Each of these items is discussed below.

4.2.1 Slip Ratio

The slip ratio is the difference between the longitudinal velocity (V_x) and the velocity of the wheel ($R_w\omega$). If the vehicle is accelerating, the slip ratio is given in (4.2).

$$\sigma_x = \frac{R_w\omega - V_x}{R_w\omega} \tag{4.2}$$

If the vehicle is decelerating, the slip ratio is given in (4.3).

$$\sigma_x = \frac{V_x - R_w\omega}{V_x} \tag{4.3}$$

The slip ratio is related to the tire deformation at the contact patch. Figure 4.6 shows the acceleration case. When a positive torque is applied, the rotational velocity of the tire ($R_W\omega$) is faster than the longitudinal velocity at the center of the tire, V_x. This is because the tire grip at the road surface causes a slight deformation of the tire at the tire patch. So the net velocity at the tire patch is $R_w\omega - V_x$ and is in the opposite direction of V_x. The slip ratio is calculated by dividing the net longitudinal velocity by the rotational velocity in the case of acceleration. A similar concept is applied for understanding the slip ratio for the braking case.

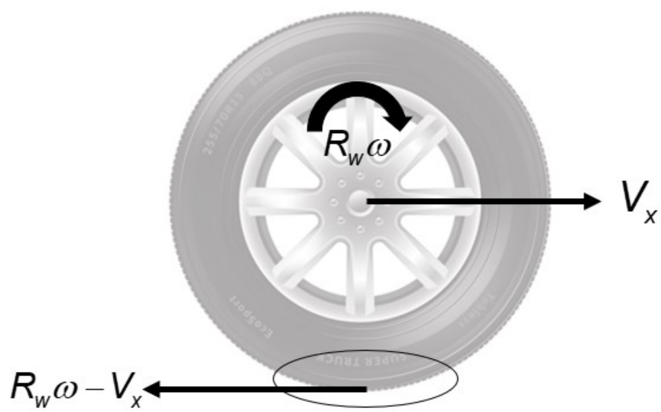

Figure 4.6 Slip ratio for acceleration

Under ideal conditions when the road surface friction coefficient is 1, and the slip ratio is small (less than 0.10) the tire traction force will have a linear relationship with the slip ratio. The relationship between the traction force and wheel slip is shown in Figure 4.7. In the linear region of the force-slip curve in Figure 4.7, the traction force is given by (4.4).

$$F_x = C_x \sigma_x \tag{4.4}$$

The parameter C_x is called the longitudinal tire stiffness and is in units of N. Equation (4.4) applies to both the front and rear axles.

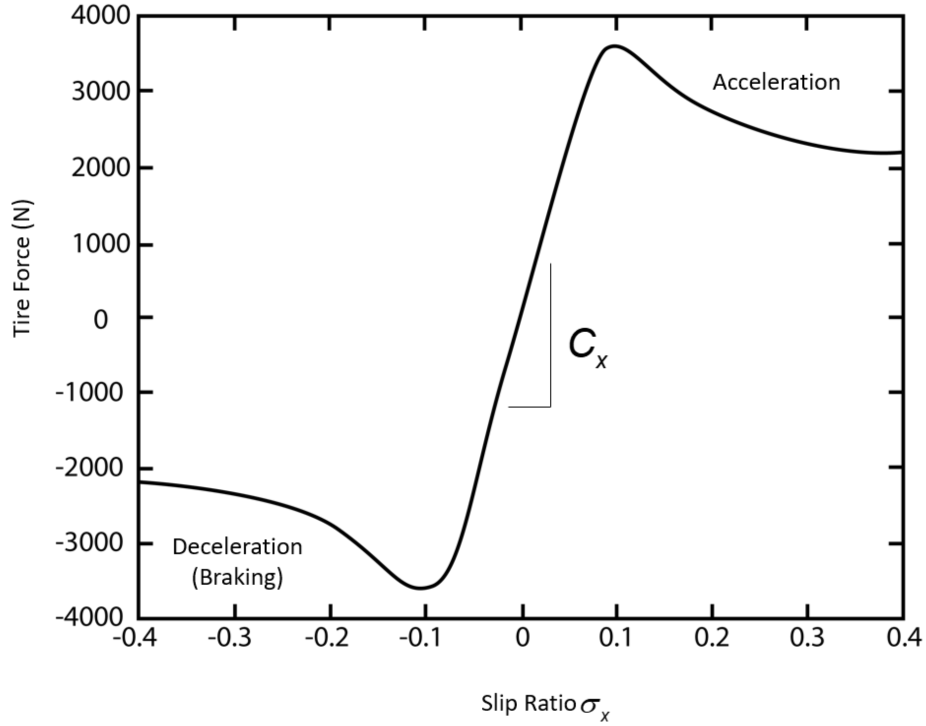

Figure 4.7 Traction force is a function of slip ratio.

When the tire has been saturated, the operating point of the vehicle is in the nonlinear range of the force-slip curve. In this case, tire grip is reduced and the vehicle may become unstable. The goal of the control system is to ensure that the vehicle operates in the linear region of the force-slip curve as much as possible.

4.2.2 Normal Tire Force and Friction Coefficient

The normal tire force represents the reaction force of the road to the tire based on the vehicle weight over that tire. When the vehicle decelerates, the weight of the vehicle shifts from the rear to the front. The opposite happens when the vehicle acclerates.

That means the normal tire force shifts as the vehicle weight shifts. The relationship between the traction force and the normal tire force is given in (4.5), where μ is the coefficient of friction between the tire and the road.

$$F_x = \mu F_z \tag{4.5}$$

When the value of μ changes, the shape of the slip-friction curve changes as well. Figure 4.8 shows typical curves for this relationship. On a slippery road surface, the available traction force will be reduced, which means that it is important for the system controller to try to maximize the amount of traction force that is generated and account for low coefficient of friction. Figure 4.9 shows a vehicle with the normal forces at the front and rear axles.

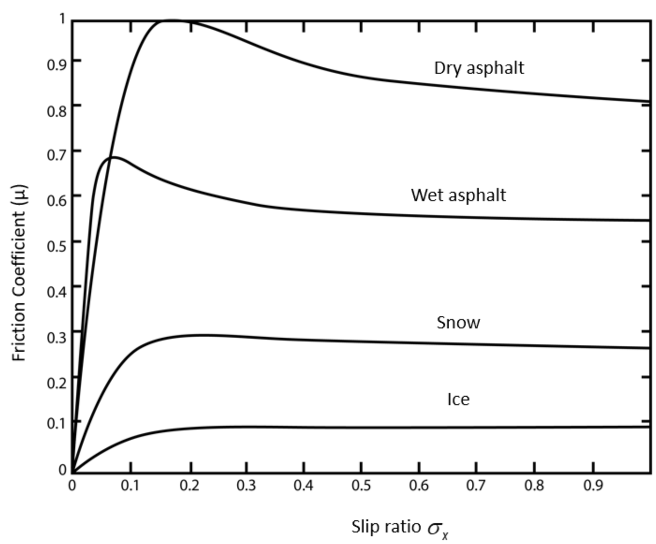

Figure 4.8 Typical friction-slip curves for different road surfaces

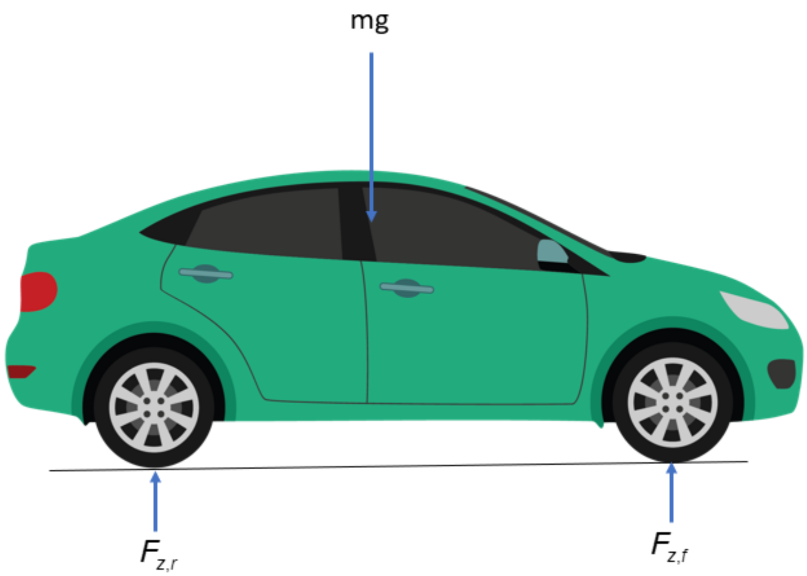

Figure 4.9 Normal tire forces at the front and rear axles

4.3 Vehicle Controller for Longitudinal Motion

4.3.1 Control System Framework

The overall control framework for longitudinal vehicle motion is presented in Figure 4.10. At the vehicle level, the driver inputs a traction force target by applying the accelerator pedal. A fuzzy logic rule set is used to split the traction force target between the front axle and rear axle based on the longitudinal acceleration. Next, a feedback loop is used to adjust the traction motor torque request to improve the overall tracking to the traction force target using a fuzzy rule set. To prevent tire saturation on a low friction road surface, a fuzzy logic rule control strategy is implemented to automatically adjust the traction force to reduce wheel slip. This allows the vehicle to maintain the maximum amount of traction force for the driving condition.

At the motor level, the target tire forces are converted to traction motor torque commands for the eAWD system by the motor controller which uses a WOSA strategy. The eAWD system converts the motor torque commands into halfshaft torque commands for the CarSim model.

Feedback from CarSim includes the longitudinal acceleration, which is fed into the fuzzy rule block to calculate the traction motor split between the front and rear axles. Also, the traction force feedback is estimated using wheel speeds from CarSim.

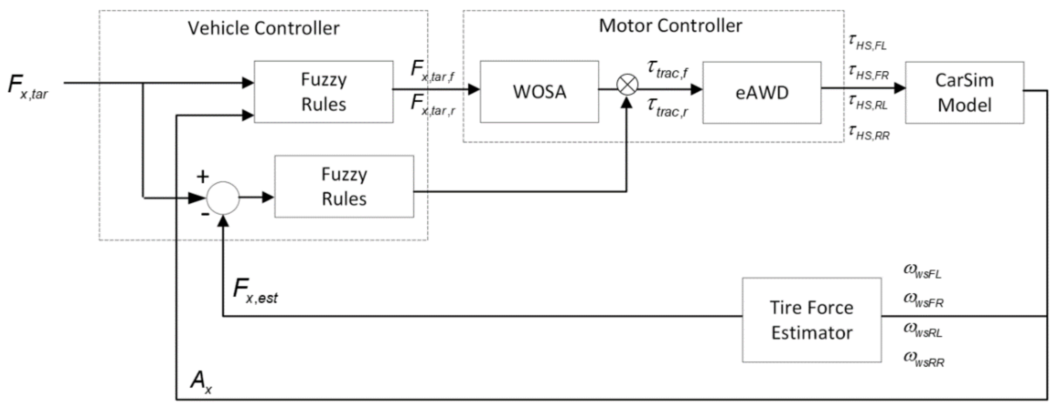

Figure 4.10 Longitudinal Motion Controller Framework

4.3.2 Vehicle Level Controller Design

The vehicle motion model for control design is based on the well-known bicycle model which is presented in Figure 4.11. In this model, the tires on each axle are represented with a single tire at the front and rear of the vehicle.

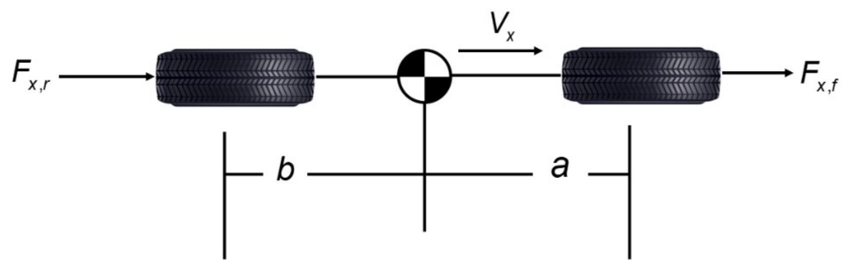

Figure 4.11 Bicycle model for longitudinal dynamics

The dynamic model of this system is presented in (4.6). The model is based on Newton's second law, and *m* is the vehicle mass.

$$\dot{V}_x = \frac{F_{x,f} + F_{x,r}}{m} = \frac{F_x}{m} \tag{4.6}$$

When the driver applies or removes pressure from the accelerator pedal, the control system interprets the pedal position as a total traction force target. This is the reference input for the control system, and is designated as $F_{x,tar}$. This is a total traction force reference for the front and rear axles combined. Because the control input for the system is total traction force, F_x, there is a feedforward term in the formulation of the state space system, which is presented in equations (4.7) and (4.8)

$$\dot{x}(t) = Ax(t) + Bu(t) \tag{4.7}$$

$$y(t) = Cx(t) + Du(t) \tag{4.8}$$

Applying the Euler method, (4.7) and (4.8) are transformed into a discrete state space system presented in (4.9) and (4.10).

$$x_{k+1} = x_k + t_s(Ax_k + Bu_k) \tag{4.9}$$

$$y_k = Cx_k + Du_k \tag{4.10}$$

For this system, the state variable is V_x and the control input is F_x. Also, $A = 0$, and $C = 0$. Hence, (4.9) and (4.10) can be rewritten as (4.11) and (4.12).

$$x_{k+1} = \bar{A}x_k + \bar{B}u_k \tag{4.11}$$

$$\hat{y}_{k+1} = Du_k \tag{4.12}$$

Where:

$x_k = [V_{x,k}]$

$u_k = \left[F_{x,k}\right]$

and

$\bar{A} = [1]$

$\bar{B} = t_s\left[\frac{1}{m}\right]$

$D = \left[\frac{1}{m}\right]$

Plugging these values into equations (3.7) through (3.15) to calculate the WOSA control input , u_k, the result is presented in equation (4.13).

$$u_k = \left(Q + R\right)^{-1}\left(Qy^*_{k+1}\right) \tag{4.13}$$

Setting $Q = 1$ and $R = 0$, the control input is presented in (4.14).

$$u_k = y^*_{k+1} \tag{4.14}$$

Where $u_k = F_{x,k}$ and $y^*_{k+1} = F_{x,tar,k}$.

For the case of longitudinal motion, the WOSA controller calculates the control input to be the reference traction tire force, $F_{x,tar}$. Hence, for control purposes, the driver input from the accelerator pedal will be treated as the traction force target.

4.4 Front/Rear split

It's important to be able to dynamically shift the traction force request between the front and rear axles for improved traction when the vehicle is accelerating and decelerating. To accomplish this, the vehicle level controller takes the traction force target and divides it into separate targets for the front and rear traction motors using an online fuzzy rule set. When the vehicle is speeding up, vehicle weight is shifted to the rear axle, hence more traction force is needed at the rear wheels. When the vehicle is slowing down, weight is shifted to the front axle, hence more traction force is needed at the front wheels. The fuzzy rule set looks at the longitudinal acceleration, A_x, and uses that value to calculate a weight shifting factor for the front and rear axles. This concept is shown in Figures 4.12 and 4.13. The fuzzy rule set can be calibrated to change the traction force split between the front and rear based on desired vehicle performance. The implementation of this strategy is presented in section 4.8.1.1.

4.5 Feedback Loop for Tracking the Fx Target

To improve the tracking performance of the vehicle level controller, an on-line fuzzy rule set is employed to adjust the traction motor torques to reduce the error between

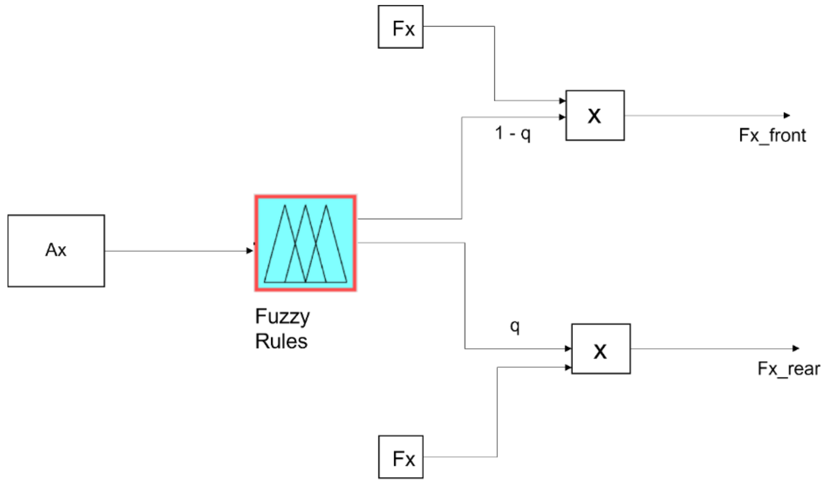

Figure 4.12 Fuzzy logic strategy for front/rear split

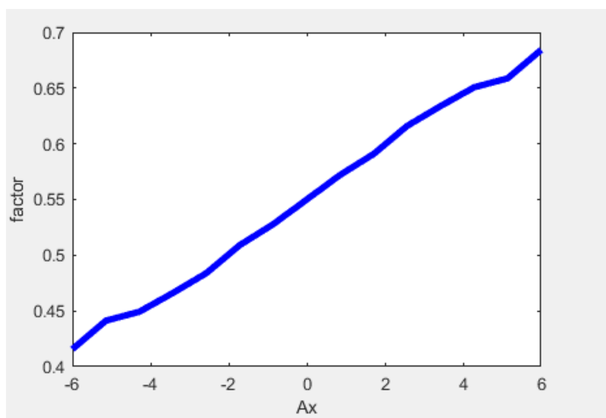

Figure 4.13 Fuzzy rule relationship between Ax and the adjustment factor front/rear split

the traction force target and the feedback traction force estimated from the wheel speeds (discussed in section 4.7.1). Essentially, the fuzzy rules reduce the motor torque when the feedback traction force is greater than the target traction force and increases the traction motor torque when the feedback traction force is less than the target traction force. This concept is shown in Figures 4.14 and 4.15.

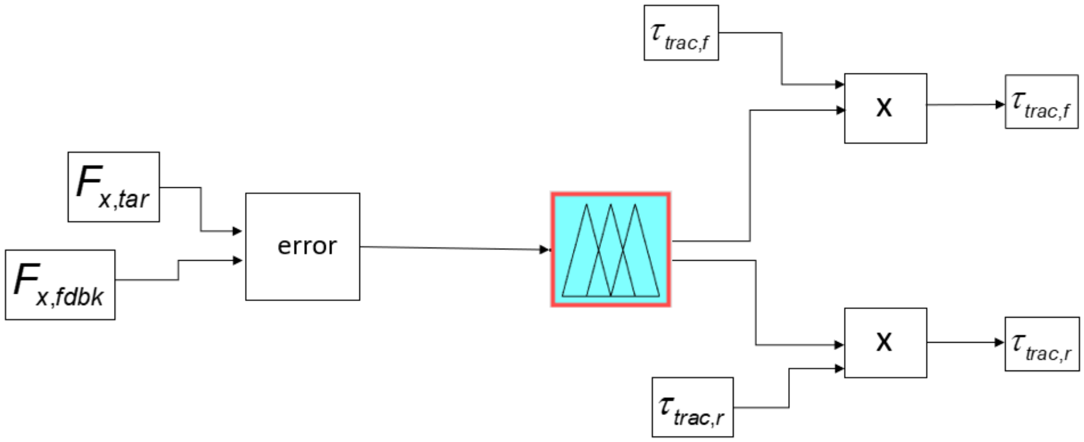

4.14 Fuzzy rule strategy for traction motor torque adjustment

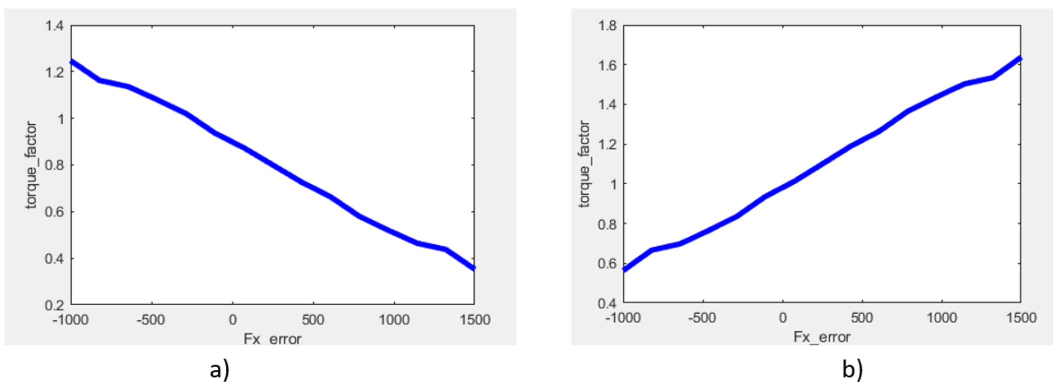

4.15 Fuzzy rule relationship between the Fx error and the traction motor torque adjustment factor. a) Torque factor calculation to decrease the traction motor torque.
b) Ttorque factor calculation to increase the traction motor torque.

The implementation of the fuzzy logic strategies for the motor torque adjustment will be demonstrated in section 4.8.1.

4.6 Motor Level Controller Design

At the motor level, the traction motor system is coupled with the vehicle model to represent the system to be controlled. This system is presented in (4.15) to (4.20). Equations (4.16) to (4.20) are modified versions of equations (2.1) through (2.8) to reflect that the torque vectoring motor is not active. These equations represent the system for one axle, with a right and left wheel. The system applies to both the front and rear axles.

$$\dot{V}_x = \frac{F_x}{m} \tag{4.15}$$

$$\dot{\omega}_{traction} = \frac{1}{J_{trac}}\left(\tau_{traction} - \frac{\rho}{(1+\rho)}(\tau_{HSL} + \tau_{HSR})\right) \tag{4.16}$$

$$\dot{\theta}_{HSL} = \frac{\rho}{(1+\rho)}\omega_{traction} - \omega_{WSL} \tag{4.17}$$

$$\dot{\theta}_{HSR} = \frac{\rho}{(1+\rho)}\omega_{traction} - \omega_{WSR} \tag{4.18}$$

$$\dot{\omega}_{WSL} = \frac{1}{J_w}\left(\tau_{HSL} - R_w F_{x,L}\right) \tag{4.19}$$

$$\dot{\omega}_{WSR} = \frac{1}{J_w}\left(\tau_{HSR} - R_w F_{x,R}\right) \tag{4.20}$$

Where $F_x = F_{x,L} + F_{x,R}$

and

$\tau_{HSL} = K\theta_{HSL} + b\dot{\theta}_{HSL}$

$\tau_{HSR} = K\theta_{HSR} + b\dot{\theta}_{HSR}$

The system is linearized around the operating point of driving in a straight line at 100 KPH, and then cast into the discrete state space form using the Euler method, (4.21), (4.22).

$$x_{k+1} = \bar{A}x_x + \bar{B}u_k \tag{4.21}$$

$$\hat{y}_{k+1} = Cx_{k+1} \tag{4.22}$$

Where

$x_k = \begin{bmatrix} V_{x,k} & \omega_{traction,k} & \theta_{hsL,k} & \theta_{hsR,k} & \omega_{wsL,k} & \omega_{wsR,k} \end{bmatrix}^T$

$u_k = \begin{bmatrix} \tau_{traction,k} \end{bmatrix}$

$y_k = \begin{bmatrix} F_{x,k} \end{bmatrix}$

Using (3.15) to solve for the control input yields (4.23).

$$u_k = ((C\bar{B})^T QC\bar{B} + R)^{-1}(C\bar{B})^T Q(y^*_{k+1} - C\bar{A}x_k) \tag{4.23}$$

Where $u_k = \tau_{traction,k}$.

The control input represents the traction motor torque that is required to meet the target traction force that is cascaded from the vehicle level controller. This controller strategy is used for both the front and rear traction motors.

To ensure system stability, Q and R must be selected such that the inverse term in (4.23) is never zero, (4.24).

$$(C\bar{B})^T QC\bar{B} + R \neq 0 \tag{4.24}$$

The weights for Q and R are selected to balance response time and the control input magnitude. For the controllers used here, it was noted that setting R to a non zero value caused the controller performance to deteriorate significantly. That is because when R is not 0, the control signal magnitude is limited. Setting R to 0 allowed the signal to move enough to apply an appropriate level on control to the plant. When R is set to 0, Q does not have an affect on the control signal.

4.7 Estimating System Parameters

4.7.1 Estimating Traction Force

For longitudinal vehicle motion, the traction force is the reference, and also the feedback from the system. Hence it is critical to have an accurate value of this parameter for successful control of the eAWD powertrain system. Unfortunately, sensors are not available to measure the traction force in real time. In this thesis, a Controller Output Observer (COO) based on a WOSA controller is used to estimate the traction force. The advantage of the COO is that it uses measurements that are already available to estimate the traction forces. A diagram of the COO strategy is presented in Figure 4.16.

The COO uses a WOSA controller to minimize the error between the measured wheel speeds from the vehicle (which are treated as the reference) and wheel speeds calculated from an estimation model of the vehicle system. The half shaft torques are treated as an exogenous input into the system. The estimation model is the vehicle model combined with the eAWD model as described in section 4.5, equations (4.15) to (4.20). The system parameters are presented in (4.25) to (4.27).

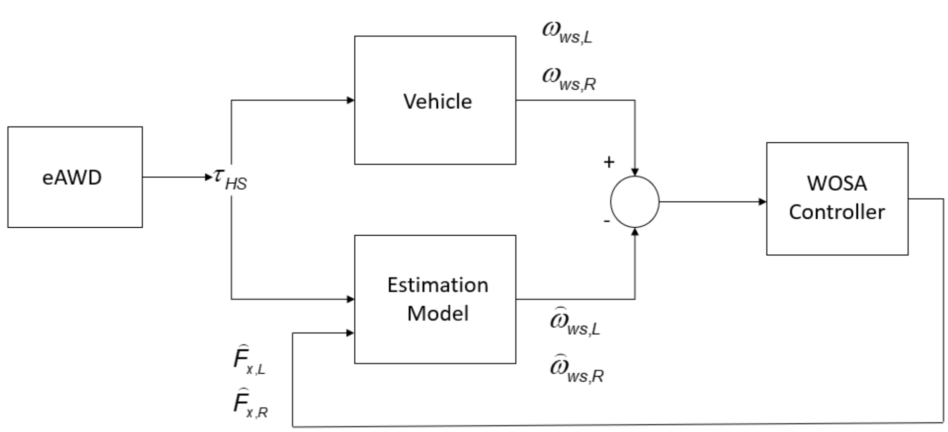

Figure 4.16 COO For Estimating F_x

$$x_k = \begin{bmatrix} V_{x,k} & \omega_{traction,k} & \theta_{hsL,k} & \theta_{hsR,k} & \omega_{wsL,k} & \omega_{wsR,k} \end{bmatrix}^T \tag{4.25}$$

$$u_k = \begin{bmatrix} \hat{F}_{x,L,k} & \hat{F}_{x,R,k} \end{bmatrix}^T \tag{4.26}$$

$$y_k = \begin{bmatrix} \omega_{ws,L,k} & \omega_{ws,R,k} \end{bmatrix}^T \tag{4.27}$$

Following a process similar to that described in section 4.6, the WOSA control law is presented in (4.28).

$$u_k = ((C\bar{B})^T QC\bar{B} + R)^{-1}(C\bar{B})^T Q(y^*_{k+1} - C\bar{A}x_k) \tag{4.28}$$

Where $u_k = \begin{bmatrix} \hat{F}_{x,L,k} & \hat{F}_{x,R,k} \end{bmatrix}^T$.

Figure 4.17 shows that the estimate tracks the feedback F_x signal from CarSim fairly closely.

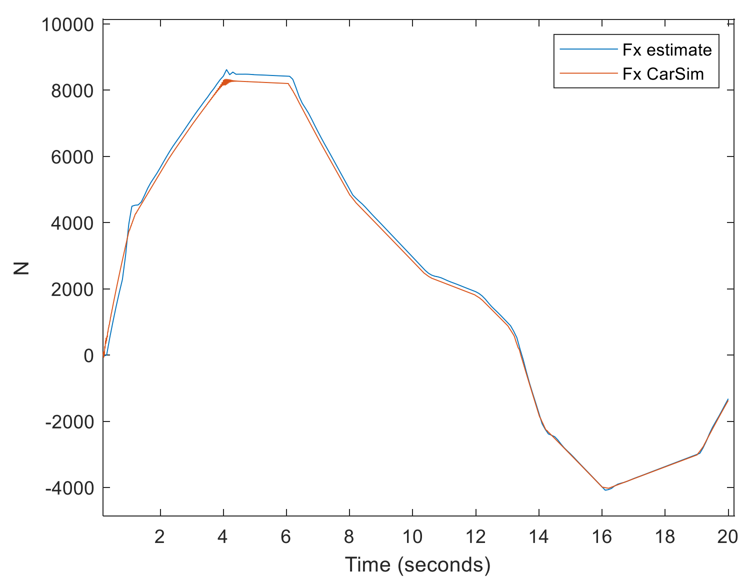

Figure 4.17 Traction force estimate vs. CarSim

4.7.2 Estimating Longitudinal Vehicle Speed

The vehicle speed is a key component of the vehicle level control strategy. Typically, the vehicle speed is estimated by using the non driven wheel speeds. Because all four wheels are driven in the eAWD, that approach is not practical. In this thesis, a COO is used to estimate the longitudinal vehicle speed.

The COO uses the longitudinal acceleration which is readily available from vehicle sensor data as a reference. A WOSA controller is used to calculate the control input traction force which minimizes the error between the measured longitudinal acceleration and the feedback longitudinal acceleration that is calculated in an estimation model that represents the vehicle's longitudinal dynamics. The estimated acceleration is integrated to provide an estimate of the longitudinal speed. See Figure 4.18 for a diagram of this strategy.

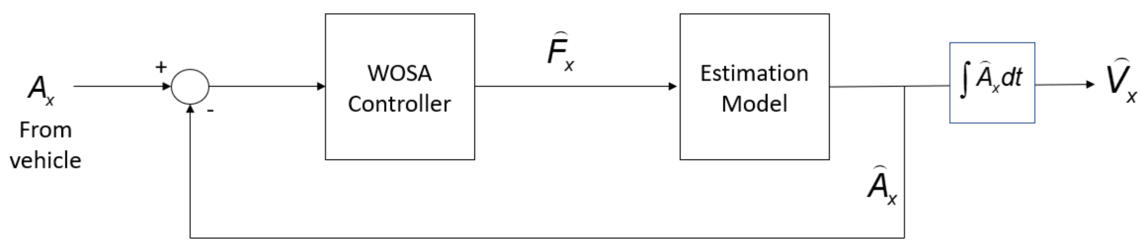

Figure 4.18 Conceptual Diagram of COO for estimating V_x

The estimation model is based on (4.15). The control model for the COO is based on the system equations (4.11) and (4.12). However, the system output is (4.29).

$$y_k = A_{x,k} \tag{4.29}$$

Applying (3.15), the control input is presented in (4.30).

$$u_k = (Q(D^T D + R)^{-1})(D^T Q)(y^*_{k+1}) \tag{4.30}$$

Where $u_k = \hat{F}_{x,k}$.

The estimate of V_x compared to the output from CarSim is shown in Figure 4.19. This particular approach has two advantages. First, the only input that is needed is a sensor reading for the longitudinal acceleration which is readily available. Second, this controller generates an estimate of the longitudinal traction force, Figure 4.20.

For the vehicle level control strategy, the estimate of F_x that is presented section 4.7.1 will be used because it is more accurate. However, it is interesting that this parameter estimation strategy can be used to estimate two system parameters with a single sensor input.

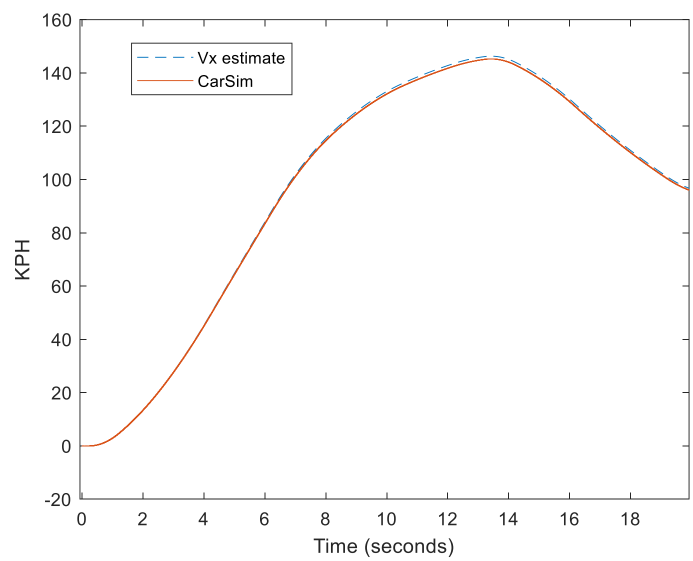

Figure 4.19 Estimate of V_x vs CarSim

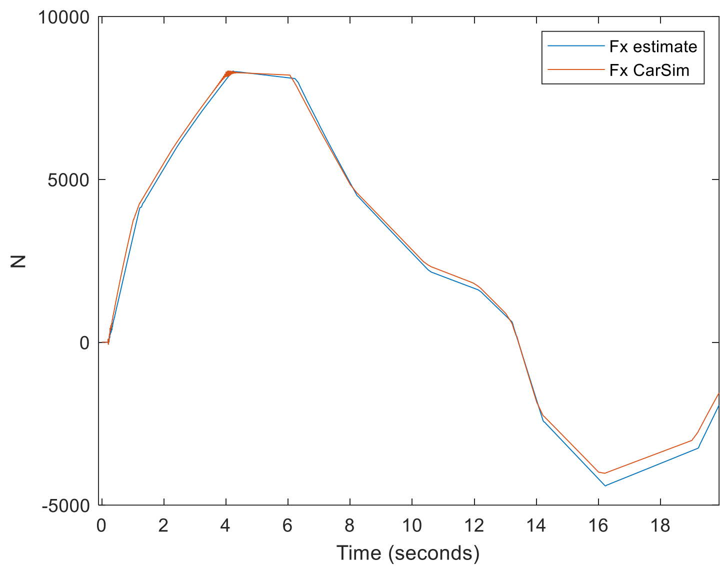

Figure 4.20 Estimate of Fx from COO estimate of Vx

4.8 Simulation Results

The overall vehicle and motor control framework (Figure 4.10) was simulated for several control cases using the Simulink/CarSim combination as described in section 2.4.

4.8.1 Launch on High Friction Surface

In this control case, the vehicle is launched on a high friction coefficient road surface with $\mu = 1$. The accelerator pedal is applied at various positions to generate the reference traction force. The result is presented in Figure 4.21 and shows that the actual traction force does not track the reference traction force closely.

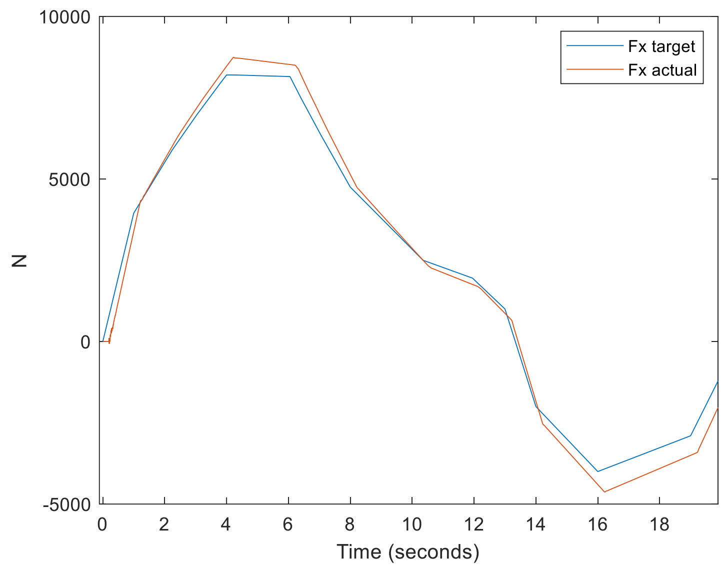

Figure 4.21 Traction force tracking without fuzzy rules

To improve the tracking performance of the vehicle level controller, an on-line fuzzy rule set is employed to adjust the traction motor torques to reduce the error between the traction force target and the feedback traction force. The details of the implementation of the fuzzy rule set is discussed in section 4.5. A significant improvement in tracking performance using the fuzzy rule set is achieved and is shown in Figure 4.22. The traction torque request and adjusted traction torque request for the front axle are presented in Figure 4.23. A very similar result occurs for the rear axle.

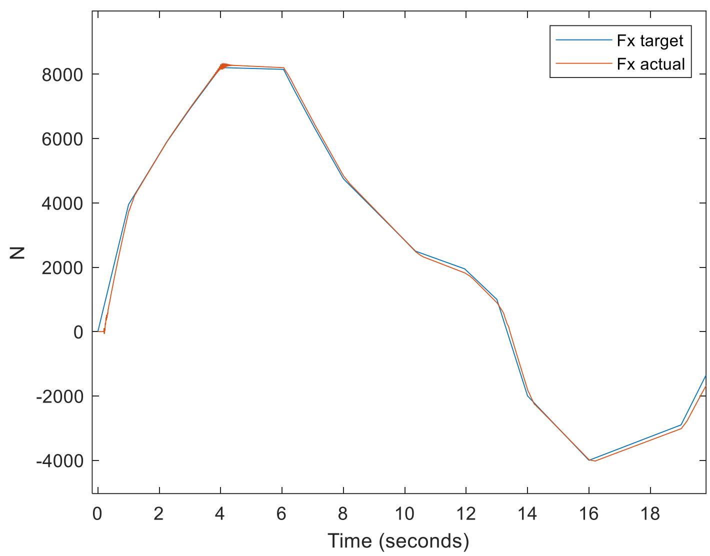

Figure 4.22 Traction force tracking with fuzzy rules

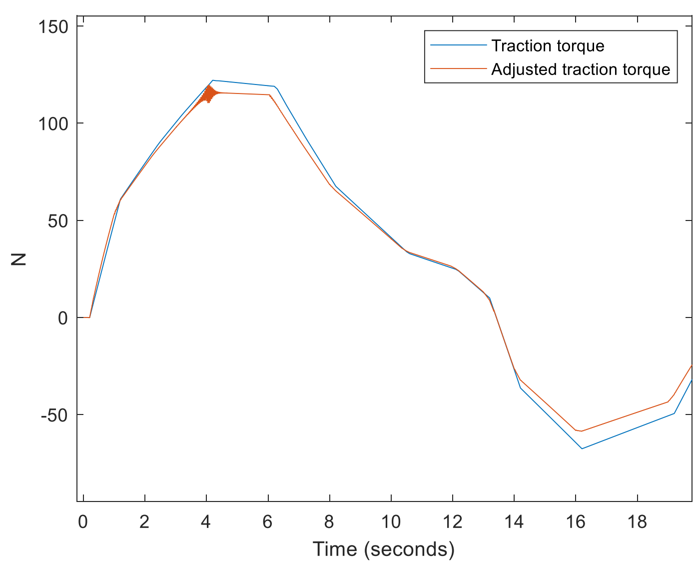

Figure 4.23 Front axle traction torque and adjusted traction torque

The traction torque adjustment factor plot is presented in Figure 4.24. The torque factor can range in value between 0.7 and 1.5. The factor decreases when the traction force feedback is higher than the traction force reference. The factor increases when the traction force feedback is below the reference.

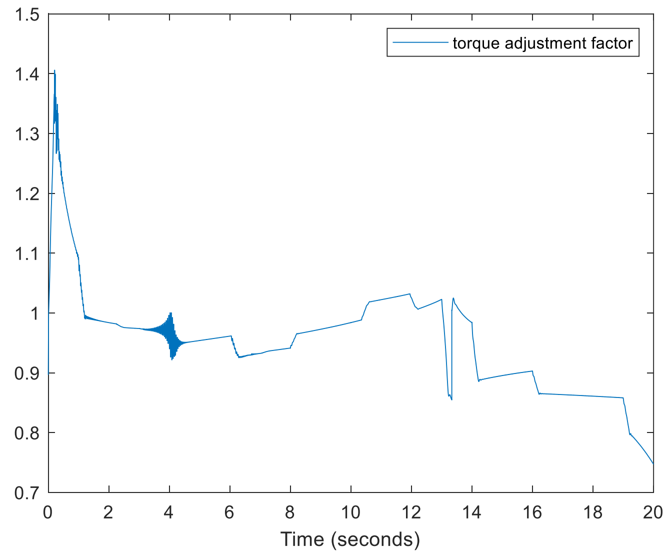

4.24 Traction torque adjustment factor

<u>4.8.1.1 Front/Rear Traction Force Split</u>

The front and rear traction force split strategy is discussed in detail in section 4.4. To reiterate, a fuzzy rule set is used to adjust the traction force split between the front and rear axles based on the vehicle acceleration. The split represents the traction force target for the front and rear axles respectively. Figure 4.25 shows the results for the high friction launch control case. When the vehicle is launching, weight is shifted to the rear of the vehicle. Hence, the traction force target for the rear axle is higher than for the front axle. As the vehicle slows down, weight shifts to the front of the vehicle and the traction force target for the front axle is higher than for rear axle.

The traction force torque request split is presented in Figure 4.26. These torque values are the adjusted torques as discussed in the previous section. The longitudinal acceleration is shown in Figure 4.27. Comparing this graph with the traction force split, a clear correlation can be seen.

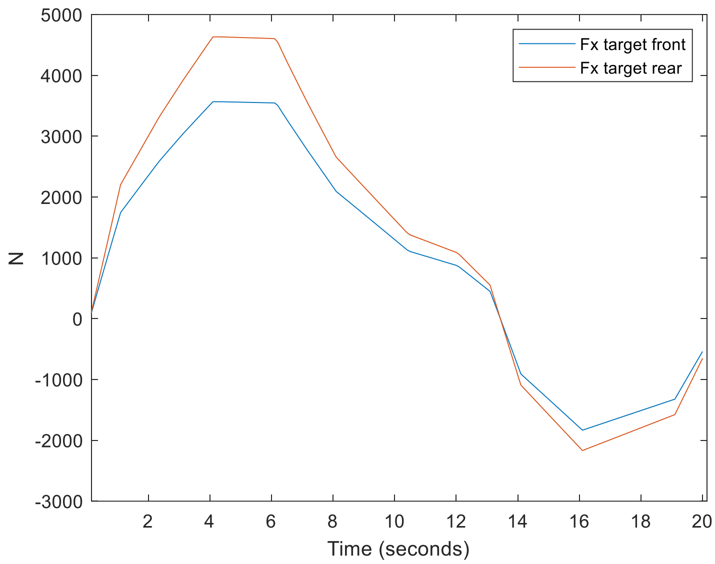

Figure 4.25 Traction force target front/rear

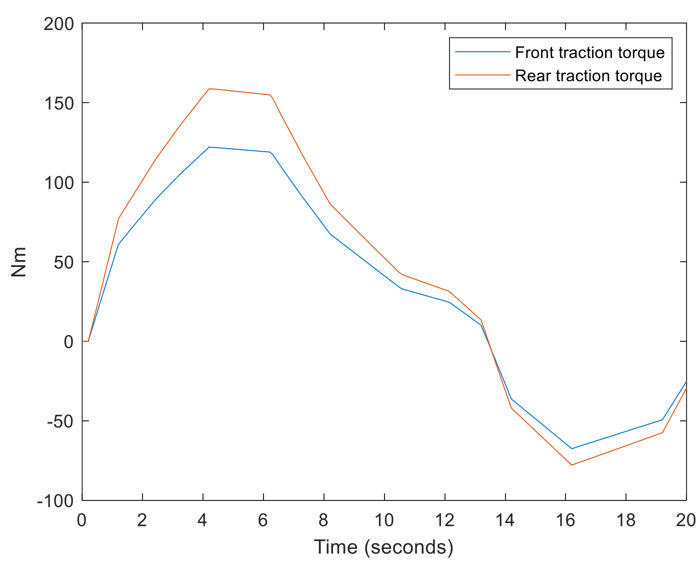

Figure 4.26 The traction force torque split from front to rear

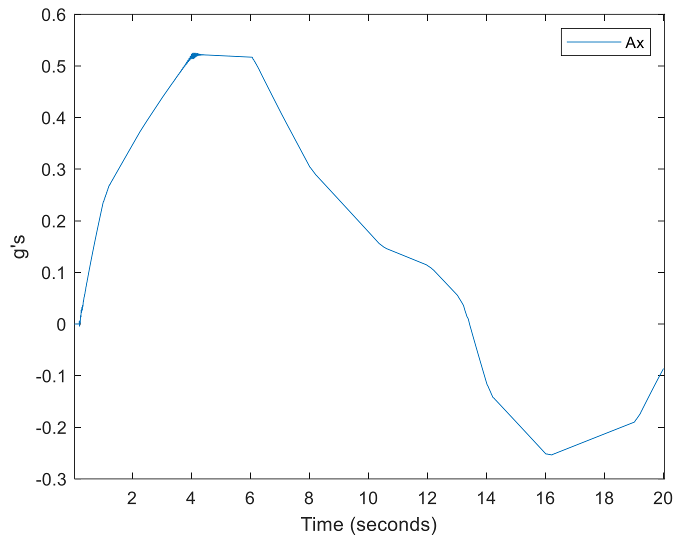

4.27 Longitudinal acceleration

4.8.2 Launch on Low Friction Surface

This control situation involves launching the vehicle on a low friction road surface. In this case, $\mu = 0.3$ which represents icy conditions. The total approximate available traction force is the vehicle mass times the coefficient of friction which is $13{,}453N \times 0.3 = 4036N$. The simulation results are presented in Figure 4.28. The actual traction force reaches a value of about 4000 N, even though the requested traction force from the driver is around 8000 N.

Because the road surface is slippery, the tires on the front and rear axles experience a very high slip ratio. To improve the performance of the vehicle on the low friction surface and reduce the slip ratio, a supplemental fuzzy rule controller is used to adjust the motor torque commands to reduce the amount of wheel slip.

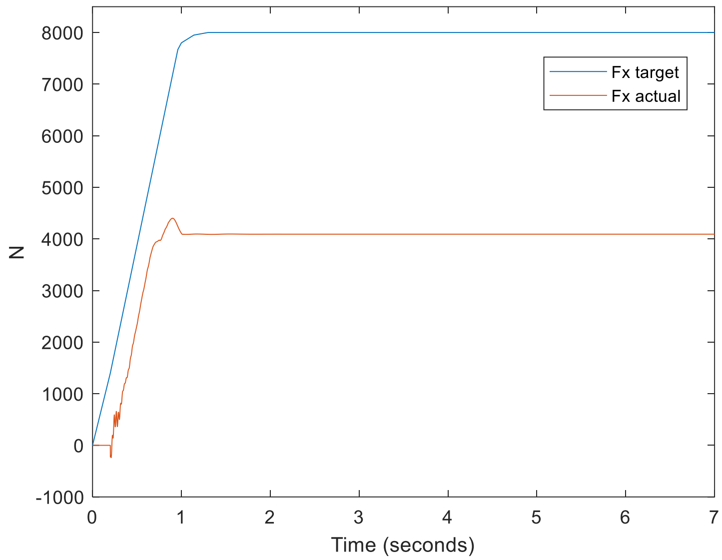

Figure 4.28 Low friction launch simulation

The fuzzy rules calculate a torque adjustment factor based on the amount of error between the target wheel slip of 0.2 and the actual measured wheel slip. This adjustment factor reduces the traction motor torque to significantly reduce the wheel slip. The fuzzy logic strategy is shown in Figure 4.29. The torque adjustment factor values are shown in Figure 4.30 a) and b).

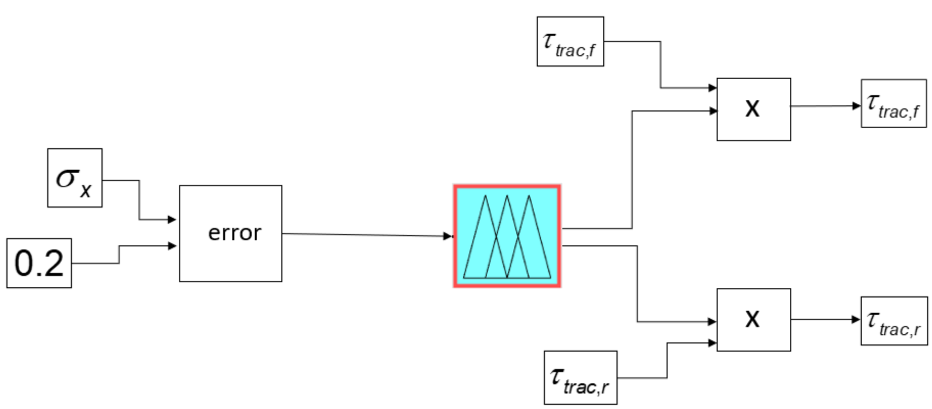

Figure 4.29 Fuzzy logic strategy to adjust traction motor torque to reduce wheel slip

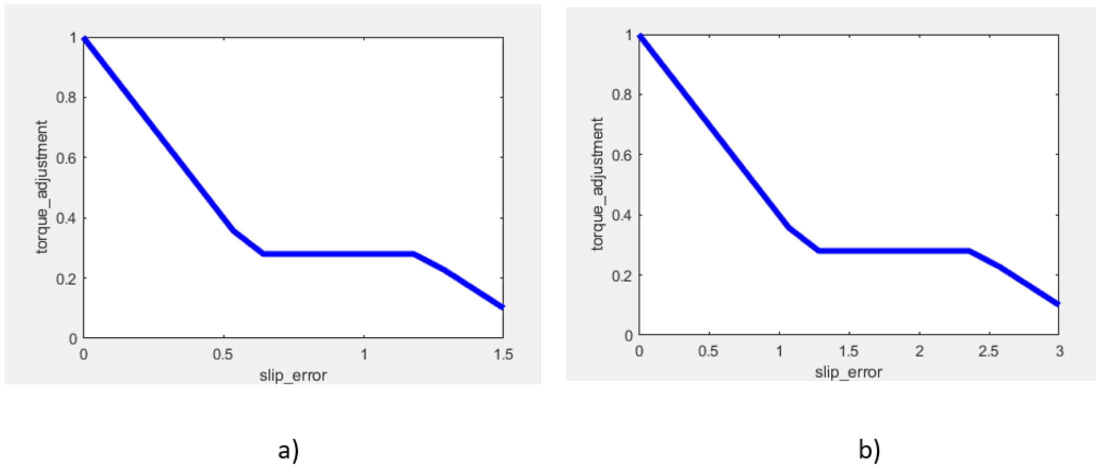

Figure 4.30 Relationship between slip error and the torque adjustment factor.
a) Front tire slip, b) rear tire slip

The wheel slip with and without the controller intervention are shown in Figure 4.31. The graph shows the wheel slips for the left tire on each axle, but the result for the right tire is very similar. The wheel slips without the controller reach a very high level, which puts the tire into the unstable range. When the controller is active, the wheel slips are significantly reduced, keeping the tires much closer to the linear range. In Figure 4.31 a), the peak wheel slip reached for the front tire is 2.5, and for the rear tire it's 5. In Figure 4.31 b), the peak wheel slip reached for the front tire is 0.49, and for the rear tire it's 1.07.

During the low friction launch, the vehicle speed reaches around 50 KPH shown in Figure 4.32, and the longitudinal acceleration reaches around 0.25 g's shown in Figure 4.33. These results were not changed by the intervention of the fuzzy logic controller to adjust the motor torque requests to reduce wheel slip.

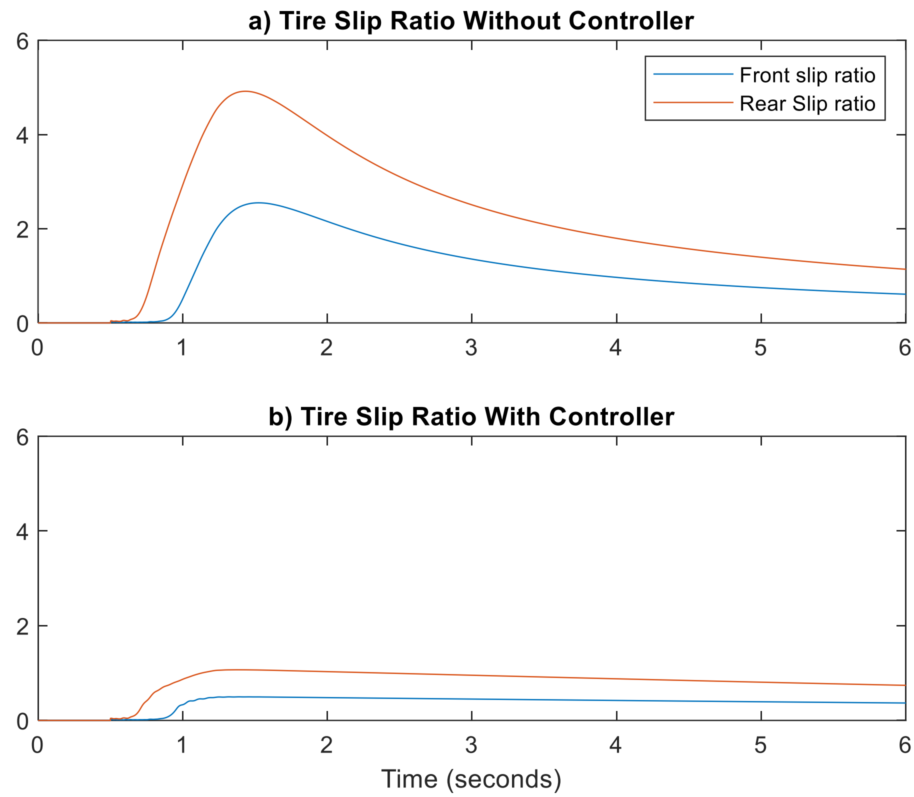

Figure 4.31 Wheel slip for front left and rear left tires

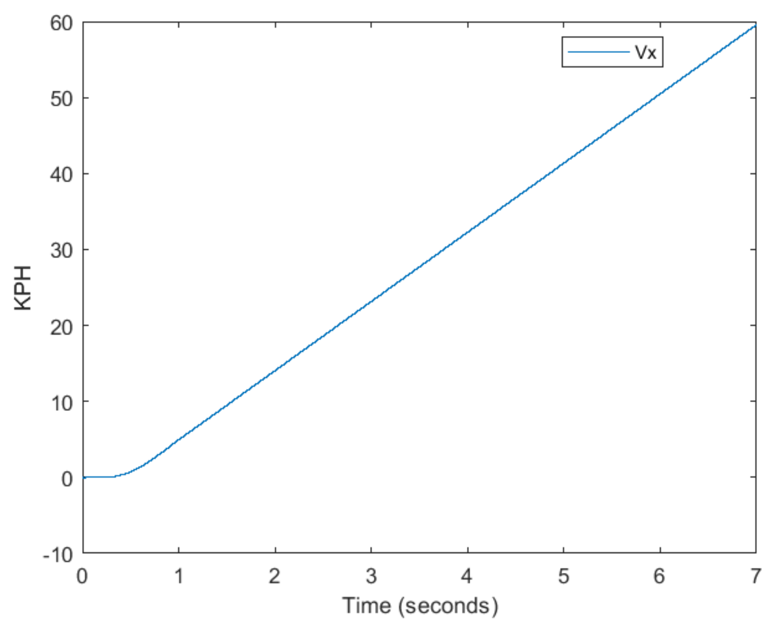

4.32 Vehicle speed during low friction launch

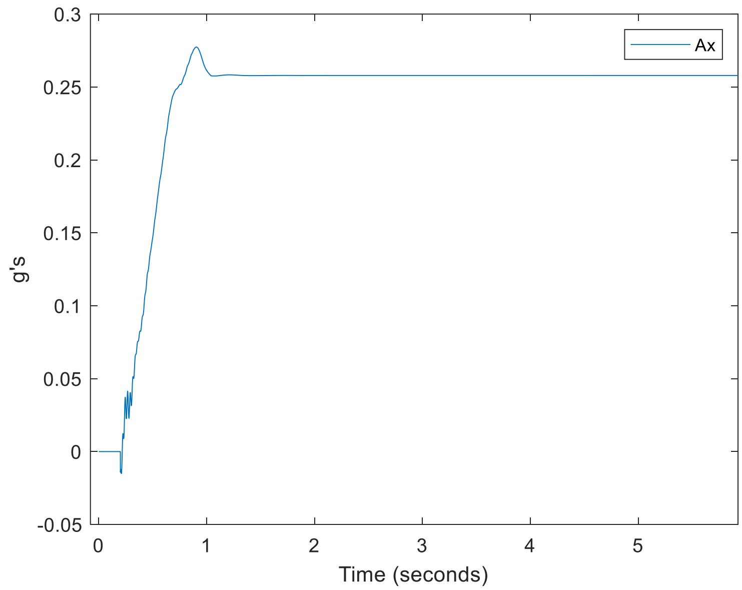

4.33 Longitudinal acceleration during low friction launch

CHAPTER FIVE

LATERAL MOTION CONTROL

5.1 Introduction

This chapter considers two key driving scenarios for controlling the lateral motion of the vehicle: A high speed double lane change on a high friction road surface, and a high speed double lane change on a low friction road surface. These two driving scenarios require using the torque vectoring motors to distribute torque to the left or right side of the vehicle to maintain stability and prevent the vehicle from sliding out of control. Lateral motion control involves controlling the yaw rate of the vehicle.

5.1.1 Literature review for yaw control and torque vectoring

Many researchers have used fuzzy rules to control the yaw rate of a vehicle during the double lane change maneuver. These references are discussed in section 1.3. Other yaw control approaches are discussed below.

Reference [33] uses an electric motor at each of the front wheels. The yaw moment control input is calculated using estimates of tire stiffness and side slip angle. A weighted least squares strategy is used to allocate the torque between the right and left wheels. This work did not include four wheel control in its scope, and it did not include low friction yaw control. It's focus was on improving driving performance on high friction surfaces.

In [34], [35],[36],[37],[38], torque vectoring is specifically discussed. In [34], a thorough introduction and explanation of the torque vectoring concepts is presented. Torque vectoring can be accomplished in many ways. In the references mentioned, there is typically an electric motor at each wheel hub, and the motors can be controlled independently. The advantage of using four motors is that torque vectoring can be achieved by commanding different torque levels at each wheel on the same axle. The disadvantage of using four motors is the extra cost and weight.

In this thesis, a motor assembly is used on each axle. Each motor assembly consists of a traction motor and torque vectoring motor. This configuration offers most of the benefits of four in-wheel motors with less cost and weight. A detailed discussion of this electric motor configuration is presented in Chapter 2.

5.1.2 Outline Of the Rest Of the Chapter

In this chapter important concepts of lateral vehicle motion are presented. First, lateral tire dynamics are discussed including tire side slip and lateral tire forces. Then key measures of vehicle performance are discussed such as yaw rate, yaw moment, and side slip angle. Then estimation of key vehicle parameters using a COO observer is discussed. Then the WOSA controller and integrated fuzzy logic rules to control the vehicle for a high speed double lane change on a high friction and low friction road surface are presented. Finally, simulation results are presented.

5.2 Lateral Tire Dynamics

When the vehicle is turning, going around a bend or performing any maneuver that is not straight ahead driving, lateral dynamics come into play. The well known bicycle model representing the lateral movement of a vehicle [39] is presented in Figure 5.1 and is employed in the development of the lateral motion vehicle controller.

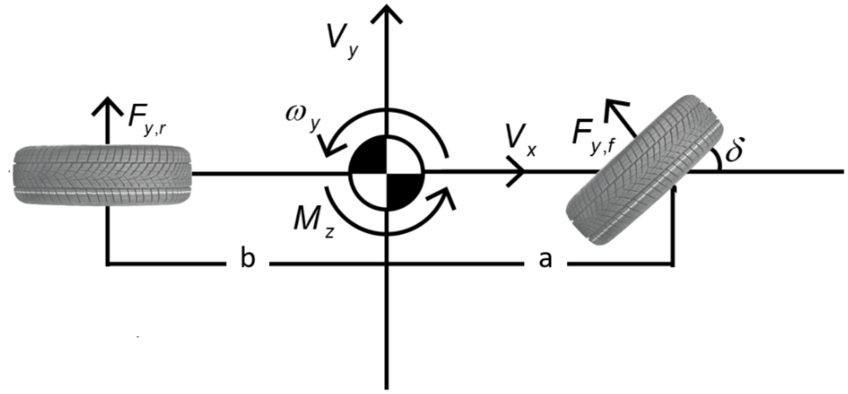

Figure 5.1 Vehicle Bicycle Model for Lateral Motion

In the model, the yaw rate is defined as ω_y, the yaw moment is defined as M_z, *a* and *b* are the distances from the front axle and rear axle to the center of gravity (C.G.) respectively. The lateral tire forces are $F_{y,f}$ and $F_{y,r}$ which are discussed in more detail below. The front wheel steering angle δ is based on the steering wheel input from the driver. The steering input is converted into a yaw rate reference that is used as the reference for the controller. The yaw rate reference is discussed in section 5.3.1. The vehicle mass is *m*. The yaw moment of inertia is J_y. This model does not consider the pitch or roll angles of the vehicle during lateral motion.

The dynamic equations for this model are presented in (5.1) and (5.2). Note, this model assumes a small front steering angle.

$$\dot{V}_y = \frac{1}{m}\left(F_{y,f} + F_{y,r}\right) - V_x\omega_y \tag{5.1}$$

$$\dot{\omega}_y = \frac{1}{J_y}(aF_{y,f} - bF_{y,r} + M_z) \tag{5.2}$$

The lateral tire forces are represented in (5.3) and (5.4).

$$F_{y,f} = C_{\alpha,f}\alpha_f \tag{5.3}$$

$$F_{y,r} = C_{\alpha,r}\alpha_r \tag{5.4}$$

Where the tire slip angles are defined in (5.5) and (5.6).

$$\alpha_f = \left(\delta - \frac{V_y + a\omega_y}{V_x}\right) \tag{5.5}$$

$$\alpha_r = \left(-\frac{V_y - b\omega_y}{V_x}\right) \tag{5.6}$$

In these equations, C_α is the cornering stiffness coefficient which represents the slope of the linear portion of the lateral tire model, shown in Figure 5.2. The slip angle of the tire is the angle between the direction the tire is pointed and the direction the tire is travelling, shown in Figure 5.3. The lateral tire force represents the reaction force of the tire to the road surface as the vehicle is turning. This force is required to keep the vehicle in contact with the road and in the turning trajectory.

5.3 Yaw Rate and Yaw Moment

When a vehicle is turning, a yaw angle and yaw moment are generated. The yaw angle is the angle at which the vehicle rotates around it's center axis. The yaw angle can also be thought of as the angle between the vehicle's x-axis and the direction the vehicle is pointed. The yaw rate is the time derivative of the yaw angle. Sometimes the yaw rate

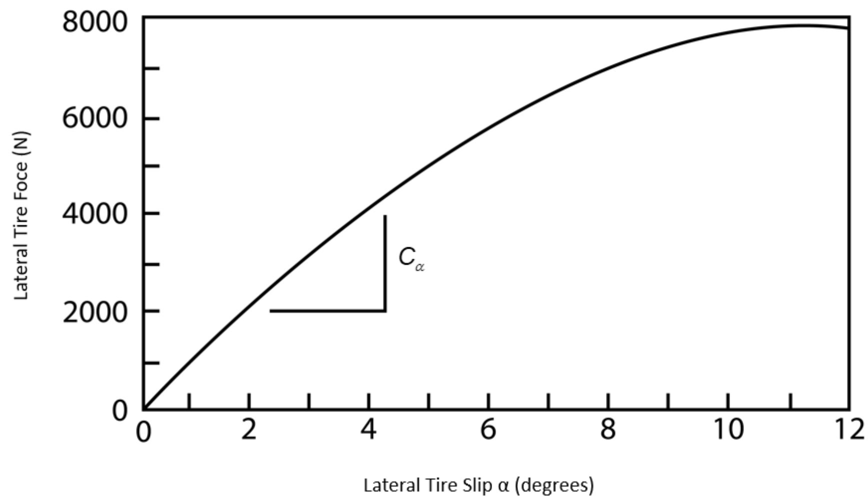

Figure 5.2 Typical Lateral tire force vs slip angle curve

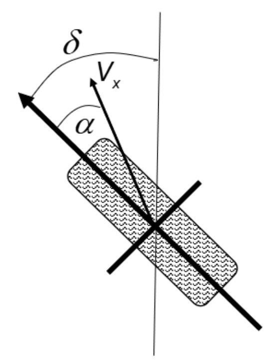

Figure 5.3 Tire slip angle

is called the yaw velocity. The yaw rate is direcly related to the steering wheel input from the driver.

The yaw moment is the moment generated by the lateral tire forces around the center of gravity of the vehicle. The yaw moment will be the control input for the vehicle system controller. See Figure 5.4 for an illusration of these concepts.

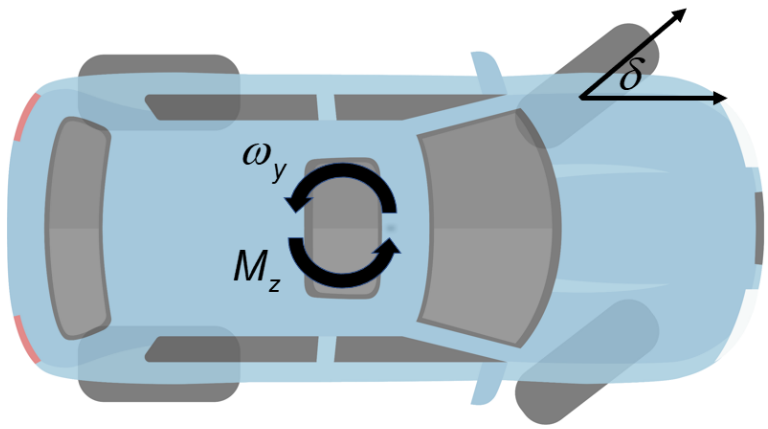

Figure 5.4 Diagram showing concept of yaw rate and yaw moment

5.3.1 Yaw Rate Reference

For lateral motion control, it is necessary to generate a yaw reference for the controller to track. In order to explain how the yaw reference is generated, it is necessary to discuss oversteer, understeer, and neutral steer.

Oversteer occurs when a vehicle is negotiating a turn, and the vehicle turns more than the driver is commanding through the steering wheel. The driver experiences oversteer as the rear of the vehicle sliding out of control. Understeer occurs when a vehicle is negotiating a turn and the vehicle does not respond to the driver's steering input. The driver experiences understeer as the vehicle plowing straight ahead even though the steering wheel is turned.

An intuitive way to understand oversteer and understeer is to consider the bicycle model presented in Figure 5.1. If the vehicle is traveling around a circle with a constant radius and steering angle, the vehicle is in a neutral steer condition if the tire slip angles for the front and rear tires are equal ($\alpha_f = \alpha_r$). The vehicle is in an oversteer condition if the front slip angle is less than the rear slip angle ($\alpha_f < \alpha_r$). The vehicle is in an understeer condition if the front slip angle is greater than the rear slip angle ($\alpha_f > \alpha_r$).

When the vehicle is driving on a constant radius circle, the amount of steering input has to change based on the vehicle speed. If the longitudinal velocity is increased (and also the lateral acceleration), then the front wheel steering angle will need to increase to maintaing the radius. If the longitudinal velocity is decreased (and also the lateral acceleration), less steering angle is needed to maintain the radius.

The steering gradient is defined as the derivative of the front steering angle with respect to the lateral acceleration. If the gradient is positive, then the vehicle is in an understeer condition If the gradient is negative, the vehicle is in an oversteer condition. See Figure 5.5 for an illustration. The gradient itself is called the understeer gradient (K_{us}). The understeer gradient is presented in (5.7) [40].

$$K_{us} = \frac{m}{(a+b)}\left(\frac{b}{C_{\alpha,f}} - \frac{a}{C_{\alpha,r}}\right) \tag{5.7}$$

The yaw rate reference formula (5.8) is derived from the bicycle model and uses K_{us} as an input. Note that the yaw reference also uses the front steering angle and longitudinal speeds as inputs.

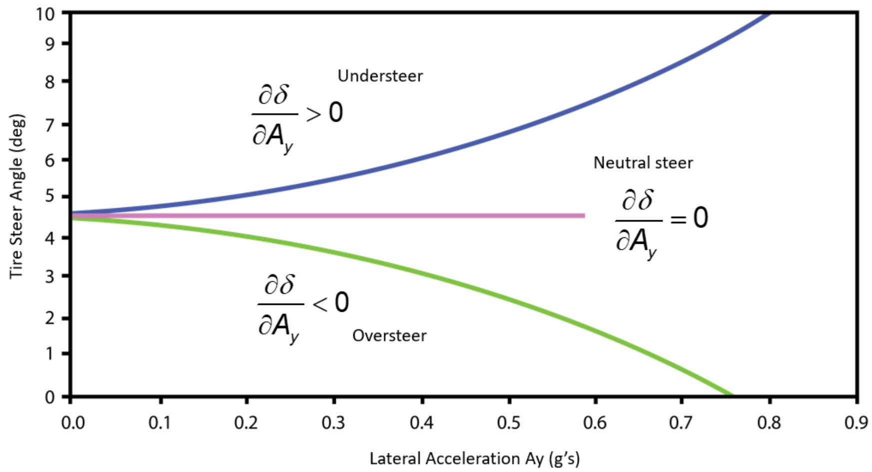

Figure 5.5 Graphical definition of the understeer gradient [40]

$$\omega_{y,ref} = \frac{V_x \tan(\delta)}{(a + b + K_{us} V_x^2)} \tag{5.8}$$

<u>5.3.2 Limiting Yaw Rate Reference for Low Friction Surface</u>

When the vehicle is experiencing lateral motion on a low friction road surface, there is the risk of tire saturation and the vehicle sliding out of control. Figure 5.6 shows a typical tire lateral slip angle versus slip curve. When the tire force reaches beyond the linear range of the curve, the tire becomes saturated and the vehicle can become unstable. To prevent tire saturation, it is necessary to limit the yaw rate reference for the vehicle level controller.

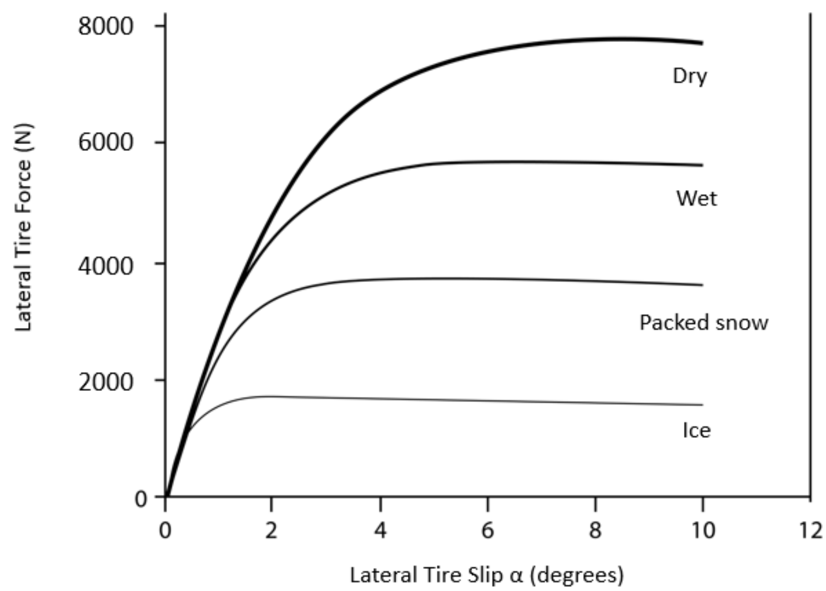

Figure 5.6 Typical friction curves vs tire side slip angle

Consider a vehicle traveling around a constant radius curve at a constant speed as shown in Figure 5.7. The vehicle experiences a steady state yaw rate, $\dot{\omega}_y$ as shown in the diagram. If the actual yaw rate exceeds the steady state yaw rate, the vehicle is likely to experience oversteer and excessive side slip. Hence, during a lateral maneuver on a low friction road surface, the reference yaw rate should not exceed the steady state yaw rate as described in (5.9). This steady state yaw rate will be called the limited yaw rate. This value of the yaw rate is used for the high speed double lane change maneuver performed on a low friction surface that is discussed in section 5.7.2.

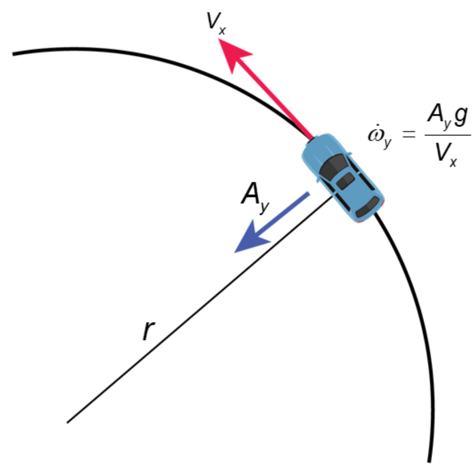

Figure 5.7 Vehicle travelling on a constant radius curve at constant speed

$$\dot{\omega}_{y,\mathrm{lim}} = \frac{A_y g}{V_x} \tag{5.9}$$

5.3.3 Side Slip Angle

Vehicle side slip angle is defined as the angle between the longitudinal and lateral velocity vectors (5.10). This angle can be thought of as the difference between the direction the vehicle is pointed (V_x) and the direction the vehicle is moving (V_y). The vehicle occupant will experience side slip angle as the vehicle sliding sideways.

$$\beta = \tan^{-1}\left(\frac{V_y}{V_x}\right) \tag{5.10}$$

For lateral motion control, it is important to limit the side slip angle for vehicle stability and driving comfort. In this thesis, the controller does not actively limit the side slip angle. However, the side slip angle is indirectly controlled, and is used as a measure of the effectiveness of the controller to maintain vehicle stability during the double lane change maneuver discussed in section 5.7.

5.4 Development of the Lateral Motion Controller

The vehicle level controller calculates a control yaw moment that tracks the yaw rate reference signal. The control yaw moment is converted into a target tire force for the torque vectoring motors, F_{TV}. The conversion of the control yaw moment into the target tire forces is done using a fuzzy logic rule set. In typical control strategies for lateral vehicle motion, the vehicle model is linearized for controller design by assuming a constant longitudinal vehicle speed. In this thesis, the vehicle speed is not assumed to be constant, and a nonlinear vehicle model is used.

The motor controller takes the target F_{TV} and calculates a torque request for the torque vectoring motors. The torque vectoring motors apply a yaw moment that attempts to match the control yaw moment calculated at the vehicle level. The eAWD system then calculates halfshaft torques that are fed into the CarSim vehicle model. This framework is shown in Figure 5.8.

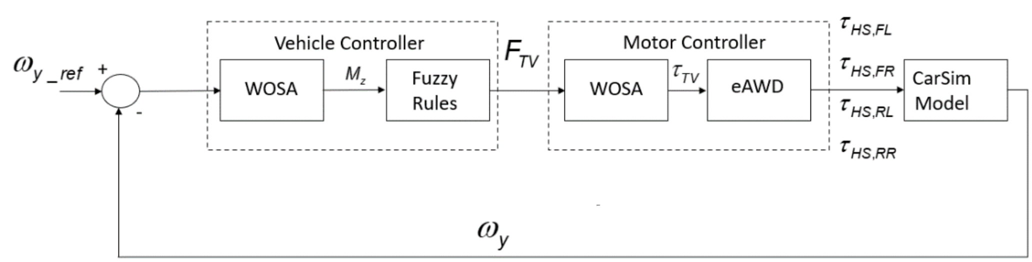

Figure 5.8 Diagram of Control Strategy for Lateral Vehicle Motion

5.4.1 The Vehicle Level Controller

The vehicle level controller is developed using the bicycle model in Figure 5.1, presented again in Figure 5.9.

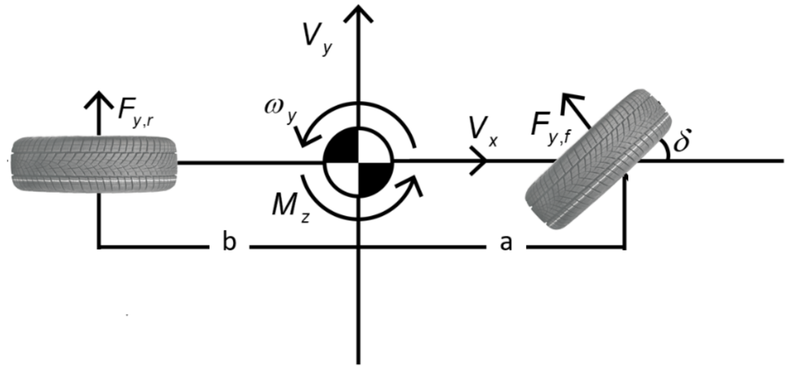

Figure 5.9 Bicycle model for lateral motion controller

Combining equations (5.1) to (5.6), a nonlinear vehicle system is presented in equations (5.11) and (5.12)

$$\dot{x}(t) = f(x(t)) + Bu(t) + B_\delta \delta(t) \tag{5.11}$$

$$y(t) = Cx(t) \tag{5.12}$$

The parameters of the model are presented in equations (5.13) to (5.18).

$$f(x) = \begin{bmatrix} \dfrac{-2.569}{V_x} & \dfrac{0.2263}{V_x} - V_x \\ \dfrac{0.0826}{V_x} & \dfrac{-1.814}{V_x} \end{bmatrix} \tag{5.13}$$

$$B = \begin{bmatrix} 0 \\ 1 \end{bmatrix} \tag{5.14}$$

$$B_\delta = \begin{bmatrix} 1.284 \\ 0.6094 \end{bmatrix} \tag{5.15}$$

$$C = \begin{bmatrix} 0 & 1 \end{bmatrix} \tag{5.16}$$

$$x = \begin{bmatrix} V_y & \omega_y \end{bmatrix}^T \tag{5.17}$$

$$u = \left[M_z \right] \tag{5.18}$$

In this model, δ is the steering angle of the front wheel, and it is based on the steering wheel input from the driver. The controller has no authority over δ, so it is treated as an exogenuous input.

Modifying equations (3.18) and (3.19), the discrete vehicle system is presented in (5.19) and (5.20).

$$x_{k+1} = x_k + t_s \left(f(x_k) + Bu_k + B_\delta \delta_k \right) \tag{5.19}$$

$$y_k = Cx_k \tag{5.20}$$

Following a development process similar to that presented in equations (3.25) to (3.27), the control input for the WOSA controller is presented in (5.21).

$$u_k = (t_s^2 (B^T C^T QCB) + R)^{-1} t_s B^T C^T Q(y_{k+1}^* - Cx_k - t_s C(f(x_k) + B_\delta \delta_k)) \tag{5.21}$$

Where $u_k = M_{z,k}$.

For the system to be stable, it is necessary to show that u_k is bounded. If the input is bounded, then the output will automatically be bounded. For this system, the output is given in (5.22).

$$\hat{y}_{k+1} = \omega_{y,k} = C(x_k + t_s(f(x_k) + Bu_k + B_\delta \delta_k)) \tag{5.22}$$

The input is bounded by ensuring that (5.22) which is the inverse term from (5.21) is never zero by setting the weighting values of Q and R appropriately.

$$t_s^2 (B^T C^T QCB) + R \neq 0 \tag{5.23}$$

Setting the values for Q and R is discussed in section 4.5.

5.4.2 Motor Controller Design

The bicycle model is coupled with the torque vectoring motor equations to represent the plant to be controlled for the torque vectoring motor system. The bicycle model for the motor controller is presented in Figure 5.10. Note that this model shows that the traction motor tire force, F_{TV} along with the lateral tire forces, $F_{y,f}$ and $F_{y,r}$ generate a yaw moment at the vehicle C.G. In the model, T is the trackwidth of the vehicle and *a* and *b* are the distances from the front and rear axles respectively.

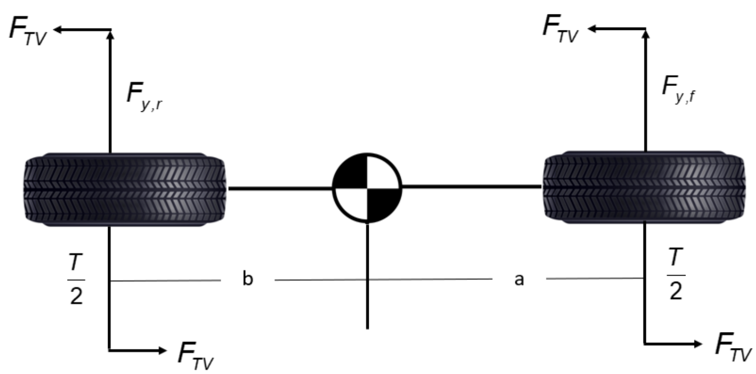

Figure 5.10 Bicycle model for torque vector motor controller

The plant model for control is presented in (5.24) to (5.32). This model is for the front axle only. The torque vectoring motor equations, (5.26) to (5.32), are the eAWD equations (2.13) to (2.18) modified to reflect the fact that only the torque vectoring motor is being used. Also, the vehicle model, (5.24) and (5.25), represents the front axle. The plant model for the rear axle is very similar and will be discussed later.

$$\dot{V}_y = \frac{F_{y,f}}{m} - V_x \omega_y \tag{5.24}$$

$$\dot{\omega}_y = \frac{1}{J_y}\left(aF_{y,f} + \frac{T}{2}F_{TV} \right) \tag{5.25}$$

$$\dot{\omega}_{TV} = \frac{1}{J_{TV}}\left(\tau_{TV} - \frac{1}{g_1 g_2 (1+\rho)}(\tau_{HSL} - \tau_{HSR}) \right) \tag{5.26}$$

$$\dot{\theta}_{HSL} = -\frac{1}{g_1 g_2 (1+\rho)}\omega_{TV} - \omega_{wL} \tag{5.27}$$

$$\dot{\theta}_{HSR} = \frac{1}{g_1 g_2 (1+\rho)}\omega_{TV} - \omega_{wR} \tag{5.28}$$

$$\dot{\omega}_{WSL} = \frac{1}{J_w}\left(\tau_{HSL} - R_w F_{x,L} \right) \tag{5.29}$$

$$\dot{\omega}_{WSR} = \frac{1}{J_w}\left(\tau_{HSR} - R_w F_{x,R} \right) \tag{5.30}$$

$$\tau_{HSL} = K\theta_{HSL} + b\dot{\theta}_{HSL} \tag{5.31}$$

$$\tau_{HSR} = K\theta_{HSR} + b\dot{\theta}_{HSR} \tag{5.32}$$

The vehicle model (5.24) and (5.25), is coupled with the eAWD model (5.26) to (5.32), through equation (5.33).

$$F_{TV} = F_{x,L} - F_{x,R} \tag{5.33}$$

The system equations are linearized around an operating point of 0.6 g's which is the lateral acceleration during a 120 KPH double lane change maneuver. The system is then cast as a discrete state space system using Euler's method.

$$x_{x+1} = \bar{A}x_k + \bar{B}u_k \tag{5.34}$$

$$y_k = Cx_{k+1} \tag{5.35}$$

The system parameters are presented in (5.36) to (5.38).

$$x_k = \begin{bmatrix} V_{y,k} & \omega_{y,k} & \omega_{TV,k} & \theta_{HSL,k} & \theta_{HSR,k} & \omega_{WSL,k} & \omega_{WSR,k} \end{bmatrix}^T \tag{5.36}$$

$$u_k = \begin{bmatrix} \tau_{TV,k} \end{bmatrix} \tag{5.37}$$

$$y_k = \begin{bmatrix} F_{TV,k} \end{bmatrix} \tag{5.38}$$

Applying equation (3.15), the control input for this system is presented in equation (5.39).

$$u_k = ((C\bar{B})^T QC\bar{B} + R)^{-1}(C\bar{B})^T Q(y^*_{k+1} - C\bar{A}x_k) \tag{5.39}$$

Where $u_k = \tau_{TV,k}$.

To ensure stability, Q and R must be selected such that the inverse term in (5.39) is never zero, (5.38). This will ensure that the control input u_k is bounded.

$$(C\bar{B})^T QC\bar{B} + R \neq 0 \tag{5.40}$$

Setting the values for Q and R is discussed in section 4.5

The plant model presented in equations (5.24) to (5.32) represent the front axle only. For the rear axle, (5.24) and (5.25) are modified as shown in (5.41) and (5.42).

$$\dot{V}_y = \frac{F_{y,r}}{m} - V_x\omega_y \tag{5.41}$$

$$\dot{\omega}_y = \frac{1}{J_y}\left(-bF_{y,f} + \frac{T}{2}F_{TV}\right) \tag{5.42}$$

The plant model for the rear axle consists of (5.41) and (5.42) plus the torque vectoring motor equations (5.26) to (5.32). The derivation of the controller for the rear axle is exactly the same as described for the front axle and will not be discussed here.

5.4.3 Converting the Control Yaw Moment Into Target Tire Forces

In sections 5.4.1 and 5.4.2, the vehicle level and motor level controllers are discussed respectively. In this section, the conversion of the control yaw moment calculated at the vehicle level into torque vectoring tire forces for the motor controller level is discussed.

The vehicle level controller calculates a control yaw moment M_Z, that allows the vehicle to track the reference yaw rate during a vehicle maneuver. The control yaw moment is converted into a torque vectoring tire force target, F_{TV} which is cascaded to the lower level motor controller. The idea is that F_{TV} is calculated such that the yaw moment generated by F_{TV} matches the control yaw moment calculated by the vehicle level controller. A fuzzy logic rule set is used to make this conversion. A diagram of this concept is shown in Figure 5.11. The motor controller translates the target F_{TV} into torque commands for the torque vectoring motors which then shift torque between the right and left side of the vehicle as necessary to correspond to the target value of F_{TV}.

The fuzzy membership function mapping to convert the control yaw moment to the torque vectoring tire force targets are shown in Figure 5.12 a). The membership functions are HP = high positive, MP = medium positive, LP = low positive, HN = high negative, MN = medium negative, and LN = low negative. The fuzzy rule surface plot showing the relationship between M_z and F_{TV} is presented in Figure 5.12 b)

There are several reasons why the fuzzy rule set is advantageous to use as part of this control strategy. First, the system provides robust peformance. The vehicle model does not have to be perfect for the fuzzy rules to work. Second, a mathematical model between M_z and F_{TV} is not needed. The fuzzy rules are based on an intuitive understanding of the relationship between M_z and F_{TV} which makes them straightforward to design and implement. Finally, the fuzzy rules enforce physical constraints on F_{TV} through the upper and lower bounds of the membership functions.

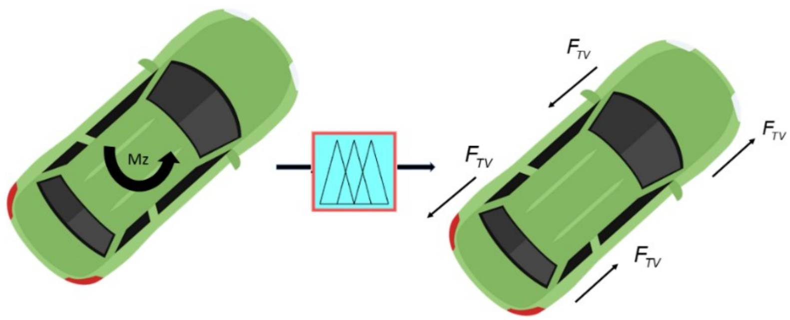

Figure 5.11 Control Mz is converted to F_{TV} targets

The fuzzy rules create a linear relationship between M_z and F_{TV}. It is necessary for the relationship to be linear because it is required that the yaw moment generated by the actuators (torque vectoring motors) match the yaw moment commanded by the vehicle level controller. If the relationship is not linear, the controller strategy does not work. The simulation results for a double lane change is presented in Section 5.6. The simulation results for the nonlinear relationship between M_z and F_{TV} is presented and discussed in section 5.6.5.

M_z	F_{TV}
HN	HP
MN	MP
LN	LP
Null	Null
LP	LN
MP	MN
HP	HN

Figure 5.12 a) Membership function to convert from Mz to F_{TV}

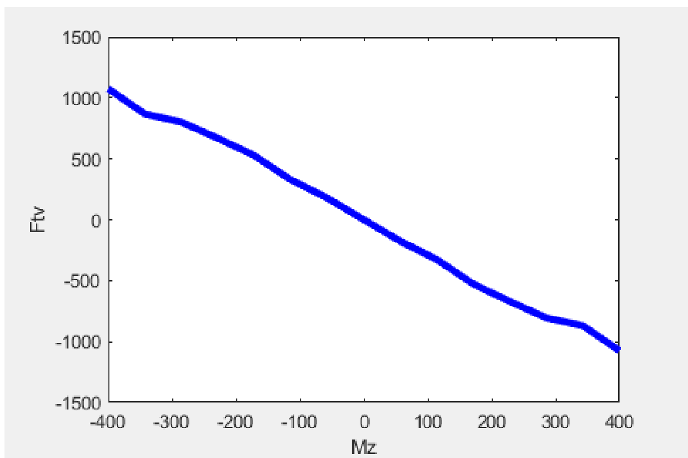

Figure 5.12 b) Fuzzy Logic Rule Surface Plot

5.5 State Estimation for V_y

The lateral vehicle controller involves two state variables, V_y and ω_y. Because ω_y can be accurately measured using available sensor technology, it is assumed that there is an accurate value available for control purposes. However, there is not a sensor available for V_y, so that state variable has to be estimated. A COO will be used to estimate the lateral velocity, similar to the one used to estimate longitudinal velocity. The diagram for the estimator is presented in Figure 5.13. The COO uses the lateral acceleration, A_y as the system output. The lateral acceleration is measured from a vehicle sensor, so it is appropriate for this usage. The controller tries to minimize the error between the estimated lateral acceleration, $\hat{A}_y$, and the measured lateral acceleration A_y using the the estimation model as the plant and a WOSA controller. The lateral tire forces are the control inputs into the estimation model.

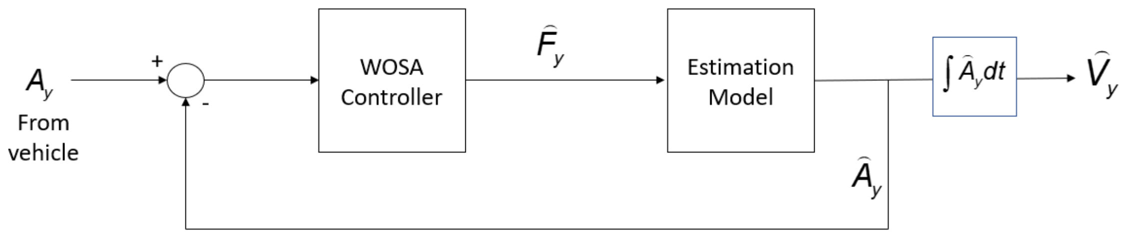

Figure 5.13 Conceptual Diagram for COO to estimate V_y

The estimation model is based on (5.1), and is presented again in (5.43).

$$\dot{V}_y = \frac{1}{m}\left(F_{y,f} + F_{y,r}\right) - V_x\omega_y \tag{5.43}$$

The linear discrete system model is presented in (5.44) and (5.45).

$$X_{k+1} = \bar{A}x_k + \bar{B}u_k + d_k \tag{5.44}$$

$$y_k = Cx_x \tag{5.45}$$

Where

$\bar{A} = [1]$

$\bar{B} = t_s\left[\frac{1}{m}\right]$

$C = [1]$

$x_k = \left[V_{y,k} \right]$

$u_k = \left[F_{y,f,k} + F_{y,r,k} \right] = \left[\hat{F}_{y,k} \right]$

$d_k = -\omega_{y,k} V_{x,k}$

The system output is (5.46).

$$y_k = V_{y,k} \tag{5.46}$$

Applying (3.15), the control input is presented in (5.47).

$$u_k = ((C\bar{B})^T QC\bar{B} + R)^{-1} (C\bar{B})^T Q(y^*_{k+1} - C\bar{A}x_k - d_k) \tag{5.47}$$

Where $u_k = \hat{F}_{y,k}$.

The results of the estimation for V_y for a double lane change are presented in Figure 5.14. The results show that the estimate overshoots the CarSim calculation of V_y by a small amount, but is a reasonable estimate of the state variable. The double lane change maneuver is discussed in more detail in section 5.7.

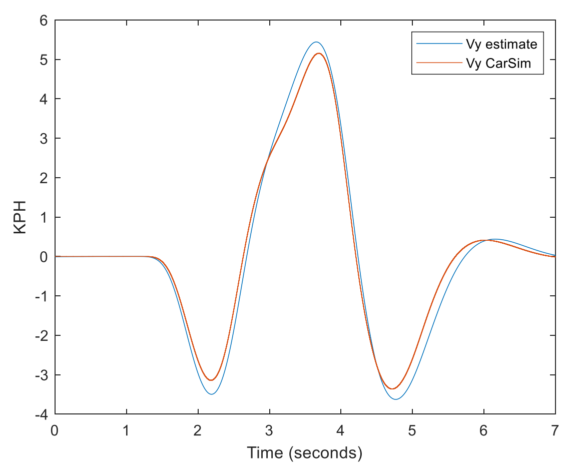

Figure 5.14 Estimate of Vy vs CarSim

Even though it is not necessary to estimate F_y, it is interesting to note that the COO does provide the estimate, shown in Figure 5.15.

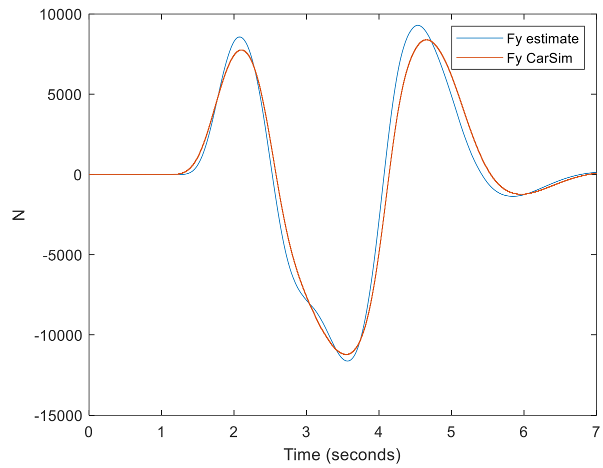

5.15 Estimate of Fy vs CarSim

5.6 Simulation Results

The control strategy was simulated for a 120 KPH double lane change maneuver using Simulink and CarSim as described section 2.4. A double lane change is an emergency maneuver when the vehicle moves over one lane, and then moves back into the original lane. It simulates avoiding an obstacle in the road. This maneuver is a standard procedure for evaluating lateral motion control performance. A diagram of the vehicle path in CarSim is presented in Figure 5.16. CarSim uses an internal driver model to provide closed loop steering inputs. For the lateral motion control case, only the torque vectoring motors are used. The traction motor torques for the front and rear motors are held at a constant value to maintain the vehicle speed as close to 120 KPH as possible.

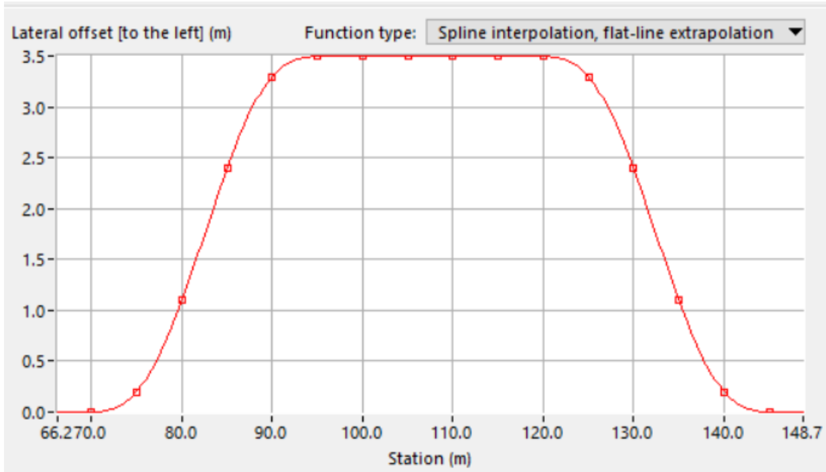

Figure 5.16 Double Lane Change Path in CarSim

5.6.1 High Surface Friction Double Lane Change

The double lane change was run on a high friction road surface with coefficient of friction $\mu = 1$. The resulst of the simulations are presented in Figure 5.17. The first simulation run was done with the torque vectoring motors not active which means the torque vectoring motor torque commands were set to 0 (Figure 5.17 a). Because the maneuver was done on a high friction surface, the vehicle is able to maintain control. But without the assistance of the torque vectoring motors, the actual yaw reference does deviate from the reference yaw reference some. In the simulation with the torque vectoring motors active, (Figure 17 b), the motors assist the closed loop driver and the actual yaw rate does track the reference pretty closely. The path tracking results are shown in Figure 5.18. The path tracking for the the case where the torque vectoring motors are not active (Figure 5.18 a)) shows slightly more deviation from the target path than for the case where the torque vectoring motors are active (Figure 5.18 b).

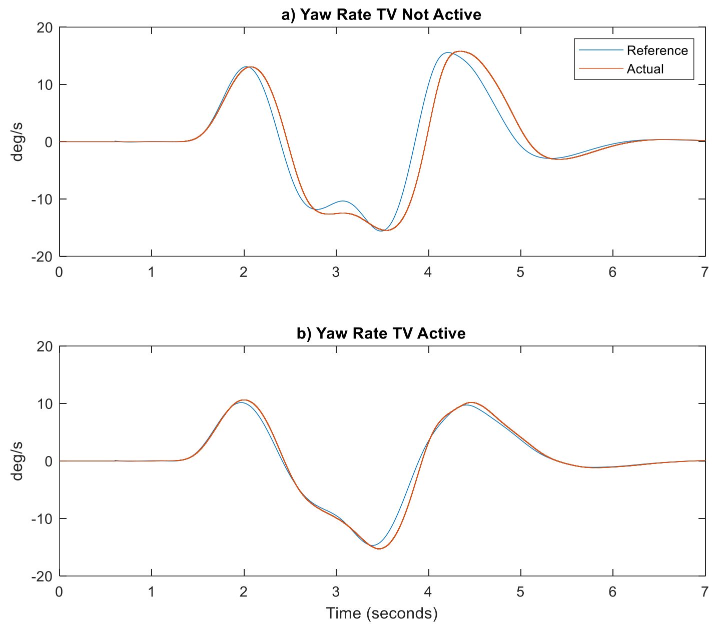

Figure 5.17 Yaw rate response for high surface friction double lane change

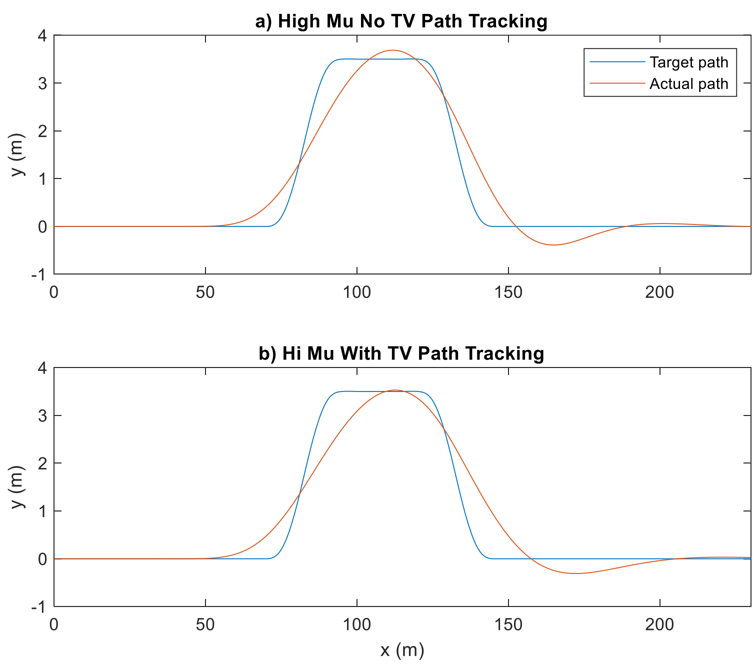

Figure 5.18 Path tracking for high friction surface double lane change

5.6.2 Low Surface Friction Double Lane Change

The second driving case involves performing the double lane change maneuver on a low friction road surface with $\mu = 0.5$. This represents a road soaked in rain. Maintaining vehicle stability for a high speed double lane change under these conditions is very challenging. To demonstrate the effectiveness of the WOSA torque vectoring controller for this driving case, three driving scenarios will be presented and discussed.

In the first scenario, the double lane change is performed with the torque vectoring motors inactive. This result is shown in Figure 5.19 a). Without the aid of the torque vectoring motors, the vehicle cannot maintain control.

The second scenario involves performing the double lane change using a yaw rate reference that is not limited to account for the low friction surface. This result is shown in Figure 5.19 b). In this scenario, the tire side slip angles are excessive, and the closed loop driver has difficulty completing the maneuver. This is evidenced by the yaw rate reference and actual yaw rate interaction in seconds 5, 6 and 7 of the simulation. The closed loop driver in trying to maintain control with steering wheel inputs, and the controller is responding to those inputs.

The third scenario involves performing the double lane change using the limited yaw rate reference as discused in section 5.3.2, equation (5.9), which is repeated here in (5.48). This result is shown in Figure 5.19 c).

$$\dot{\omega}_{y,\lim} = \frac{A_y g}{V_x} \tag{5.48}$$

The limited yaw rate reference represents the theoretical maximum yaw rate for the road surface to prevent tire saturation and excessive tire side slip angle. The vehicle is able to track the limited yaw rate target, and maintain control, even on the low friction surface.

The path tracking for the scenarios is presented in Figure 5.20. When the torque vectoring motors are not active, the vehicle slides out of control as shown in Figure 5.10 a). When the torque vectoring motors are active and the limited yaw rate target is applied, the vehicle is able to maintain control and successfully complete the double lane change, though there is deviation from the target path as shown in Figure 20 b). This result is acceptable for this driving situation.

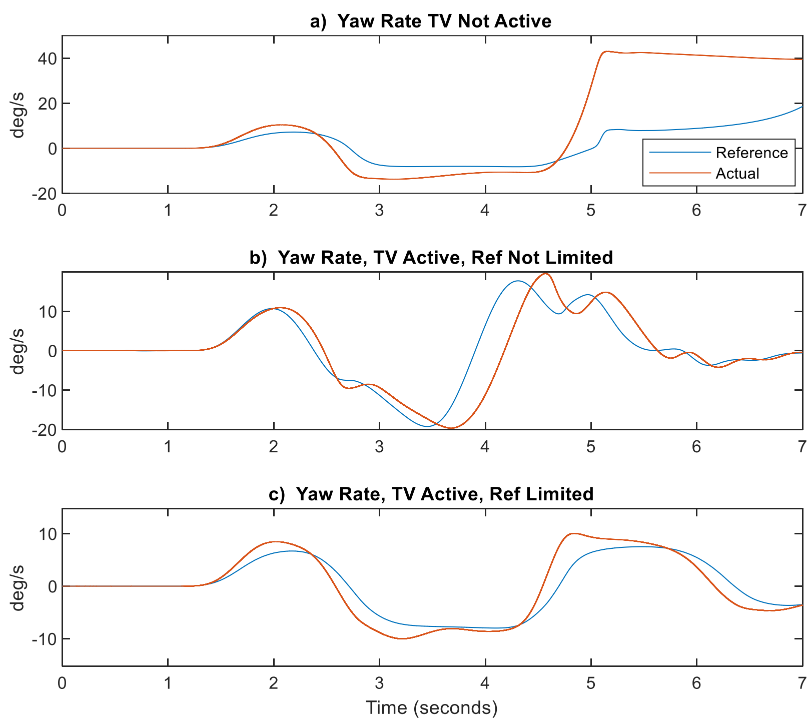

Figure 5.19 Yaw rate response on low friction road surface

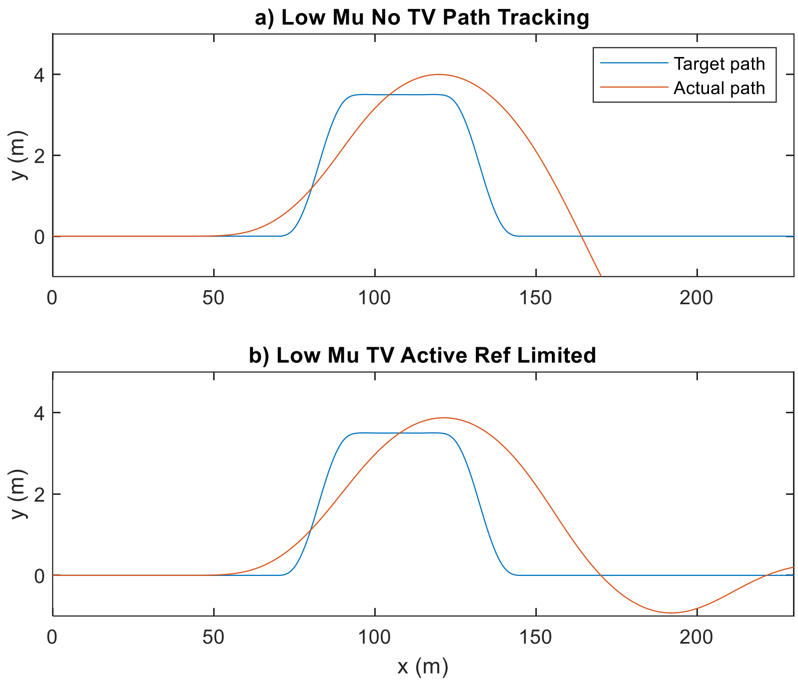

Figure 5.20 Path tracking for low friction surface double lane change

5.6.3 Comparison on High Friction and Low Friction Surfaces

Here, the controller outputs for the double lane change on the high friction and low friction surface are compared and presented in Figure 5.21. Note that the controller outputs on the low friction surface are considerably higher than they are for the high friction surface. This is because the controller input signal has to be more active to successfully track the reference signal input on the low friction surface.

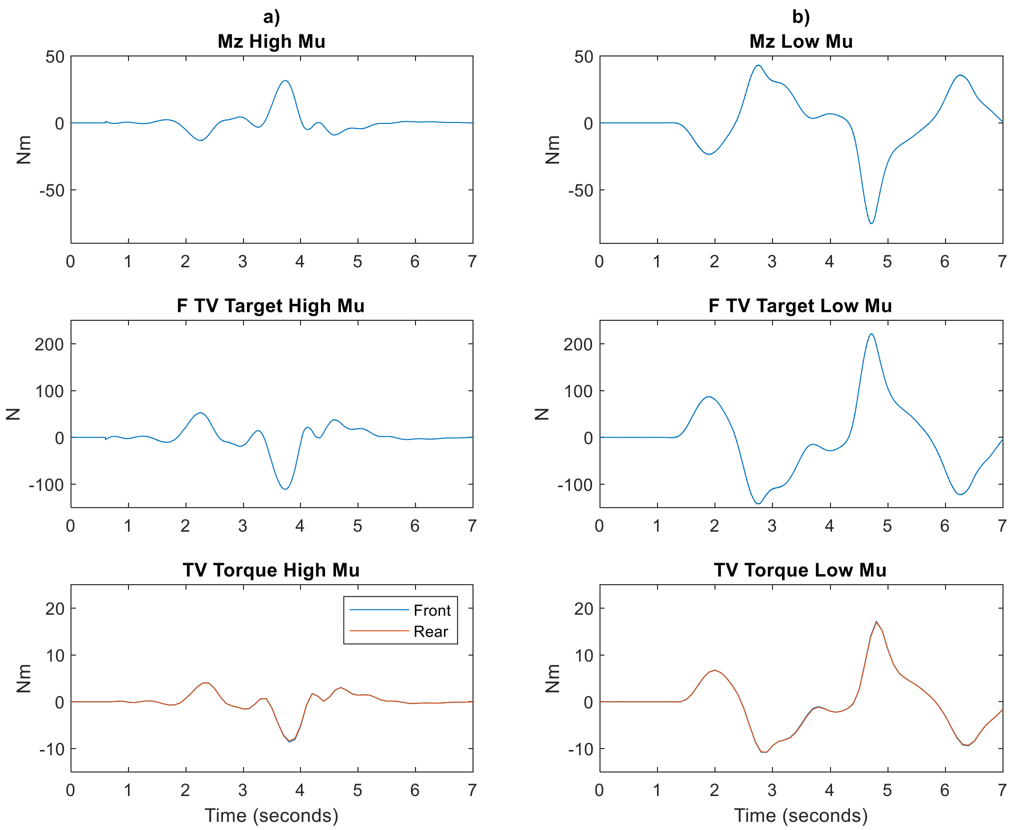

Figure 5.21 Controller output comparison for the high friction and low friction cases

5.6.4 Side Slip Angle

The effectiveness of the WOSA controller can also be evaluated by looking at the tire slip angles, α and the vehicle side slip angle, β. These concepts are discussed in detail in section 5.1. The comparison of the slip angles is presented in Figure 5.22, which shows the tire slip angles for the front and rear axles, (α_f, α_r) and the vehicle side slip angle (β) for the four double lane change cases discussed previously. For Figure 5.22 a), the double lane change on the high friction surface is presented. The side slip angles peak at around 3 degrees. For Figure 5.22 b), the double lane change on the low friction surface with no torque vectoring motor is presented. The vehicle slides out of control and all of the slip angles go to an extreme value (-50 degrees) which is below the scale shown on the graph. For Figure 5.22 c), the double lane change on the low friction surface with the unlimited yaw reference is presented. The slip angles max out at about 10 degrees, which is significantly higher than the high friction case. In Figure 5.22 d) the double lane change on the low friction surface with the limited yaw rate reference is presented. The slip angles are well controlled and peak at around 6 degrees for the front axle slip angle, and about 2.5 degrees for the rear axle slip angle and the vehicle side slip angle.

One caution has to be considered when using the limited yaw rate reference for the low friction surface. As noted above, the tire slip angle for the front axle is higher than for the rear axle. This indicates that the vehicle could be in an oversteer condition. To properly design the controller for this situation, it would be necessary to subjectively evaluate the amount of understeer and adjust the limited yaw rate reference as necessary.

5.6.5 Nonlinear Fuzzy Rules for Mz and F_{TV} Simulation Results

In this section, the 120 KPH double lane change on a high friction road surface is simulated for two nonlinear fuzzy rule sets. In Figures 5.23 and 5.25, two nonlinear surface plots are presented for the relationship between M_Z and F_{TV}. In Figures 5.24 and 5.26, the respective simulation results comparing the yaw rate reference with the actual yaw rate are presented. The nonlinear relationship causes the controller strategy not to work, and the vehicle does not successfully complete the double lane change maneuver.

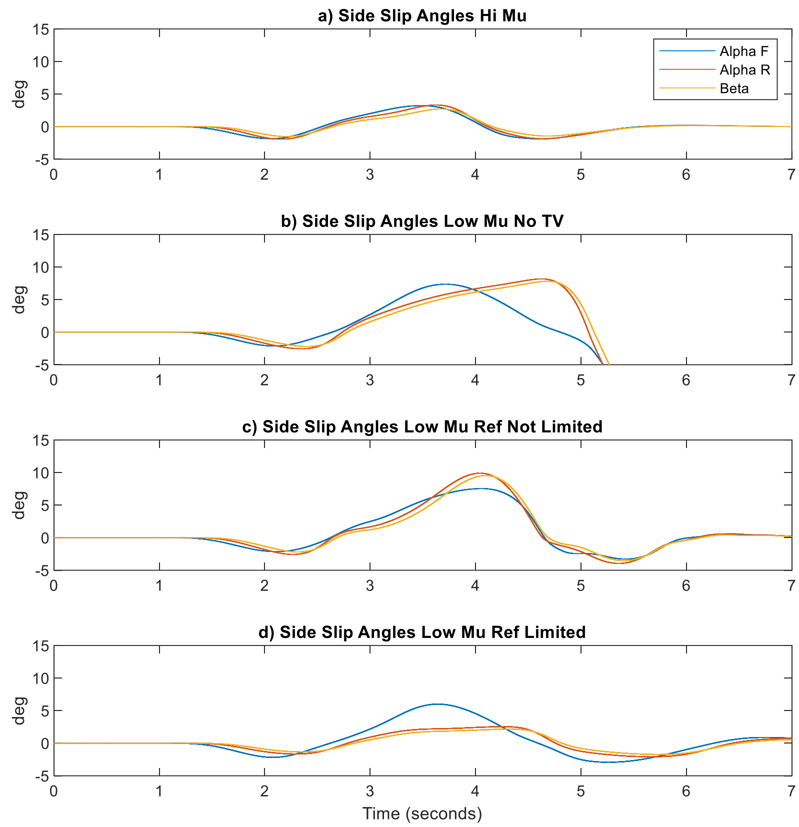

Figure 5.22 Side slip angle comparison

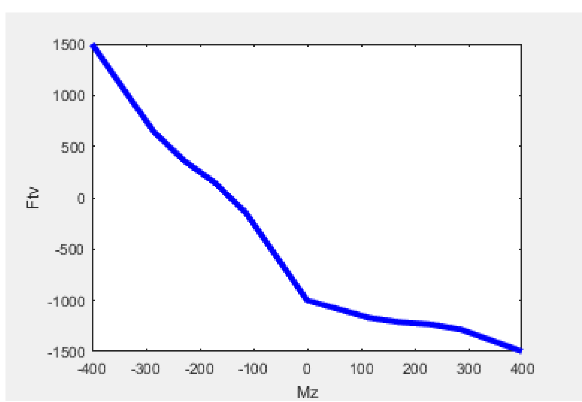

Figure 5.23 Nonlinear surface plot

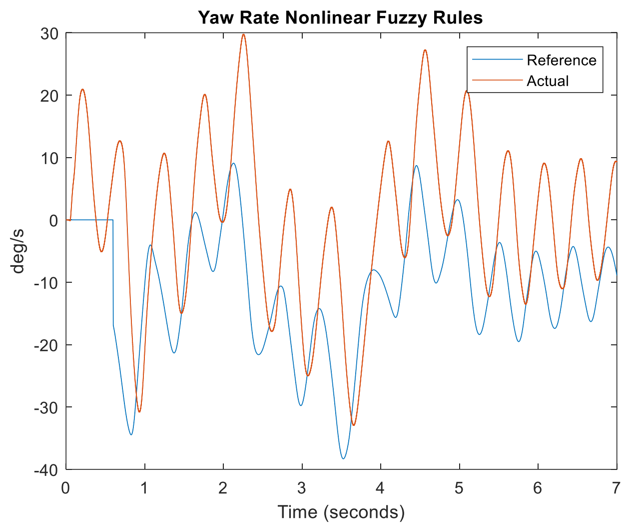

Figure 5.24 Double lane change simulation result

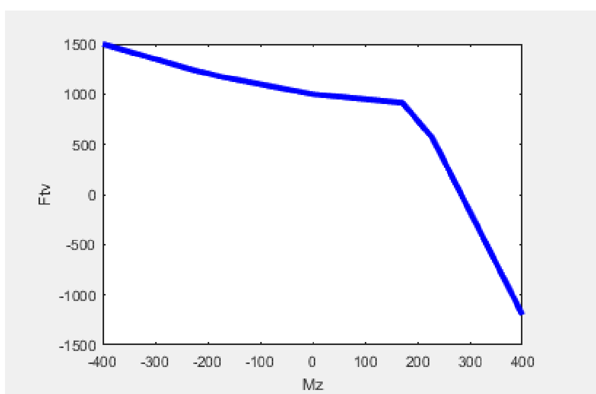

Figure 5.25 Nonlinear surface plot

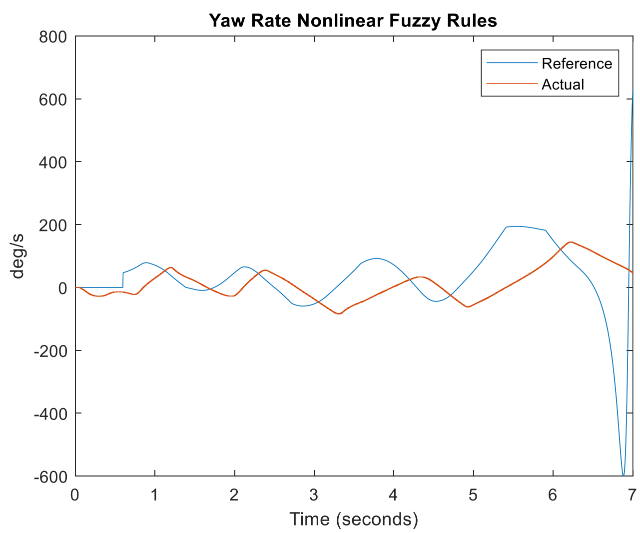

Figure 5.26 Double lane change simulation result

CHAPTER SIX

ADDITIONAL NONLINEAR LATERAL MOTION CONTROLLERS

This chapter presents three additional nonlinear controllers to calculate the control yaw moment at the vehicle level. These control strategies use the same torque vectoring motor controller as described in section 5.4.2. It is interesting to see how well these controller strategies work with the fuzzy logic rule set to calculate a control yaw moment to control the lateral vehicle motion. The three additional controllers that are considered are nonlinear model predictive control (NLMPC), feedback linearization control (FLC) and sliding mode control (SMC). It is particularly interesting to look at the NLMPC controller because it is a predictive controller, similar to the WOSA.

6.1 Non Linear Model Predictive Controller

Model Predictive Control (MPC) optimizes a constrained objective function over a specified time horizon. At each sample time, the controller receives an estimate of the current state, and uses that information along with a system model to calculate a sequence of optimized control inputs. There are two time horizons that are used. The prediction horizon represents the number of time intervals into the future for the prediction model. The control horizon represents the number of time intervals into the future for calculating the control sequence. The control horizon must be less than or equal to the prediction horizon. Once the optimized control sequence is calculated, the first element of the sequence is used as the control input at the current time. The process is repeated over again at the next sample time. Because of this, MPC is often referred to as a receding horizon controller. The concept of MPC is presented in Figure 6.1. In this thesis, the plant is nonlinear, thus a nonlinear optimization strategy is used and the controller is called non-linear MPC (NLMPC).

6.1.1 Literature Review for NLMPC

Many researchers have tackled the problem of using MPC or NLMPC to control yaw and side slip. In [17], a piecewise-linearized MPC strategy is implemented for lateral yaw control on a double lane for an eAWD powertrain vehicle. The strategy requires the online linearization of the system to calculate the control input at each time step. This approach addresses the nonlinearity of the plant, but is not feasible to implement in a real vehicle. This approach was used for the purposes of comparison to other control strategies. In [41], an explicit NLMPC strategy is employed to design a controller to track yaw rate and side slip angle simultaneously. In this strategy, a suboptimal solution for the objective function and constraints is solved off-line and stored in computer memory. The controller looks up the correct solution based on operating conditions during vehicle operation. This approach offers the advantage of fast real time execution. However, for this approach, a very complicated objective function was developed which resulted in a solution space that is quite large. In [42], an NLMPC strategy that combines the use of the vehicle model with the Pacejka tire model to represent the lateral tire forces is used. This is an unusual approach because, typically, the tire model is assumed to be linear, but the Pacejka model adds a significant nonlinear component to the system model.

In this thesis, the NLMPC is implemented using a vehicle model to calculate the upper level yaw moment control input, and fuzzy rules are used to translate the control input into target tire forces for the motor controllers as described in Chapter 5.

Furthermore, the longitudinal vehicle speed is not treated as a constant, but is included as a state variable, which makes the system nonlinear.

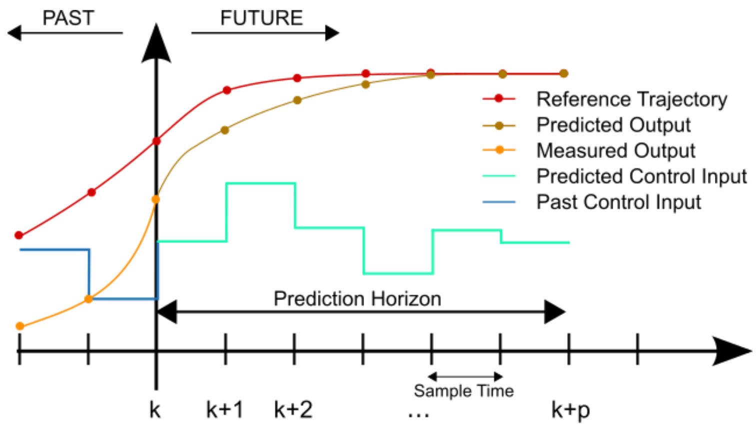

Figure 6.1 MPC control concept [43]

6.1.2 Formulation of the NLMPC Controller

The lateral motion equations are presented again in (6.1) and (6.2). The equations are supplemented with (6.3) to allow V_x to be treated as a state variable.

$$\dot{V}_y = \frac{1}{m}\left(F_{y,f} + F_{y,r}\right) - V_x \omega_y \tag{6.1}$$

$$\dot{\omega}_y = \frac{1}{J_y}\left(aF_{y,f} - bF_{y,r} + M_z\right) \tag{6.2}$$

$$\dot{V}_x = 0 \tag{6.3}$$

The system represented by (6.1), (6.2) and (6.3) is cast as a nonlinear system in (6.4) and (6.5).

$$\dot{x}(t) = f(x(t)) + Bu(t) + B_\delta \delta(t) \tag{6.4}$$

$$y(t) = Cx(t) \tag{6.5}$$

The parameters of the system model are presented in equations (6.6) to (6.12).

$$f(x) = \begin{bmatrix} -\frac{2.569}{V_x} & \frac{0.2263}{V_x} - V_x & \frac{1.284(V_y + 1.3\omega_y)}{V_x^2} - \omega_y + \frac{1.284(V_y - 1.476\omega_y)}{V_x^2} \\ \frac{0.0826}{V_x} & -\frac{1.814}{V_x} & \frac{0.6094(V_y + 1.3\omega_y)}{V_x^2} - \frac{0.692(V_y - 1.476\omega_y)}{V_x^2} \\ 0 & 0 & 0 \\ & & \end{bmatrix} \tag{6.6}$$

$$B = \begin{bmatrix} 0 \\ 1 \\ 0 \end{bmatrix} \tag{6.7}$$

$$B_\delta = \begin{bmatrix} 1.284 \\ 0.6094 \\ 0 \end{bmatrix} \tag{6.8}$$

$$C = \begin{bmatrix} 0 & 1 & 0 \end{bmatrix} \tag{6.9}$$

$$x = \begin{bmatrix} V_y & \omega_y & V_x \end{bmatrix}^T \tag{6.10}$$

$$y = \begin{bmatrix} \omega_y \end{bmatrix} \tag{6.11}$$

$$u = \begin{bmatrix} M_z \end{bmatrix} \tag{6.12}$$

The system in (6.4) and (6.5) is discretized using Euler's method.

$$x_{k+1} = x_k + t_s(f(x_k) + Bu_k + B_\delta \delta_k) \tag{6.13}$$

$$y_k = Cx_k \tag{6.14}$$

The objective function is presented in (6.15).

$$\underset{\min(y,u)}{J} = Q\sum_{1}^{m}\left(y_{ref,k} - y_k\right)^2 + R\sum_{1}^{n}\left(\Delta u\right)^2 \tag{6.15}$$

In this formulation *m* is the prediction horizon and *n* is the control horizon. Also, Q and R are weighting matrices for the system output and inputs respectively. The objective function in (6.15) is constrained by (6.16) which represents the model projection over the prediction horizon.

$$x_{k+1} = x_k + t_s(f(x_k) + Bu_k + B_\delta \delta_k) \qquad k = 1:(m-1) \tag{6.16}$$

Finally, a linear constraint is applied to the control input variable, M_z to limit its value for the purposes of the fuzzy logic rule set that converts the yaw moment into tire force targets.

$$M_{z,\min} \le M_z \le M_{z,\max} \tag{6.17}$$

The NLMPC controller was designed using the Matlab MPC toolbox and implemented using the *fmincon* function.

6.1.3 Simulation Results

The 120 KPH dual lane change maneuver was simulated on a high friction surface and a low friction surface as described previously. The results of both maneuvers are presented in Figure 6.2. In Figure 6.2 a), the high friction maneuver is shown. The controller is able to track the reference yaw rate reasonably well.

The low friction simulation result is presented in Figure 6.2 b). In this driving case the reference yaw rate is limited as described in section 5.3.2 to prevent tire saturation on the low friction surface.

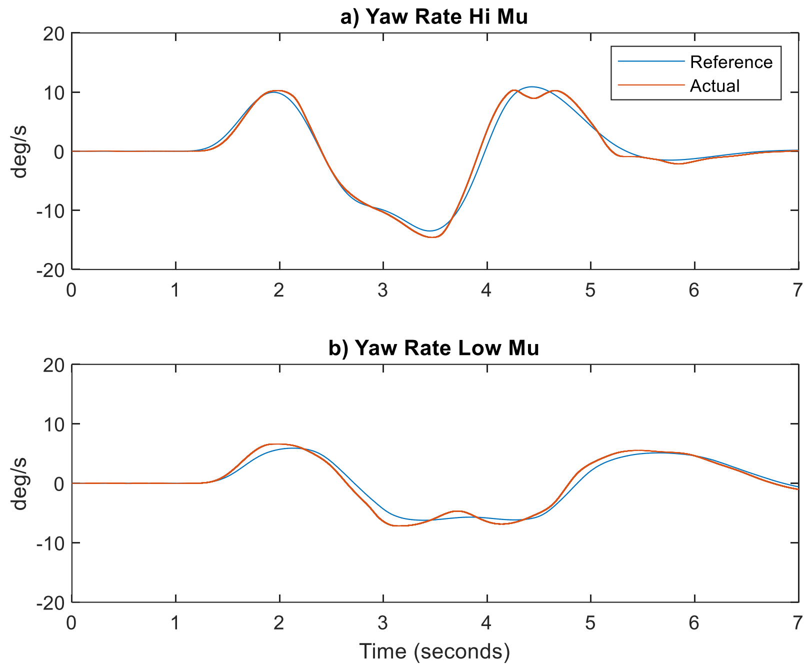

Figure 6.2 Yaw rate tracking comparison for NLMPC controller

The path tracking for the high friction and low friction driving cases are shown in Figure 6.3. The high friction case is shown in Figure 6.3 a), and the low friction case is shown in Figure 6.3 b). For the low friction case, the vehicle does deviate from the target path, but is still able to maintain control and complete the maneuver.

The outputs for the NLMPC controller for the high friction and low friction driving cases are compared in Figure 6.4. The controller input, M_z for the high friction driving case is much lower than it is for the low friction driving case. This result is expected because the controller has to work harder in the low friction case to track the reference yaw rate. This pattern is repeated for the F_{TV} targets and the torque vectoring motor torque requests.

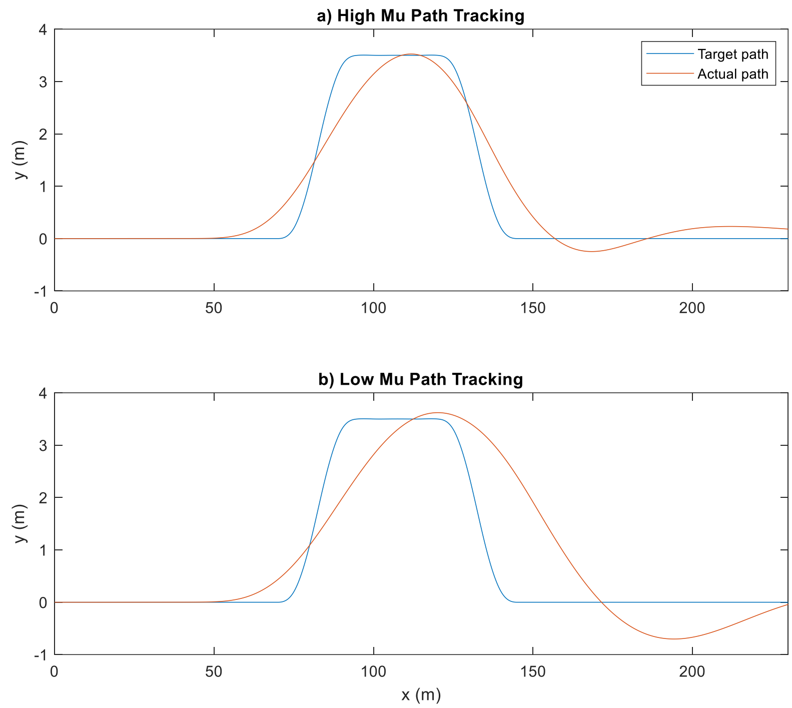

Figure 6.3 Path tracking comparison for NLMPC controller

6.2 Feedback Linearization Controller

The general principle of feedback linearization is to algebraically transform a nonlinear system into a linear system so that well-known linear control techniques can be used on the transformed system.

6.2.1 Literature Review for FLC

There are not a lot of examples of FLC for automotive controls in the literature. In [44], a FLC is designed for lateral control of a vehicle based on the steering input. In this controller, the system assumes that the longitudinal vehicle speed is constant to simplify the plant model. In, [45] the motion of an autonomous vehicle for path tracking is controlled using FLC. The vehicle model is supplemented with a nonlinear tire model which yields a fairly complex nonlinear plant model. The FLC approach is used to linearize the model in terms of the state variables, and an LQR controller is applied to the system.

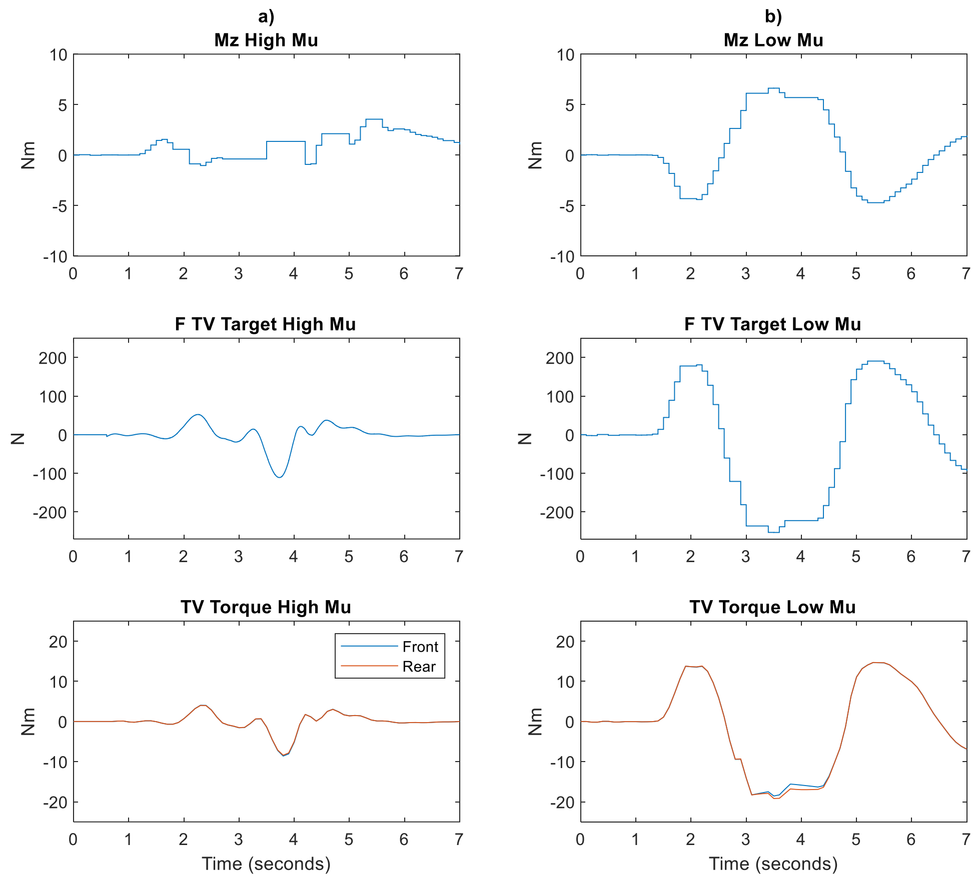

Figure 6.4 NLMPC Controller output comparison for the high friction and low friction cases

There are three main approaches to feedback linearization. Full state feedback linearization is used when all of the state variables are available for measurement or estimation. Partial state feedback linearization uses a subset of the state variables to design the controller. Output feedback linearization uses measurements of the system output only. In this work, an FLC strategy is applied to the lateral motion vehicle model by linearizing the output feedback term.

6.2.2 Formulation of the FLC

The lateral vehicle motion equations (6.1) to (6.3) are presented again in (6.18) and (6.20). The system parameters are the same as presented in (6.6) to (6.12).

$$\dot{V}_y = \frac{1}{m}\left(F_{y,f} + F_{y,r}\right) - V_x\omega_y \tag{6.18}$$

$$\dot{\omega}_y = \frac{1}{J_y}\left(aF_{y,f} - bF_{y,r} + M_z\right) \tag{6.19}$$

$$\dot{V}_x = 0 \tag{6.20}$$

The control input for this system is contained in (6.19) which is a nonlinear equation because of the expressions for $F_{y,f}$ and $F_{y,r}$ which are presented in (5.3),(5.4),(5.5) and (5.6). Using the output feedback linearization strategy, a linearized controller can be designed.

Letting $u = M_z$ and $P = \dot{\omega}_y$ and rewriting equation (6.19) with the new variables yields (6.21).

$$P = \frac{1}{J_y}\left(aF_{y,f} - bF_{y,r} + u\right) \tag{6.21}$$

Rearranging (6.21) to isolate u yields (6.22).

$$u = J_yP - aF_{y,f} + bF_{y,r} \tag{6.22}$$

For (6.21), P is defined in (6.23) as a proportional gain controller, where k is the gain constant.

$$P = k\left(\omega_{y,ref} - \omega_y\right) \tag{6.23}$$

The control input defined in (6.22) represents the feedback linearization control law. The control input cancels out the nonlinearities inherent in equation (6.19). This can be seen if (6.22) is substituted into (6.21), shown in (6.24), where P is as defined in (6.23).

$$P = \frac{1}{J_y}\left(aF_{y,f} - bF_{y,r} + J_y P - aF_{y,f} + bF_{y,r}\right) \tag{6.24}$$

<u>6.2.3 Simulation Results</u>

The 120 KPH double lane change was performed on a high friction and low friction road surface using the FLC as described previously. The results are presented in Figure 6.5. The high friction case is shown in Figure 6.5 a), and the low friction case is shown in Figure 6.5 b). For the high friction case, the vehicle is able to track the reference yaw rate pretty closely. For the low friction case, there is some deviation between the reference yaw rate and the actual yaw rate because of the low friction surface. However, the vehicle is still able to successfully complete the maneuver. For the low friction case, the limited yaw rate reference as described in section 5.3.2 is used.

The path tracking for the double lane change result is presented in Figure 6.6. The high friction result is presented in Figure 6.6 a), and the low friction result is presented in Figure 6.6 b). For the high friction case, the vehicle is able to follow the target path reasonably well. For the low friction case, the vehicle does deviate from the path, but is able to complete the maneuver, and this result is acceptable for this driving case.

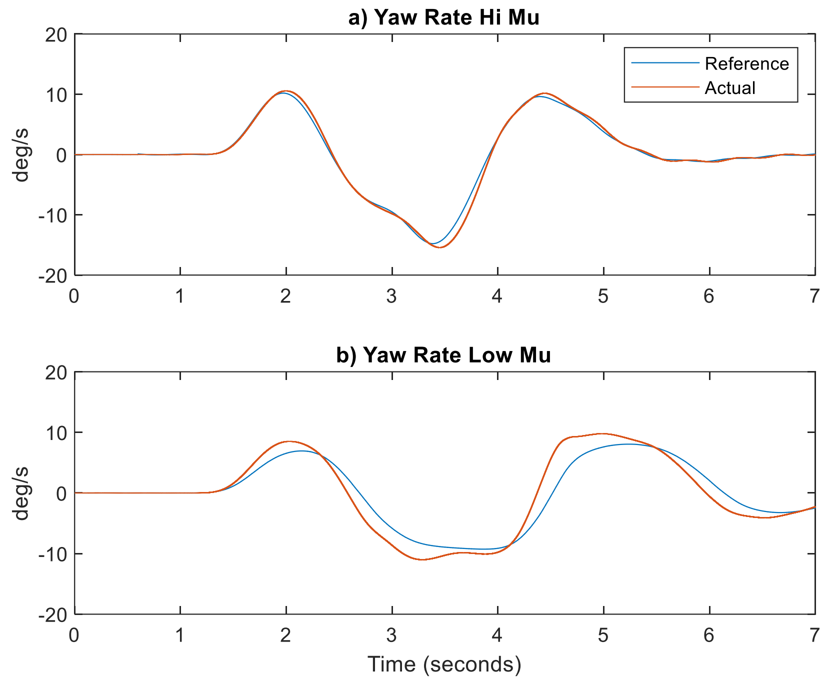

Figure 6.5 Yaw rate tracking comparison for the FLC controller

The outputs for the FLC for the high friction surface and low friction surface are presented in Figure 6.7. It is interesting to note that for the FLC, the control input for M_z is much larger than for the other controllers (WOSA, NLMPC, SMC to be discussed below). One noteworthy aspect of the FLC is that it can generate very large controller input signals, which can be an issue for some applications. However, that is not an issue in this control case because the fuzzy logic rules to translate the control signal into target F_{TV}'s are set so that the boundaries of the membership functions to calculate the

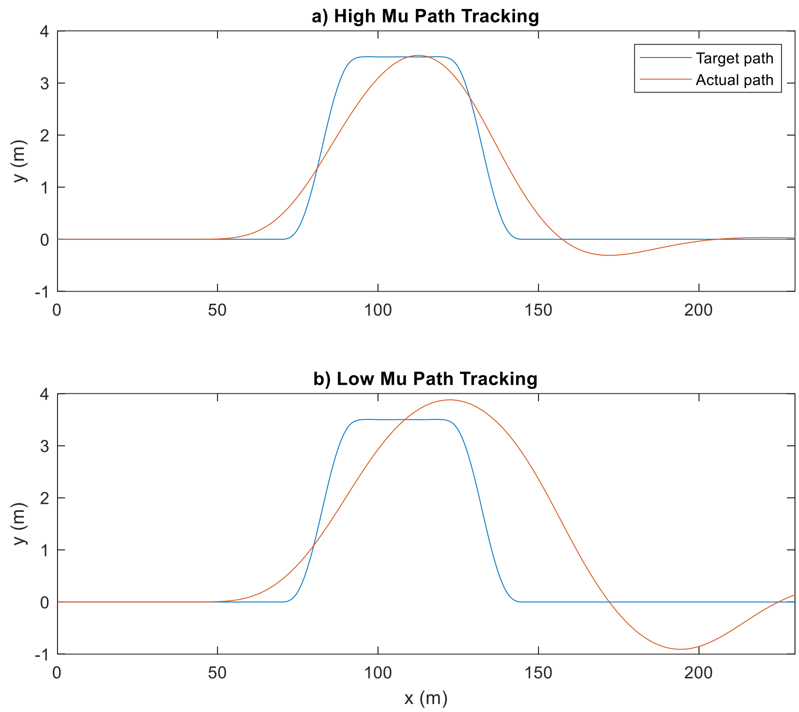

Figure 6.6 Path tracking comparison for the FLC controller

F_{TV} maximum and minimum are appropriate for the traction motor. That is one advantage of using the fuzzy rule concept as part of the integrated control scheme.

6.3 Sliding Mode Controller

The general idea of sliding mode control is to design a controller that forces the system to slide along a surface in the system phase plane. The sliding surface represents the desired dynamics of the system. The controller is designed to drive the system trajectory to the sliding surface, and to keep the trajectory close to the sliding surface.

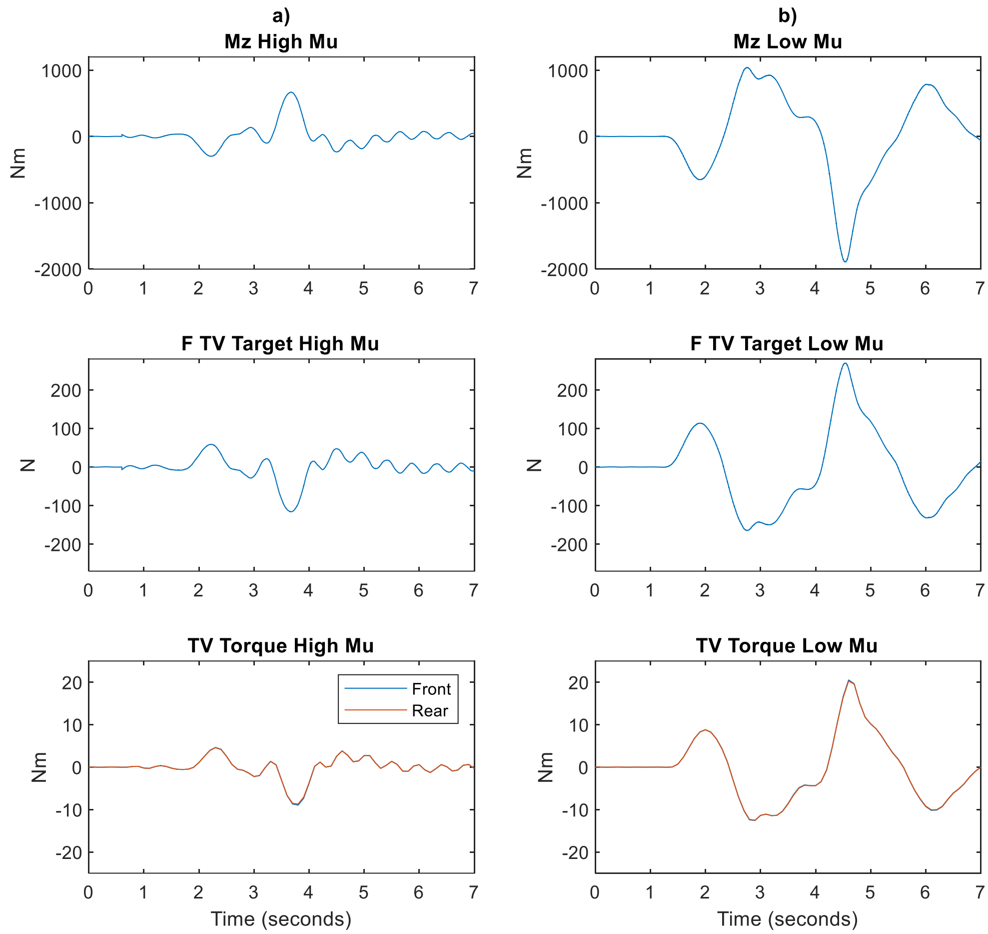

Figure 6.7 FLC controller output comparison for the high friction and low friction cases

The control law will force the system trajectory to "jump" back and forth across the sliding surface. This results in a control law that is discontinous. This discontinuousness creates a "chattering" response in the control input. A supplemental term can be added to the control law to reduce the chattering response if necessary.

The control law consists of two components. The reaching mode forces the system to the sliding surface. The switching mode forces the system to stay on or near the sliding surface. See Figure 6.8 for an illustration of this concept.

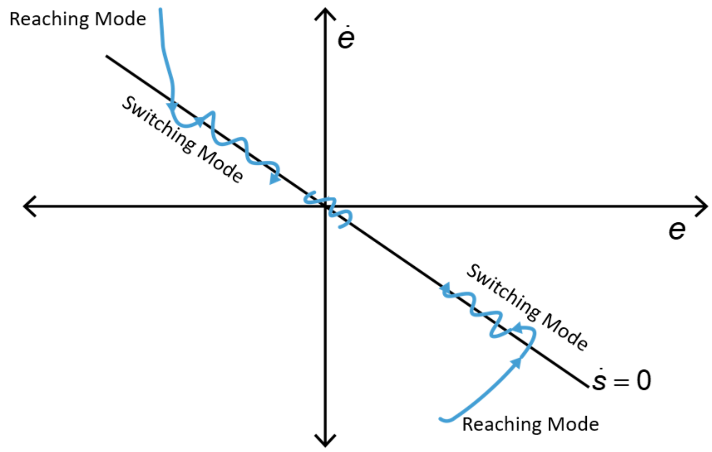

Figure 6.8 Sliding mode control concept

6.3.1 Literature review for SMC

The literature is rich with examples of SMC used to control lateral vehicle motion. Typically, the steering input is used as the control signal for yaw controllers that use SMC. In [46] and [47], a variable SMC is used for yaw control. A variable SMC uses a variable value of the switch gain term (K) in the reaching law. This variable term changes based on how far the system is from the sliding surface. There are various ways to calculate the variable switch gain term. In [48], a fuzzy SMC is used to control the vehicle yaw. A typical SMC is designed, but the switch gain term is adjusted based on a fuzzy rule set. The input into the fuzzy rule set is $s\dot{s}$ and the output is the switch gain value (K). In [49] , a simple PD type SMC is used where a gain is mulitplied by the error term and the derivative of the term, and these are added together and multiplied by sign(s) to calculate the control law. See Figure 6.9.

$$u = (\alpha | e | + \beta \dot{e}) \operatorname{sgn}(s)$$
$$s = ce + \dot{e}$$

Figure 6.9 PD type control law disussed in [48]

In [50], a SMC is designed for a powertrain with a torque vectoring rear axle. Here, sliding mode surface uses a weighted combination of the yaw rate and slip rate errors.

6.3.2 Formulation of the SMC

The SMC developed here will use the same system equations presented in section 6.1, (6.1) to (6.12). The nonlinear system equations are presented again in (6.25) and (6.26).

$$\dot{x}(t) = f(x(t)) + Bu(t) + B_\delta \delta(t) \tag{6.25}$$

$$y = Cx \tag{6.26}$$

Define the system error in (6.27) and (6.28).

$$e = y_{ref} - y \tag{6.27}$$

$$\dot{e} = \dot{y}_{ref} - \dot{y} \tag{6.28}$$

Where $\dot{y} = C\dot{x}$.

The sliding surface is defined in (6.29) and (6.30).

$$s = e \tag{6.29}$$

$$\dot{s} = \dot{e} \Rightarrow \dot{y}_{ref} - C\left(f(x(t)) + Bu(t) + B_\delta \delta(t)\right) \tag{6.30}$$

The reaching law is defined in (6.31)

$$\dot{s} = -(\varepsilon sign(s) + Ks) \tag{6.31}$$

Desirable system dynamics occur when $\dot{s}=0$. Combining (6.30) and (6.31) and setting $\dot{s}=0$ yields (6.32).

$$\dot{y}_{ref}-\left(Cf(x(t))+CBu(t)+CB_{\delta}\delta(t)\right)+\varepsilon sign(s)+Ks=0 \tag{6.32}$$

Isolating (6.32) for u yields (6.33), which is the sliding mode control law.

$$u=\left(CB\right)^{-1}\left(y_{ref}-Cf(x(t))-CB_{\delta}\delta(t)+\varepsilon sign(s)+Ks\right) \tag{6.33}$$

6.3.3 Simulation Results

The 120 KPH double lane change was simulated using the same process as decribed previously. The yaw reference tracking results for the high friction and low friction case are presented in Figure 6.9. The controller response tracks the yaw reference reasonably well for the high friction driving case, shown in Figure 6.9 a). For the low friction case, the controller uses the limited yaw rate reference as described in section 5.3.2 and there is some deviation between the yaw rate reference and the actual yaw rate, shown in Figure 6.9 b). However, the controller is able to track the reference yaw rate, and the vehicle is able to complete the maneuver. This result is acceptable for the low friction driving case.

The path tracking results of the for the double lane change maneuver for the high friction driving case and low friction driving case are presented in Figure 6.10. The high friction case is shown in Figure 6.10 a), and the low friction case is shown in Figure 6.10 b). It is clear that for the high friction case, the vehicle is able to maintain tracking of the path. For the low friction friction case, there is deviation from the path, which is acceptable for this driving case.

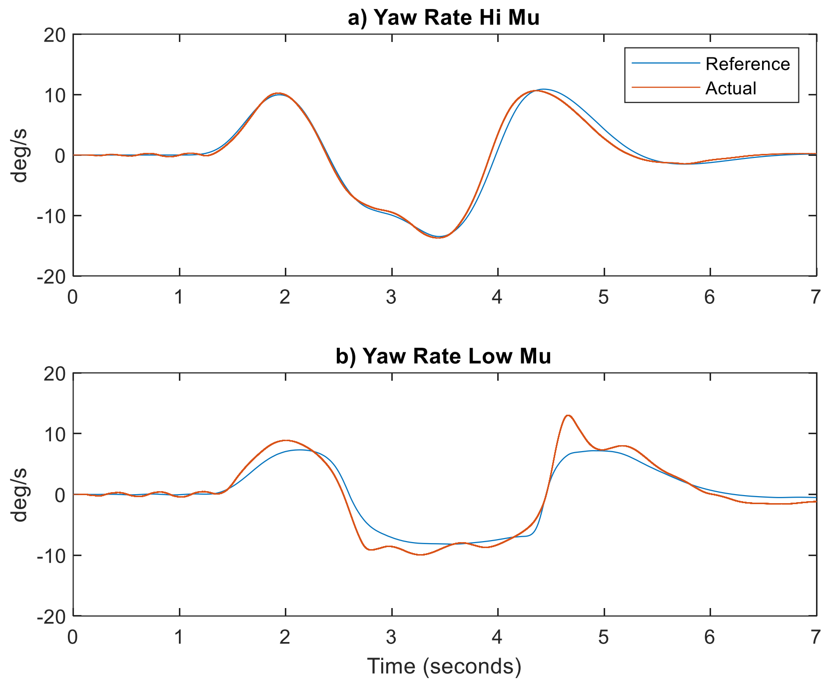

Figure 6.9 Yaw rate tracking comparison for the SMC controller

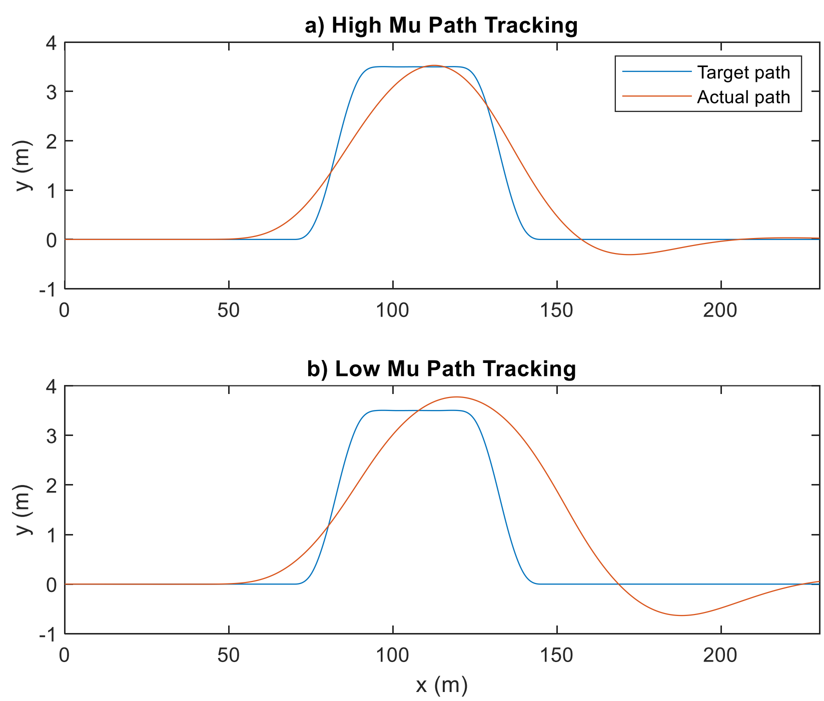

Figure 6.10 Path tracking comparison for the SMC controller

The SMC controller outputs for the high friction and low friction cases are presented in Figure 6.11. The reaching law that was used for the SMC controller significantly reduced the level of chattering that is typically present in a sliding mode control signal as can be seen in the graphs for the Mz and F_{TV}. The chattering is completely eliminated for the torque vectoring motor torque commands because the WOSA controller acts as sort of a filter for the input signal. For the low friction case, the chattering was present at a low level, but was filtered out by the WOSA controller for the motors.

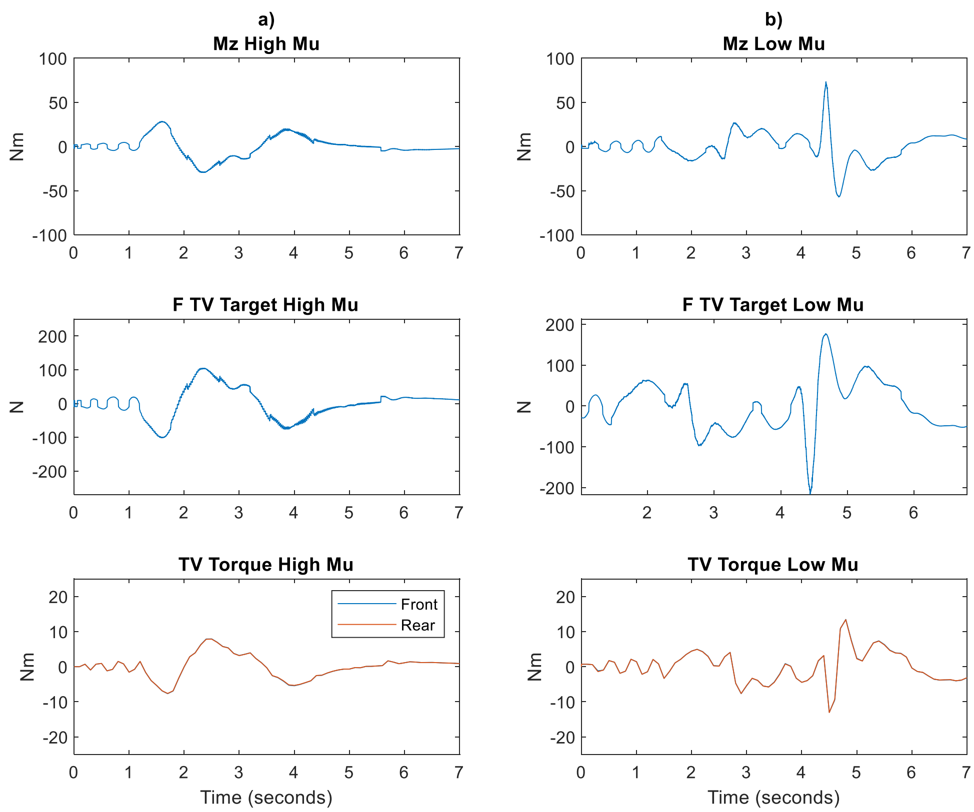

Figure 6.11 SMC controller output comparison for the high friction and low friction cases

CHAPTER SEVEN

COMPARISON OF LATERAL MOTION CONTROLLER PERFORMANCE

In Chapters 5 and 6, several lateral motor controller strategies were discussed (WOSA, NLMPC, FLC, SMC). These strategies were used in conjunction with a fuzzy rule set to control an eAWD vehicle on a double lane change on a high friction and low friction road surface. A comparison of the performances of the controller strategies is presented here.

7.1 Yaw rate comparison

The main purpose of the controller is to track the yaw rate reference signal as closely as possible. The tracking to reference performance is measured by calculating a mean squared error (MSE) index for each controller. The MSE is simply the sum of the squared errors at each sample time divided by the number of sample times for the simulation (7.1).

$$MSE = \frac{1}{n}\sum_{k=1}^{n}\left(\omega_{ref,k} - \omega_k\right)^2 \tag{7.1}$$

The summaries of the double lane change simulation results for the high friction and low friction surfaces are presented in Figures 7.1 and 7.2 respectively. On the high friction surface, the the FMC had the best performance, and the NLMPC had the worse performance. The WOSA and SMC were in the middle with similar performance.

For the low friction road surface, recall that the yaw rate target is limited to prevent tire saturation. Limiting the target makes it easier for the controller to meet. The low friction surface results show that the NLMPC had the best performance, and the WOSA had the worse, with the SMC and FLC in the middle.

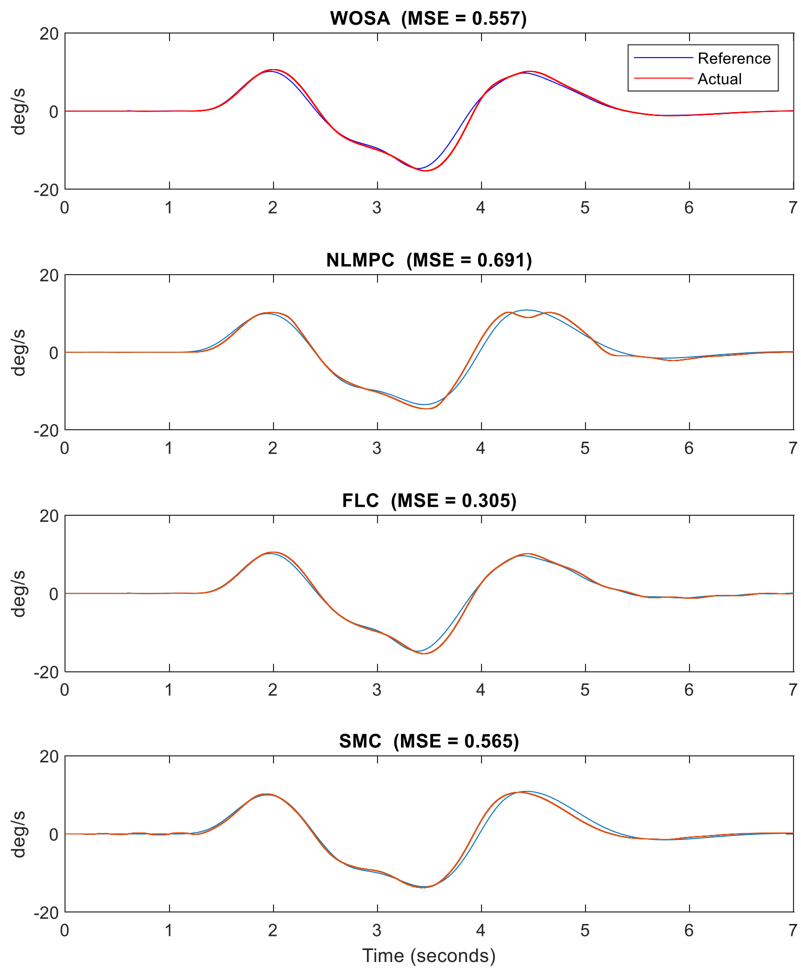

Figure 7.1 Mean Square Error comparison for high friction surface double lane change

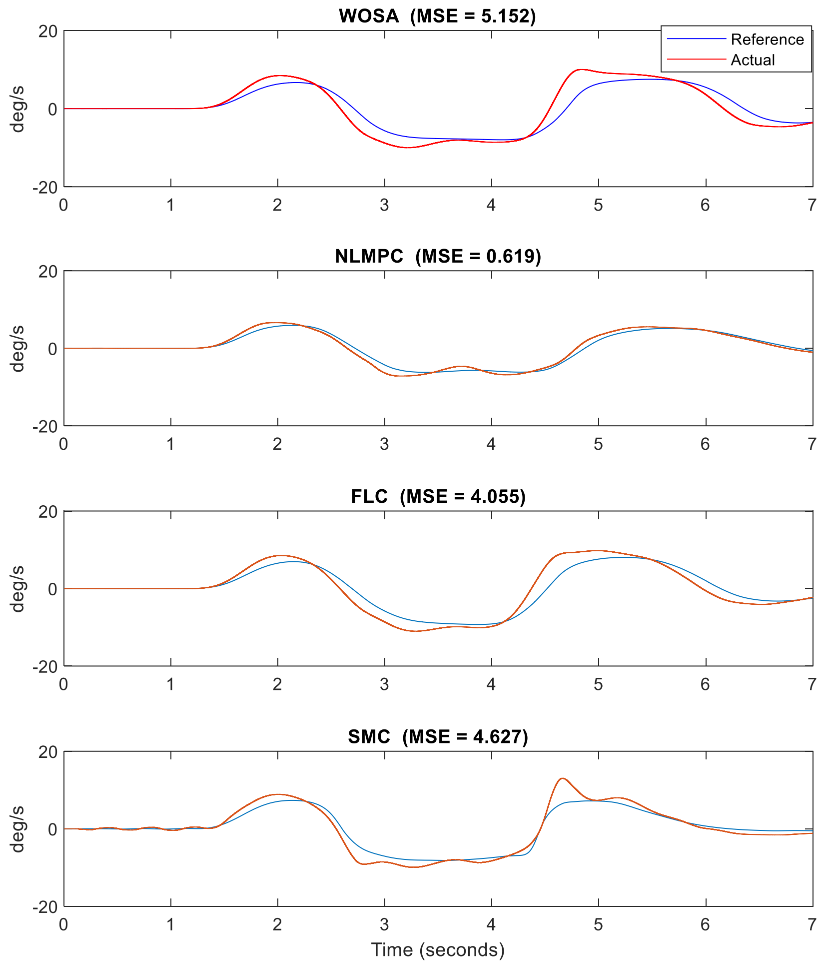

Figure 7.2 Mean Square Error comparison for low friction surface double lane change

7.2 Side slip, Ay and Vy comparison

The side slip angle (beta) at the vehicle center of gravity C.G. for high friction and low friction cases are presented in Figure 7.3. During a double lane change, it is important to minimize the side slip angle as much as possible for safety and passenger comfort. For the high surface friction case, all of the controllers are able to maintain the side slip at a reasonable level. For the low friction case, because the yaw rate target is limited, the controllers are able to limit the side slip angle, even though the vehicle is maneuvering on a low friction surface. This result demonstrates the effectiveness of the controllers. It should be noted that the NLMPC controller limited the side slip angle the most during the low friction maneuver.

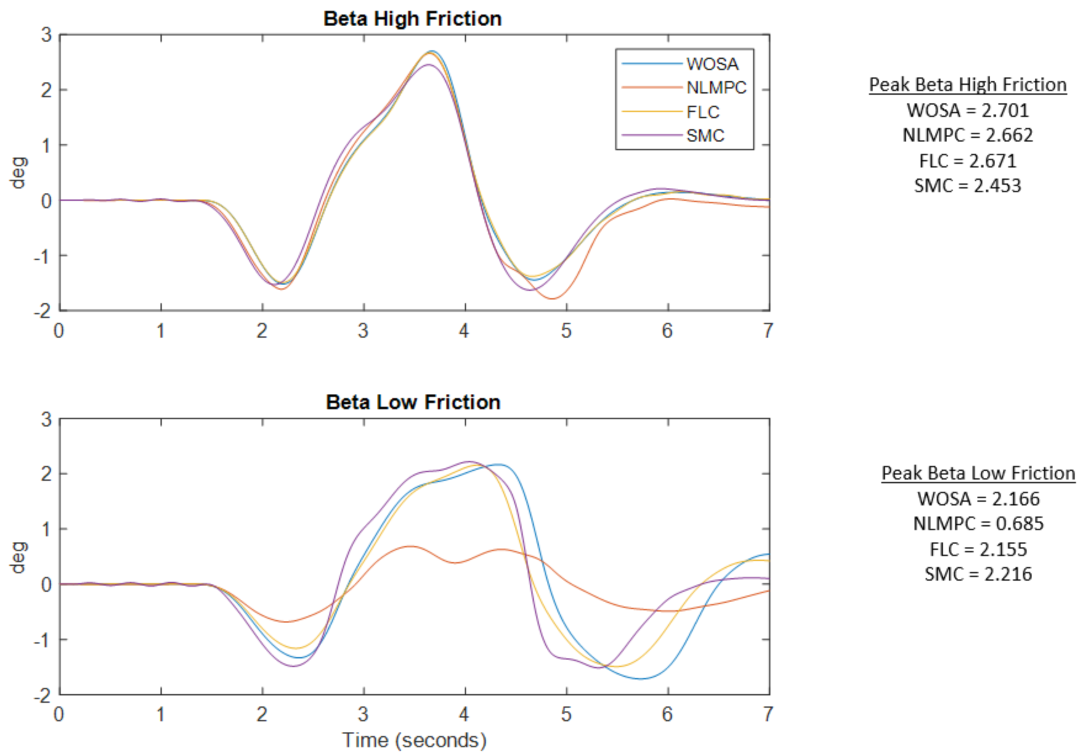

Figure 7.3 Vehicle side slip angle at C.G. comparison for high and low friction surfaces for double lane

The lateral acceleration results are presented in Figure 7.4. For the high friction case, the lateral accelerations for all four controllers is very similar. For the low friction case, the lateral acceleration for the NLMPC is significantly lower than it is for the the other controllers. This is consistent with the overall performance for the NLMPC controller for the low friction road surface.

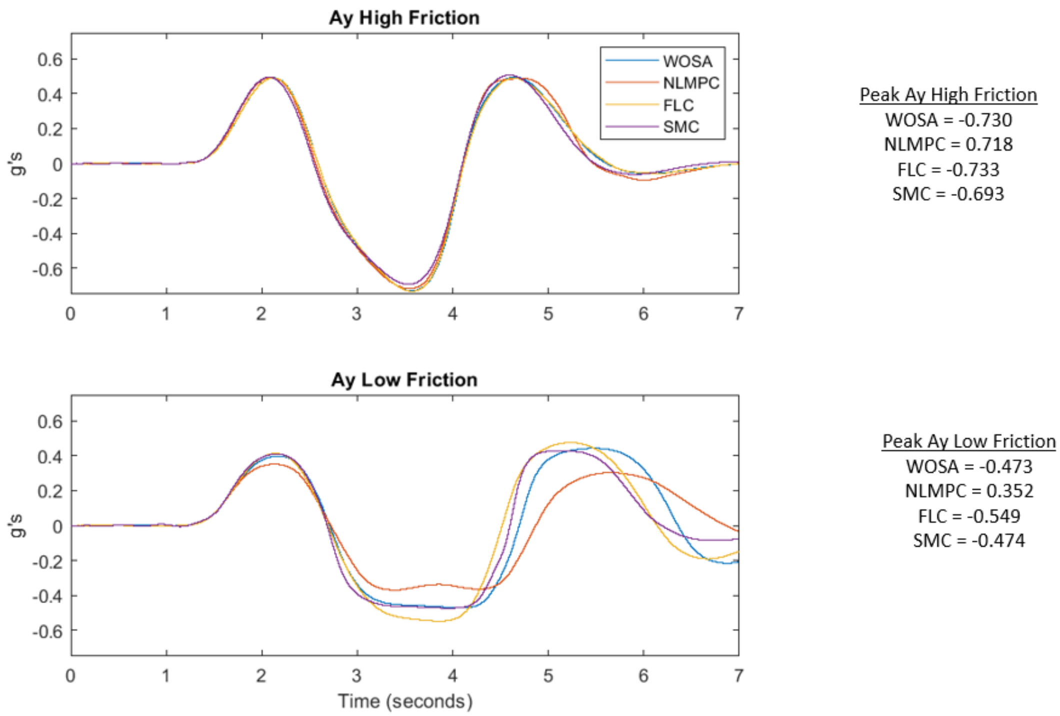

Figure 7.4 Lateral acceleration comparison for high and low friction surfaces for double lane change

The lateral vehicle speed results are presented in Figure 7.5. The results for this measurement are consistent with those for the side slip and lateral acceleration. For the high friction case, the controllers have similar results. For the low friction case, the NLMPC controller has a significantly lower peak lateral speed than the other controllers.

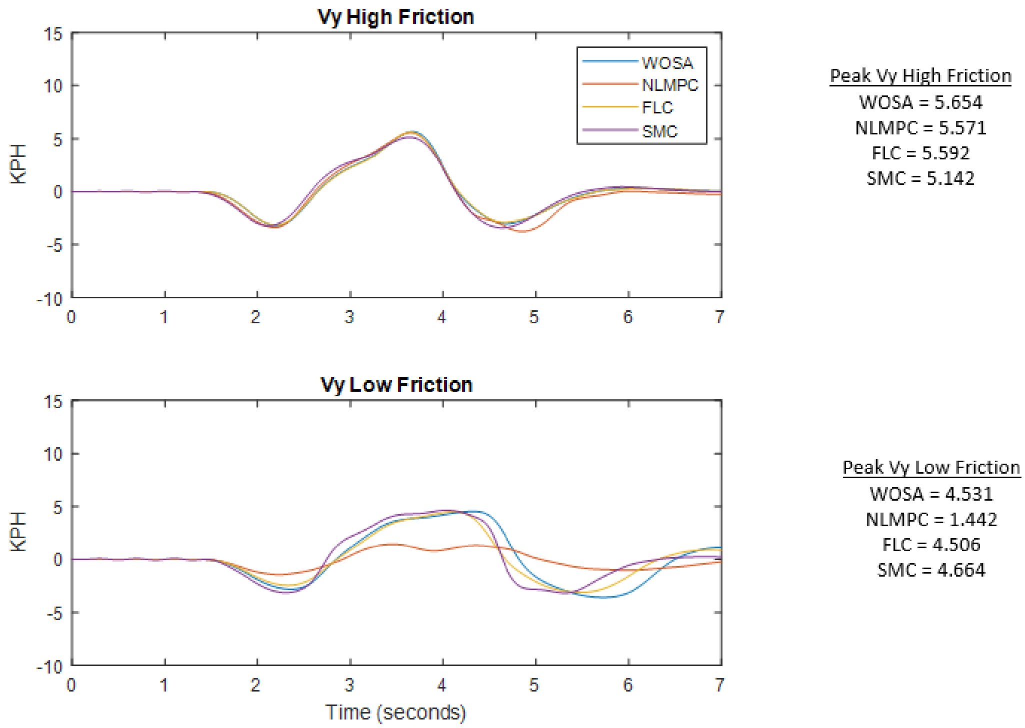

Figure 7.5 Lateral vehicle speed comparison for high and low friction surfaces for double lane change

7.3 Summary of comparison

In this chapter, a comparison of the four lateral motion controllers is presented and discussed. The measures of performance are the MSE for yaw rate target tracking, the side slip angle, the lateral acceleration and lateral vehicle speed.

A comparison of the MSE's showed that the SMC performed the best in tracking the yaw target. But the other three controllers all performed well.

For the side slip angle, lateral acceleration and lateral vehicle speed, the results were pretty consistent for both the high friction and low friction driving cases. For the high friction case, all of the controllers were very similar with slight differences in the results. For the low friction case, the NLMPC performed significantly better than the other controllers.

The conclusion of this comparison is that all four controller strategies effectively control the vehicle motion on a high friction road surface during the double lane change maneuver. For the low friction case, the NLMPC controller performed significantly better than the other three controllers, even though all of the controllers were effective.

CHAPTER EIGHT

CONCLUSION AND FUTURE WORK

8.1 Conclusion

This research explores the concept of integrating a plant model based controller with fuzzy logic rules to control an eAWD powertrain vehicle for longitudinal and lateral vehicle motion. The eAWD powertrain consists of a traction and torque vectoring motor assembly on the front and rear axle of the vehicle.

The control architecture consists of two tiers, a vehicle level tier and a motor level tier. The vehicle level tier is responsible for taking the driver demands and translating those into vehicle level control inputs. For longitudinal motion, the control input is tire traction force. For lateral motion, the control input is the vehicle yaw moment. Fuzzy logic rules are used to convert the vehicle level control inputs into target tire forces for the motor controller tier.

For longitudinal motion, fuzzy logic rules are used to allocate the tire traction force between the front and rear axles of the vehicle. The tire traction forces at each axle are the reference targets for the motor controllers. Also, fuzzy logic rules are used to adjust the motor torques to improve tracking for the vehicle level yaw rate target. For lateral motion, the fuzzy logic rules are used to convert the control yaw moment into tire force targets for the motor controllers.

For lateral motion control, several control strategies are developed. These controllers are WOSA, NLMPC, FMC and SMC. The goal is to understand how well these controller strategies work with the fuzzy rules to control the vehicle during lateral motion.

All of the controller strategies are simulated using an integrated Simulink/CarSim environment. The controller strategies are implemented in Simulink and CarSim provides a high fidelity vehicle model. Several test cases are evaluated. For longitudinal motion, launching on a high friction road surface and changing vehicle acceleration rates is the first case. The second case is launching on a low friction road surface. For lateral motion, a 120 KPH double lane change is evaluated on a high friction road surface and a low friction road surface.

The simulation results for the longitudinal motion control case demonstrated the the controller strategy is effective in meeting the driver demand for traction torque on the high friction road surface. Also, for launch on the low friction road surface, the vehicle is able to reduce the level of tire slip which maintains stability and optimizes the traction force.

For the lateral motion control case, the simulation results demonstrated that the controller is effective in assisting the driver to track the target yaw rate on the high friction road surface. But the simulation results were particularly impressive on the low friction road surface. When the controller is not active the vehicle cannot complete the double lane change maneuver. But with the controller active, the vehicle is able to successfully complete the maneuver. The simulation results for all of the controllers were (WOSA, NLMPC, FLC, SMC) were similar. However, the NLMPC controller performs better than the other controllers on the low friction road surface for the double lane change.

The WOSA control strategy is also used to implement the COO observers to estimate the traction tire force and longitudinal velocity for longitudinal motion, and lateral tire forces and lateral vehicle speed for the lateral motion case.

This research does not involve the vehicle suspension, road banking or interaction with the foundation braking system. Those aspects of the vehicle are considered out of scope of this work.

8.2 Future Work

This research explored several strategies for controlling an eAWD powertrain vehicle. Though it was demonstrated that each of these strategies (WOSA, NLMPC, FLC, SMC), coupled with fuzzy logic rules effectively control the longitudinal and lateral motion, more work can be done to improve and enhance them.

The first area of improvement is to include interaction with the friction brakes of the vehicle. In production vehicles, friction braking is used to control the stability functions. With the advent of electric motors, it's possible to coordinate the function of the friction brakes with the electric motors to achieve a higher level of stability control.

Another area of improvement is to consider the efficiency maps for control of the traction and torque vectoring motors. Taking into account how these motors produce torque would produce a more realistic control strategy.

This research included the COO strategy for estimating the longitudinal and lateral tire forces and vehicle speeds. These estimation techniques could be tested with real vehicle data to access their effectiveness.

Another area of improvement is in the calculation of the yaw rate target. The yaw rate target relied on a static estimate of the stiffness coefficient. A better and more robust target could be developed if the stiffness coefficient is estimated online. This would allow the yaw target to self adjust for different levels road surface friction.

A final area of ehancement would be to consider lateral weight shifting and road bank angle. This would make the control strategy more effective for real life vehicle operations.

LIST OF PUBLICATIONS

A. J. Ross and M. Das, “Design of an Integrated Weighted One Step Ahead and Fuzzy Yaw Controller for an Electric AWD Powertrain,” in *2023 IEEE International Conference on Electro Information Technology (eIT)*, Romeoville, IL, USA: IEEE, May 2023, pp. 314–321. doi: 10.1109/eIT57321.2023.10187285.

REFERENCES

[1] “Automakers Are Adding Electric Vehicles to Lineups,” Consumer Reports. Accessed: Sep. 29, 2023. [Online]. Available: https://www.consumerreports.org/cars/hybrids-evs/why-electric-cars-may-soon-flood-the-us-market-a9006292675/

[2] J. C. and L. Ice, “Charging into the future: the transition to electric vehicles : Beyond the Numbers: U.S. Bureau of Labor Statistics.” Accessed: Sep. 29, 2023. [Online]. Available: https://www.bls.gov/opub/btn/volume-12/charging-into-the-future-the-transition-to-electric-vehicles.htm

[3] M. Karamuk, “A survey on electric vehicle powertrain systems,” in *International Aegean Conference on Electrical Machines and Power Electronics and Electromotion, Joint Conference*, Istanbul, Turkey: IEEE, Sep. 2011, pp. 315–324. doi: 10.1109/ACEMP.2011.6490617.

[4] x-engineer.org, “EV design – vehicle control modes – x-engineer.org.” Accessed: Sep. 29, 2023. [Online]. Available: https://x-engineer.org/ev-design-vehicle-control-modes/

[5] S. J. Rind, Y. Ren, Y. Hu, J. Wang, and L. Jiang, “Configurations and control of traction motors for electric vehicles: A review,” *Chin. J. Electr. Eng.*, vol. 3, no. 3, pp. 1–17, Dec. 2017, doi: 10.23919/CJEE.2017.8250419.

[6] “Torque vectoring explained,” CarExpert. Accessed: Sep. 29, 2023. [Online]. Available: https://www.carexpert.com.au/car-news/torque-vectoring-explained

[7] “Demystifying Fuzzy Inference Systems,” Educative. Accessed: Sep. 30, 2023. [Online]. Available: https://www.educative.io/blog/fuzzy-inference-system

[8] K. Subbulakshmi, “Antilock-Braking System Using Fuzzy Logic,” 2014.

[9] P. Khatun, C. M. Bingham, N. Schofield, and P. H. Mellor, “Application of fuzzy control algorithms for electric vehicle antilock braking/traction control systems,” *IEEE Trans. Veh. Technol.*, vol. 52, no. 5, pp. 1356–1364, Sep. 2003, doi: 10.1109/TVT.2003.815922.

[10] K. Jalali, T. Uchida, J. McPhee, and S. Lambert, “Development of a Fuzzy Slip Control System for Electric Vehicles with In-wheel Motors,” *SAE Int. J. Altern. Powertrains*, vol. 1, no. 1, pp. 46–64, Apr. 2012, doi: 10.4271/2012-01-0248.

[11] J. Zhang, C. Yin, and J. Zhang, “Use of Fuzzy Controller for Hybrid Traction Control System in Hybrid Electric Vehicles,” in *2006 International Conference on Mechatronics and Automation*, Luoyang: IEEE, Jun. 2006, pp. 1351–1356. doi: 10.1109/ICMA.2006.257824.

[12] F. Tahami, S. Farhangi, and R. Kazemi, “A Fuzzy Logic Direct Yaw-Moment Control System for All-Wheel-Drive Electric Vehicles,” *Veh. Syst. Dyn.*, vol. 41, no. 3, pp. 203–221, Jan. 2004, doi: 10.1076/vesd.41.3.203.26510.

[13] K. Jalali, T. Uchida, S. Lambert, and J. McPhee, “Development of an Advanced Torque Vectoring Control System for an Electric Vehicle with In-Wheel Motors using Soft Computing Techniques,” *SAE Int. J. Altern. Powertrains*, vol. 2, no. 2, pp. 261–278, Apr. 2013, doi: 10.4271/2013-01-0698.

[14] S. Krishna, S. Narayanan, and S. Denis Ashok, “Fuzzy logic based yaw stability control for active front steering of a vehicle,” *J. Mech. Sci. Technol.*, vol. 28, no. 12, pp. 5169–5174, Dec. 2014, doi: 10.1007/s12206-014-1140-0.

[15] K. Jalali, T. Uchida, J. McPhee, and S. Lambert, “Integrated Stability Control System for Electric Vehicles with In-wheel Motors using Soft Computing Techniques,” *SAE Int. J. Passeng. Cars - Electron. Electr. Syst.*, vol. 2, no. 1, pp. 109–119, Apr. 2009, doi: 10.4271/2009-01-0435.

[16] Y. Zhang, J. Ou, E. Yang, S. Yang, and T. Meng, “Study on intelligent control of yaw stability of electric vehicle with in-wheel motors,” *J. Eng.*, vol. 2020, no. 13, pp. 584–588, Jul. 2020, doi: 10.1049/joe.2019.1162.

[17] J. V. Alcantar, “Investigation & Development of Vehicle Dynamics Control Frameworks for an Electric All-Wheel-Drive Hybrid Electric Vehicle”.

[18] S. Anwar, “Generalized predictive control of yaw dynamics of a hybrid brake-by-wire equipped vehicle,” *Mechatronics*, vol. 15, no. 9, pp. 1089–1108, Nov. 2005, doi: 10.1016/j.mechatronics.2005.06.006.

[19] J. Zhao, J. Q. Luo, J. Wu, W. W. Deng, and B. Zhu, “Optimal Distribution Strategy for Vehicle Active Yaw Moment Using Bio-Inspired Computing,” *Appl. Mech. Mater.*, vol. 461, pp. 961–966, Nov. 2013, doi: 10.4028/www.scientific.net/AMM.461.961.

[20] N. Guo, B. Lenzo, X. Zhang, Y. Zou, R. Zhai, and T. Zhang, “A Real-Time Nonlinear Model Predictive Controller for Yaw Motion Optimization of Distributed Drive Electric Vehicles,” *IEEE Trans. Veh. Technol.*, vol. 69, no. 5, pp. 4935–4946, May 2020, doi: 10.1109/TVT.2020.2980169.

[21] B. Ren, H. Chen, H. Zhao, and L. Yuan, “MPC-based yaw stability control in in-wheel-motored EV via active front steering and motor torque distribution,” *Mechatronics*, vol. 38, pp. 103–114, Sep. 2016, doi: 10.1016/j.mechatronics.2015.10.002.

[22] H. Zhou and Z. Liu, “Design of vehicle yaw stability controller based on model predictive control,” in *2009 IEEE Intelligent Vehicles Symposium*, Xi’an, China: IEEE, Jun. 2009, pp. 802–807. doi: 10.1109/IVS.2009.5164381.

[23] “What is Epicyclic Gearbox - Main Components, Working and Application?,” Mechanical Booster. Accessed: Sep. 23, 2023. [Online]. Available: https://www.mechanicalbooster.com/2017/12/epicyclic-gearbox-main-components-working-application.html

[24] Xi Chen and Liuping Wang, “Discrete-time one-step ahead prediction control (DOPC) of a Quadcopter UAV with constraints,” in *2016 Australian Control Conference (AuCC)*, Newcastle, Australia: IEEE, Nov. 2016, pp. 180–185. doi: 10.1109/AUCC.2016.7868184.

[25] L. Chu, H. Li, Y. Xu, D. Zhao, and C. Sun, “Research on Longitudinal Control Algorithm of Adaptive Cruise Control System for Pure Electric Vehicles,” *World Electr. Veh. J.*, vol. 14, no. 2, p. 32, Jan. 2023, doi: 10.3390/wevj14020032.

[26] J. V. Alcantar, F. Assadian, and M. Kuang, “Vehicle Dynamics Control of eAWD Hybrid Electric Vehicle Using Slip Ratio Optimization and Allocation,” *J. Dyn. Syst. Meas. Control*, vol. 140, no. 9, p. 091010, Sep. 2018, doi: 10.1115/1.4039486.

[27] M. S. Geamanu, H. Mounier, S.-I. Niculescu, A. Cela, G. LeSolliec, and M. S. Geamanu, “Longitudinal control for an all-electric vehicle,” in *2012 IEEE International Electric Vehicle Conference*, Greenville, SC, USA: IEEE, Mar. 2012, pp. 1–6. doi: 10.1109/IEVC.2012.6183191.

[28] L. Yuan, H. Chen, B. Ren, and H. Zhao, “Model predictive slip control for electric vehicle with four in-wheel motors,” in *2015 34th Chinese Control Conference (CCC)*, Hangzhou, China: IEEE, Jul. 2015, pp. 7895–7900. doi: 10.1109/ChiCC.2015.7260894.

[29] M. Sekour, K. Hartani, and A. Merah, “Electric Vehicle Longitudinal Stability Control Based on a New Multimachine Nonlinear Model Predictive Direct Torque Control,” *J. Adv. Transp.*, vol. 2017, pp. 1–19, 2017, doi: 10.1155/2017/4125384.

[30] T. A. Wenzel, K. J. Burnham, M. V. Blundell, and R. A. Williams, “Dual extended Kalman filter for vehicle state and parameter estimation,” *Veh. Syst. Dyn.*, vol. 44, no. 2, pp. 153–171, Feb. 2006, doi: 10.1080/00423110500385949.

[31] “Estimation, Vehicle model, Tire force, Extended Kalman filter,” *Int. J. Instrum. Sci.*, 2013.

[32] K. Kobayashi, K. C. Cheok, and K. Watanabe, “Estimation of absolute vehicle speed using fuzzy logic rule-based Kalman filter,” in *Proceedings of 1995 American Control Conference - ACC’95*, Seattle, WA, USA: American Autom Control Council, 1995, pp. 3086–3090. doi: 10.1109/ACC.1995.532084.

[33] G. Park, “A Vehicle Lateral Motion Control Based on Tire Cornering Stiffness Estimation Using In-Wheel Motors,” *Electronics*, vol. 11, no. 16, p. 2589, Aug. 2022, doi: 10.3390/electronics11162589.

[34] J. A. Herring, K. J. Burnham, and S. Oleksowicz, “Review and Simulation of Torque Vectoring Yaw Rate Control”.

[35] K. Jalali, T. Uchida, S. Lambert, and J. McPhee, “Development of an Advanced Torque Vectoring Control System for an Electric Vehicle with In-Wheel Motors using Soft Computing Techniques,” *SAE Int. J. Altern. Powertrains*, vol. 2, no. 2, pp. 261–278, Apr. 2013, doi: 10.4271/2013-01-0698.

[36] K. Sawase, Y. Ushiroda, and T. Miura, “Left-Right Torque Vectoring Technology as the Core of Super All Wheel Control (S-AWC)”.

[37] E. Siampis, M. Massaro, and E. Velenis, “Electric rear axle torque vectoring for combined yaw stability and velocity control near the limit of handling,” in *52nd IEEE Conference on Decision and Control*, Firenze: IEEE, Dec. 2013, pp. 1552–1557. doi: 10.1109/CDC.2013.6760103.

[38] A. Tahouni, M. Mirzaei, and B. Najjari, “Novel Constrained Nonlinear Control of Vehicle Dynamics Using Integrated Active Torque Vectoring and Electronic Stability Control,” *IEEE Trans. Veh. Technol.*, vol. 68, no. 10, pp. 9564–9572, Oct. 2019, doi: 10.1109/TVT.2019.2933229.

[39] "Lateral Dynamics of a Linear Single-Track Vehicle," Kelvin Tse. Accessed: Mar. 09, 2023. [Online]. Available: https://kktse.github.io/jekyll/update/2018/09/18/single-track-bicycle.html

[40] D. Vilela and R. S. Barbosa, "Analytical models correlation for vehicle dynamic handling properties," *J. Braz. Soc. Mech. Sci. Eng.*, vol. 33, no. 4, pp. 437–444, Dec. 2011, doi: 10.1590/S1678-58782011000400007.

[41] M. Metzler, D. Tavernini, A. Sorniotti, and P. Gruber, "An explicit nonlinear MPC approach to vehicle stability control".

[42] M. Choi and S. B. Choi, "Model Predictive Control for Vehicle Yaw Stability With Practical Concerns," *IEEE Trans. Veh. Technol.*, vol. 63, no. 8, pp. 3539–3548, Oct. 2014, doi: 10.1109/TVT.2014.2306733.

[43] "Wikiwand - Model predictive control," Wikiwand. Accessed: Sep. 23, 2023. [Online]. Available: https://www.wikiwand.com/en/Model_predictive_control

[44] D.-C. Liaw and W.-C. Chung, "A feedback linearization design for the control of vehicle's lateral dynamics," *Nonlinear Dyn.*, vol. 52, no. 4, pp. 313–329, Jun. 2008, doi: 10.1007/s11071-007-9280-8.

[45] Y. Sun, Q. Dai, J. Liu, X. Zhao, and H. Guo, "Intelligent vehicle path tracking based on feedback linearization and LOR under extreme conditions," in *2022 41st Chinese Control Conference (CCC)*, Hefei, China: IEEE, Jul. 2022, pp. 5383–5389. doi: 10.23919/CCC55666.2022.9901797.

[46] E. Dong, F. Wang, B. Li, and L. Zhang, "Vehicle lateral stability control based on sliding model in high-speed sharp turning condition," in *2022 International Seminar on Computer Science and Engineering Technology (SCSET)*, Indianapolis, IN, USA: IEEE, Jan. 2022, pp. 183–186. doi: 10.1109/SCSET55041.2022.00051.

[47] L. Khasawneh, "ROBUST AND ADAPTIVE LATERAL CONTROLLER FOR AUTONOMOUS VEHICLES".

[48] L. Guo, P. Ge, and D. Sun, "Fuzzy-Sliding Mode Control based Yaw Stability Control Algorithm for Four-in-wheel-motor Drive Electric Vehicle," in *2019 3rd Conference on Vehicle Control and Intelligence (CVCI)*, Hefei, China: IEEE, Sep. 2019, pp. 1–6. doi: 10.1109/CVCI47823.2019.8951601.

[49] Siqi Zhang, Shuwen Zhou, and Jun Sun, “Vehicle dynamics control based on sliding mode control technology,” in *2009 Chinese Control and Decision Conference*, Guilin, China: IEEE, Jun. 2009, pp. 2435–2439. doi: 10.1109/CCDC.2009.5192610.

[50] D. Rubin and S. Arogeti, “Vehicle yaw stability control using rear active differential via Sliding mode control methods,” in *21st Mediterranean Conference on Control and Automation*, Platanias, Chania - Crete, Greece: IEEE, Jun. 2013, pp. 317–322. doi: 10.1109/MED.2013.6608740.